

**THE STRUCTURAL AND MAGNETIC CHARACTERISATION OF
PEROVSKITE-RELATED OXYFLUORIDE MATERIALS**

by

EUAN ALEXANDER SAUCHIN SCOTT

A thesis submitted to

THE UNIVERSITY OF KENT

SCHOOL OF PHYSICAL SCIENCES

For the degree of

MASTER OF SCIENCES BY RESEARCH

Supervisor: Dr Emma E. McCabe

The School of Physical Sciences

G.20, Ingram Building

University of Kent

Canterbury

CT27NH

To My Father

Inspiring, honourable, and modest

CONTENTS

ACKNOWLEDGEMENTS.....	iii
ABSTRACT	iv
Introduction.....	- 1 -
1.1 Perovskites.....	- 1 -
1.1.1 Tolerance Factor	- 1 -
1.1.2 Perovskite Distortions	- 2 -
1.2 Layered Perovskite-Related Materials.....	- 3 -
1.2.1 Ruddlesden-Popper Phases.....	- 3 -
1.2.2 Dion-Jacobson Phases	- 4 -
1.2.3 Aurivillius Materials.....	- 4 -
1.3 Ferro- & Piezo-electrics.....	- 5 -
1.3.1 Piezoelectric effect	- 6 -
1.3.2 Ferroelectricity.....	- 6 -
1.4 Magnetism.....	- 7 -
1.5 Aims.....	- 7 -
Experimental and Analysis Methods	- 9 -
2.1 Experimental Methods.....	- 9 -
2.1.1 Solid State Synthesis.....	- 9 -
2.1.2 Hydrothermal Synthesis.....	- 9 -
2.2 Analytical Methods.....	- 9 -
2.2.1 X-Ray Powder Diffraction	- 9 -
2.2.2 Neutron Powder Diffraction.....	- 10 -
2.2.3 Rietveld Refinement Analysis.....	- 11 -
2.2.4 Pawley Method	- 12 -
2.2.5 ISODISTORT.....	- 12 -
2.2.6 X-Ray Absorption Near-Edge Structure (XANES) Analysis	- 12 -
2.2.7 Second Harmonic Generation.....	- 12 -
Characterisation of $\text{Bi}_2\text{CoO}_2\text{F}_4$	- 13 -
3.1 Background.....	- 13 -
3.2 Aims.....	- 14 -
3.3 Experimental Method.....	- 14 -
3.4 Structural Refinement Using X-ray Powder Diffraction Data.....	- 14 -
3.4.1 Variable temperature XRPD.....	- 16 -
3.5 Investigation of Co Oxidation State Through XANES/EXAFS Data.....	- 17 -
3.6 Structural Refinement Using 50 K Neutron Powder Diffraction Data.....	- 18 -
3.6.1 Determination of the Lattice Parameters.....	- 18 -

3.6.2	Determination of Distortions in Octahedra and Fluorite-Like Layers.....	- 18 -
3.6.3	Mode Inclusion Simulated Annealing.....	- 20 -
3.6.4	Pawley Refinements Using Low Symmetry Models.....	- 21 -
3.6.5	Rietveld Refinement of $\text{Bi}_2\text{CoO}_2\text{F}_4$	- 22 -
3.7	Investigation of Anion Distribution through Bond Valence Sum Calculations	- 33 -
3.8	Magnetic Structural Characterisation Using 5 K Neutron Powder Diffraction Data	- 34 -
3.8.1	Simulated Annealing of Magnetic Modes.....	- 35 -
3.8.2	Refinement of Magnetic Structure	- 38 -
3.9	Discussion.....	- 42 -
Anion Order to Break Inversion Symmetry.....		- 43 -
4.1	Introduction.....	- 43 -
4.1.1	How to Get Anion-Order.....	- 43 -
4.1.2	Summary of Proposals from Theory	- 46 -
4.1.3	Aurivillius Oxyfluorides.....	- 46 -
4.2	Symmetry Analysis.....	- 48 -
4.2.1	Apical, Equatorial &/or Fluorite Layer occupancy.....	- 48 -
4.2.2	Discussion.....	- 51 -
4.2.3	Conclusion.....	- 51 -
Conclusions		- 52 -
5.1	Characterisation of $\text{Bi}_2\text{CoO}_2\text{F}_4$	- 52 -
5.2	Anion Order to Break Inversion Symmetry	- 52 -
Appendix A - Characterisation of $\text{Bi}_2\text{CoO}_2\text{F}_4$		- 58 -
1.6	Pawley Refinements of XRPD Data	- 58 -
1.7	Enhanced Images of Tetragonal and Orthorhombic 50 K NPD Refinement Reflections	- 59 -
1.8	Pawley Refinements of 50 K NPD Data using Various Unit Cell Parameters.....	- 61 -
1.9	Pawley Refinements of 50 K NPD Data using Space Groups deduced from IOSDISTORT.....	- 65 -
1.10	Rietveld Refinement of 50 K NPD Data using Various Models	- 66 -
2.1.1	<i>Fmm2</i> Model.....	- 66 -
1.10.3	<i>Abm2</i> Model.....	- 67 -
1.10.4	<i>Cmca</i> (X_2^+) Model	- 68 -
Appendix B - Anion Order to Break Inversion Symmetry		- 70 -
2.1	Space Groups Derived from Apical and Equatorial Ordering Modes	- 70 -
2.2	Space Groups Derived from Anion Ordering and Octahedral Rotational Modes	- 71 -

ACKNOWLEDGEMENTS

For providing expertise, assistance or guidance for any work or research related to this degree:

I would like to thank Eleni Mitoudi Vagourdi and Professor Mats Johnsson from the University of Stockholm for experimental assistance by synthesising and sending samples of $\text{Bi}_2\text{CoO}_2\text{F}_4$ ready for neutron powder diffraction work and providing interesting discussion about the research undertaken.

Thank you to Dr Ivan de Silva and Dr Alex Gibbs at the ISIS neutron and muon source for providing expertise and guidance whilst collecting neutron powder diffraction data.

I am grateful to Dr Vanessa Cascos for collecting variable temperature X-ray powder diffraction and neutron powder diffraction data from ISIS with Emma. I am thankful to Filbin John for collecting X-ray data as well as XANES data at the Diamond Light Source.

I would like to thank Professor Alan Chadwick and Dr David Pickup for offering help and expertise with collecting XANES data, and Dave for patiently showing me how to analyse using Athena and always being on hand when things went wrong.

A big thank you to my second supervisor Dr Paul Saines, for the help that he gave me throughout the degree, and to the whole MEE group for engaging in interesting conversations, helping me with issues and offering guidance where needed. With special mention to Mario, Jordan and James who always helped whenever I needed it, either in the lab or with my writing up, and always having great discussions, not too commonly, over a pint.

Most importantly, I would like to thank my supervisor Dr Emma E. McCabe for taking me on as her Master's student and going above and beyond with all her help, guidance, and support throughout the whole degree. I am truly grateful for giving me the opportunity to prove myself, always giving me gentle encouragement and a fondness for solid state chemistry.

ABSTRACT

This thesis explores two $n=1$ Aurivillius oxyfluoride phases and their structural characterisation and how this relates to their physical properties.

$\text{Bi}_2\text{CoO}_2\text{F}_4$ was successfully analysed using XRPD, NPD, XANES and SHG techniques. Structural characterisation of NPD data collected at 50 K and at 5 K indicated rotations of CoF_6 octahedra about both in-plane and out-of-plane axes, whilst SHG activity supports the assignment of a non-centrosymmetric symmetry. Rietveld refinements suggest a ground state $Pca2_1$ symmetry. Low temperature NPD data allowed exploration of the magnetic structure. Analysis indicated the magnetic symmetry was close to a collinear antiferromagnetic structure with in-plane moments; however, two very similar magnetic structures were obtained, one of which has a ferromagnetic component allowed by symmetry, which may explain unusual field dependence found in magnetic susceptibility measurements.

Theory work has highlighted the possibility of anion ordering in heteroanionic materials breaking inversion symmetry and so we carry out a symmetry analysis of possible anion-ordered arrangements for $\text{Bi}_2\text{TiO}_4\text{F}_2$ assuming *mer* or *fac* $[\text{TiO}_3\text{F}_3]$ units. Although these units are polar, there are 12 ways of arranging these polar units based on an ideal parent model of $I4/mmm$ symmetry, only 4 of these models are non-centrosymmetric and would allow macroscopic polarisation. Interestingly, further analysis has shown that allowing non-polar octahedral rotations in non-polar anion-ordered models can break inversion symmetry, and this represents a new avenue for designing hybrid-improper materials.

CHAPTER ONE

Introduction

1.1 Perovskites

Perovskites are a very widely studied class of materials of general formula ABX_3 (A is a large cation, usually an alkali, alkaline earth, or lanthanide metal ion; B -site is a medium sized cation, commonly a transition metal, and the X -sites are occupied by anions). The structure of perovskite oxides, of the general structure ABO_3 , is composed of corner shared BO_6 octahedra with the A cation in a 12-coordination body centre site, AO_{12} , as seen in *Figure 1.1.1*.¹

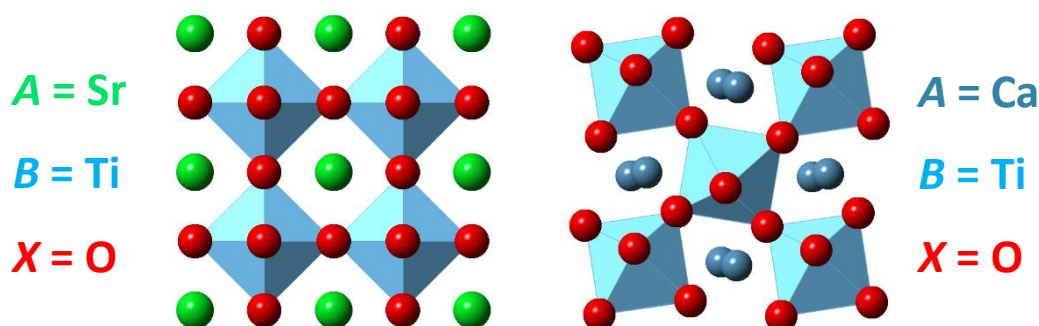


Figure 1.1.1 - The perovskites structures of SrTiO₃ (left) and CaTiO₃ (right) displaying how different A-site cation sizes can give to the ideal and distorted symmetries, respectively. Showing strontium (green)/calcium (blue) and oxygen (red).

Since the 1940s, with the discovery of dielectric and ferroelectric properties in BaTiO₃, these materials have been extensively investigated. The fascination with these materials stems from the close correlation between the chemical and physical properties, allowing characteristics to be tweaked and tuned by composition. Owing to this flexibility, a vast array of perovskites can be synthesised, from all-inorganic oxides, like SrTiO₃, to the inorganic-organic hybrid perovskite CH₃NH₃PbI₃ (with CH₃NH₃⁺ in the A -site).^{1,2} Many of these perovskites undergo structural distortions such as octahedral tilts, rotations and displacements due to the sizes and electron configurations of the ions, which in turn, allow these materials to exhibit unique and fascinating properties, suitable for a wide range of applications.³

1.1.1 Tolerance Factor

Goldschmidt, in 1926, suggested that a tolerance factor could be employed as a basis to determine the likelihood of a perovskite structure forming. The ideal perovskite has a cubic structure with A and B ions at the corners and centre of the unit cell and anions in the centre of each face (*Figure 1.1.1*).

The tolerance factor, t , depends on the ionic radii of the ions r_A , r_B and r_X :

$$t = \frac{(r_A - r_X)}{\sqrt{2}(r_B - r_X)}$$

The ideal perovskite structure has t close to 1.0. For $t > 1$, the A cations are relatively too large for the B cations and the cubic structure is less stable; hexagonal perovskites (e.g. BaMnO₃)⁴ may form. For $t < 1$, the B cations are too large for the ideal cubic structure and distortions, such as octahedral rotations, may occur (e.g. CaTiO₃,⁵ *Figure 1.1.1 (right)*).

The tolerance factor alone is not sufficient to predict stability of a perovskite structure. Chongea Li and L. M. Feng showed limitations in previous attempts at a 'structural map' for perovskite formability and came up with a simple determination of adding an octahedral factor, μ .^{6,7}

$$\mu = \frac{r_B}{r_O} = 0.425$$

with r_B and r_O representing ionic radii of the B cation and oxygen in the system, respectively. Initially this factor was used specifically for ABO_3 perovskite oxides, where the lowest limit of the ‘octahedral factor’ for a perovskite structure to form was 0.425.⁶ However, later research showed that the equation can be applied to halide perovskites, where the limits for a perovskite structure forming is between 0.442 and 0.895.⁸

Combining the octahedral factor and tolerance factor Li and Feng were able to form an equation which calculates the lower limits of the ‘structural map’.

$$\frac{-4.317(r_A + r_O)}{\sqrt{2}(r_B + r_O)} + 3.912 = \frac{r_B}{r_O}$$

where r_A , r_B and r_O represents atomic radii of A , B and O ions, respectively.

These three equations can be used to create a ‘structural map’ which can reliably (99.5% accuracy for perovskite oxides)⁶ predict whether a perovskite structure is likely to form.

1.1.2 Perovskite Distortions

1.1.2.1 First Order Jahn-Teller Distortions

The BX_6 octahedra, dependent on different conditions, can undergo distortions: elongation/compression of the octahedra and/or rotation/tilting of the octahedra and/or cation displacements.⁹

First order Jahn-Teller distortions occur where the electron configurations of the B site cation allowing an unequal occupation of degenerate orbitals is unstable with respect to distortions of the octahedra, in the form of elongations/compressions. Axial bonds lengths will either be longer or shorter than the equatorial bond lengths in these types of octahedral units, as seen in some cuprate oxide octahedra $[CuO_6]$.¹⁰

1.1.2.2 Cation Displacements

This is where cations are displaced away from the center of their coordination polyhedra. The displacement can be considered in terms of electrostatics (e.g., a small, highly charged cation displacing towards an anion to optimize its coordination environment). It is often considered in terms of electronic factors such as the second order Jahn Teller effect (SOJT). This involves the lowering of symmetry, which promotes the mixing of the electronic ground state (HOMOs) and the excited states (LUMOs) to lower the ground state energy. This change in geometry of the structure is accompanied by a permanent electric dipole within the structural unit.¹¹

1.1.2.3 Tilts & Rotations

‘Tilting’ of octahedra comes about due to the A -site cation being ‘too small’ for the ideal cuboctahedral site: tilting of BX_6 octahedra reduces the A -site cavity size, stabilising perovskite compositions with tolerance factor $t < 1$. The corner-shared connectivity of the BX_6 octahedra means that tilting of one octahedra will determine the tilting in the plane perpendicular to the tilt axis. The adjacent plane will imitate the first plane either in-phase or out of phase.

Easy exchange of anions in the perovskite ABX_3 structure have allowed further tuning of properties via the halide perovskites. Studies have found that octahedral tilting can be influenced by the ionicity/covalency of the A - X and B - X bonds.¹² When A - X bonds are more ionic and B - X bonds are more covalent tilted structures are preferred. These influences have led to advances in materials with non-oxide anions and heteroanionic materials, such as the oxyfluorides.¹³

1.2 Layered Perovskite-Related Materials

Intensive research has been directed at two-dimensional, or layered, perovskite-related materials for decades, owing to their diverse array of physical, electronic, and chemical characteristics. These materials display the potential for photocatalytic, magnetic, and dielectric properties, with extensive interest in ferroic properties. Families of layered perovskite-related materials include the Dion-Jacobson (DJ) Ruddlesden-Popper (RP) and Aurivillius families, which differ in the stacking of perovskite blocks, and the inter-layers between them, as outlined below.⁹

1.2.1 Ruddlesden-Popper Phases

Ruddlesden-Popper (RP) materials are layered perovskite-related phases with structures composed of two-dimensional perovskite-like blocks separated by rock-salt layers. RP phases have the general formula $A_{n+1}B_nX_{3n+1}$ (where A represents larger 9- and 12-coordinated cations, B represents medium sized 6-coordinated cations, X is an anion, and the n is the number of layers of octahedra in the perovskite-like stack). With $n = 2$ RP phases, the general formula is $A_3B_2O_7$. The $n = 2$ phases have two A -sites: a 12-coordinate site in the middle of the perovskite block, and a 9-coordinate site in the rocksalt layer, see *Figure 1.2.1*.

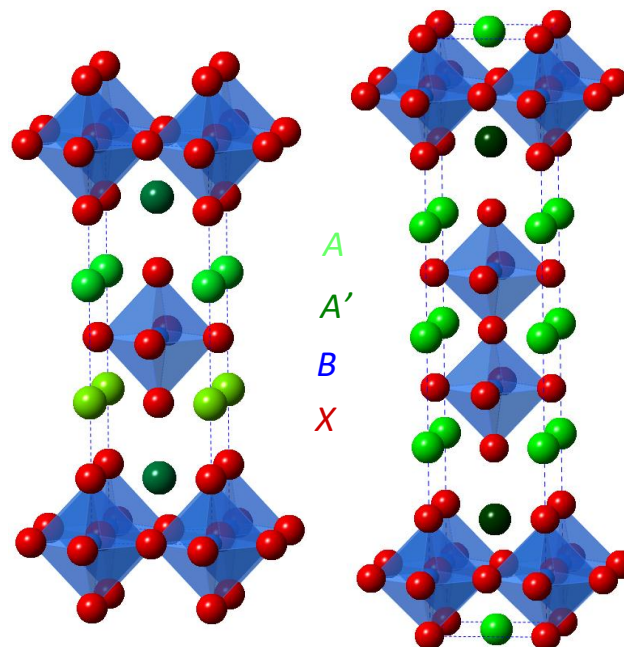


Figure 1.2.1 – Illustrations of the $I4/mmm$ high symmetry $n = 1$ (left) and $n = 2$ (right) Ruddlesden-Popper phases, representing the $A_{n+1}B_nX_{3n+1}$ structure, where 9- and 12-coordinate A -site cations are shown in dark green and light green, respectively, oxide anions are shown in red and BX_6 octahedra are shown in blue.

1.2.1.1 Topotactic Reactions on RP Phases

Development of transition-metal oxides has stimulated research into mixed-anion systems, as two different anions in a sublattice gives the opportunity to control and enhance chemical or physical properties found in pure oxides. Synthesising oxyfluorides through high temperature synthesis is difficult because the oxyfluoride phases are often metastable and high temperature reactions are more likely to give thermodynamically stable fluoride or oxide phases. As a result, soft chemistry (*chimie douce*) approaches can be employed, such as fluorination.^{14,15} These techniques are typically low temperature reactions on parent oxides. In fluorination the reaction can be substitutional, as seen in the fluorination of Ba_2ZrO_4 ,¹⁶ or the reaction can be oxidative, such as the low temperature fluorination of $La_2SrCr_2O_7$.¹⁷ The low fluorination temperature means that there is relatively little disruption to the parent structure with additional anions often inserted into interstitial sites (often favouring anion-ordered structures). However, introducing anions into interstitial sites can change the spacing between perovskite-like layers and the size

and electron configuration of the cations, changing the structure as well as magnetic and electronic behaviour.^{18,19}

1.2.2 Dion-Jacobson Phases

With their name derived from its discoverer, Dion, in 1981 and the extended research done by Jacobson in 1986, Dion-Jacobson (DJ) materials form a homologous series with the general formula $A'A_{n-1}B_nO_{3n+1}$ for $n > 1$. The structure consists of n layers of corner-linked BO_6 octahedra and 12-coordinate A cations, separated by layers of univalent alkali earth cations, A' . The ideal structure is tetragonal, with $P4/mmm$ symmetry.^{20,21} The perovskite blocks are stacked in either eclipsed or staggered arrangements depending on the size of the interlayer A' cations (e.g. eclipsed for larger Rb^+ , Cs^+ ions; staggered for smaller K^+ ions)²² as illustrated in *Figure 1.2.2*.

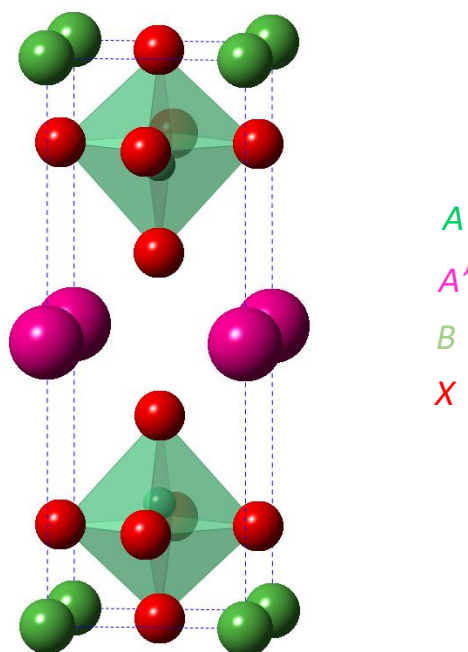


Figure 1.2.2 - Illustrations of the $I4/mmm$ high symmetry $n = 2$ Dion-Jacobson phases, illustrating the $A'A_{n-1}B_nO_{3n+1}$ structure, with A - and A' -site cations in green and pink, respectively, anions-sites in red and BX_6 perovskite octahedra in green.

The size of the A -site cation can tune the degree of octahedral tilting and resulting symmetry.²³ DJ phases have gained attention due to their potential to show polar behaviour by the hybrid improper mechanism (see *Section 1.3.2.1*).³

1.2.3 Aurivillius Materials

Aurivillius structures, named after their discoverer Bengt Aurivillius, have the general formula $M_2O_2(A_{n-1}B_nO_{3n+1})$, where M is a non-spherical ion (almost always by Bi^{3+}), A is generally an s or f block cation and B site is usually a d^0 transition metal. These materials can be thought of as perovskite blocks n layers thick stacked along $[001]$, separated by fluorite-like bismuth oxide layers, $[Bi_2O_2]^{2+}$, see *Figure 1.2.3*.²⁴⁻²⁶

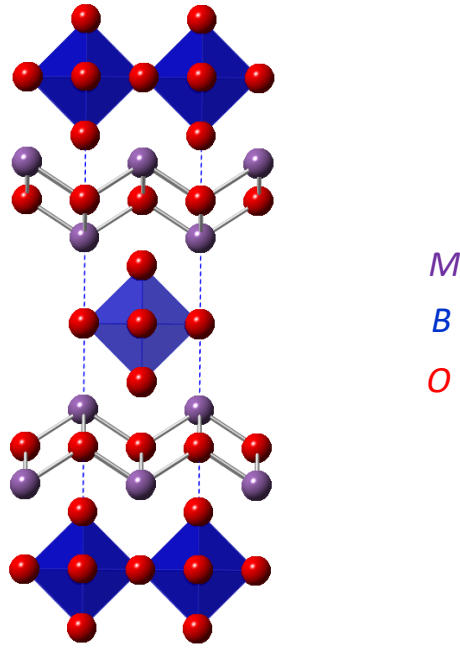


Figure 1.2.3 - Illustrations of the $I4/mmm$ high symmetry $n = 1$ Aurivillius phases, representing the $M_2O_2(A_{n-1}B_nO_{3n+1})$ structure, where oxide anions are shown in red, BO_6 octahedra are shown in blue and the bismuth cations are shown in purple.

Some interesting properties of Aurivillius phases include ionic conductivity²⁷ and photocatalytic properties.²⁸ The B -site is usually occupied by d^0 transition metals and it has proven difficult to introduce high concentrations of magnetic transition metals into the B sites in the perovskite-like layers.²⁹

Most Aurivillius materials tend to share similar structural and functional characteristics. The $I4/mmm$ space group describes the ideal high-symmetry reference structure, whilst at low temperatures many Aurivillius materials adopt orthorhombic or monoclinic structures, many of which are polar.⁹ The low temperature phases of most Aurivillius phases are ferroelectric with high Curie temperatures (e.g. $T_c > 600$ K). Studies on these materials show some to possess fatigue-free behaviour³⁰ and low current leakage, making them attractive for commercial applications.

The two results chapters of this thesis focus on $n = 1$ Aurivillius materials. Several $n = 1$ Aurivillius phases have been reported, including Bi_2WO_6 , Bi_2MoO_6 , Bi_2NbO_5F , $Bi_2TiO_4F_2$. These phases have lower symmetries than described by the ideal $I4/mmm$ space group, such as the $Pca2_1$ symmetries found in Bi_2WO_6 and Bi_2MoO_6 ,³¹ due to rotations/tilts of the octahedra about the in-plane and out-of-plane axes, and polar or antipolar cation displacements, discussed in more detail in *Chapter 3* (see *Figure 3.6.2*).

The $Bi_2TiO_4F_2$ and Bi_2NbO_5F phases seem to show tilting of BX_6 octahedra. $Bi_2TiO_4F_2$, however, only shows rotations in the short-range (hence disordered $I4/mmm$ model reported)³², whilst a non-polar $Pbca$ structure is reported for Bi_2NbO_5F .³³ In contrast, the oxide Bi_2WO_6 ^{34,35} is reported to have rotations of octahedra about both the short in-plane and long out-of-plane axes as well as in-plane polar displacements at low temperatures, however, phase transitions occur at higher temperatures, losing the out-of-plane rotation at 660 °C whilst at 960 °C the unit cell is restructured, consisting of units of $[Bi_2O_2]$, $[WO_4]$ and $[WO_2]$.³⁵

1.3 Ferro- & Piezo-electrics

Most solids, despite some having local dipole moments, form structures with no net dipole moment. However, some classes of solids are known to adopt non-centrosymmetric structures that allows a macroscopic polarisation. These materials have been extensively researched for their commercial importance. The rest of this section will cover these types of materials.

1.3.1 Piezoelectric effect

Piezoelectrics are a class of materials for which the application of a mechanical stress generates an electric voltage (and the inverse effect). This phenomenon occurs due to the application of mechanical stress or electric field causing the movement of atoms within the unit cell creating a dipole moment. Piezoelectricity was first discovered in barium titanate (BaTiO_3)³⁶ ceramics leading to the fast development of other piezoelectric materials, such as, PZT or lead zirconate titanate ($\text{Pb}[\text{Zr}_{(x)}\text{Ti}_{(1-x)}]\text{O}_3$) one of the most widely used commercial piezoelectric perovskites.³⁷ Piezoelectric crystals are commercially important for applications in piezo-sensors and resonators.

1.3.2 Ferroelectricity

Ferroelectric materials adopt non-centrosymmetric structures with a net dipole, the direction of which can be changed by application of an electric field (see *Figure 1.3.1*). The coupling between polarisation and the applied field can only occur for materials with polar structures, where cation displacements drive the switch between metastable states, such as BaTiO_3 .³⁶

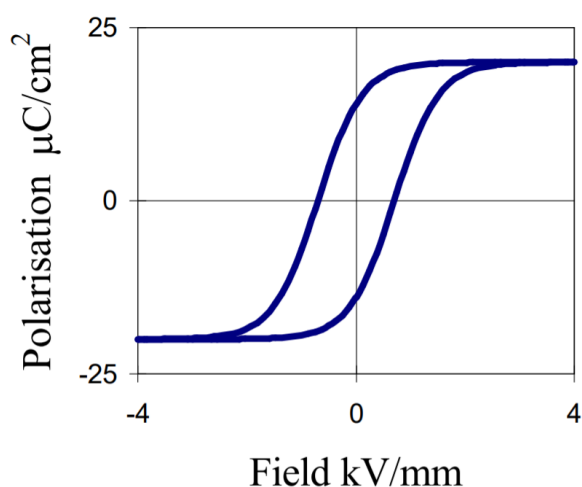


Figure 1.3.1 – Illustration of a ferroelectric polarisation on application and dependence of an electric field, reproduced from reference.³⁸

The ease of forcing the switch between polarisations is described as hard or soft, where hard ferroelectrics require larger applied fields to drive the polarisation, and vice versa for soft ferroelectrics. Ferroelectrics have a critical temperature, named the Curie temperature (T_c) which signifies the point above which a material is no longer ferroelectric, rather, is paraelectric. Above T_c the material adopts a high symmetry non-polar centrosymmetric structure whilst below T_c it adopts the lower symmetry polar non-centrosymmetric structure. The best way to find the transition temperature T_c , is by plotting relative permittivity or dielectric constant, ϵ_r , against temperature.

The type of ferroelectricity described above, in which polar displacements drive the phase transition, is often referred to as ‘proper’ ferroelectricity. Recent theory work has shown that non-polar distortions can sometimes couple to break inversion symmetry and stabilise polar, non-centrosymmetric structures.³⁹ This “hybrid improper” mechanism is outlined in the next section.

1.3.2.1 Hybrid Improper Mechanism

The hybrid-improper mechanism for ferroelectricity in RP phases was first demonstrated by Benedek and Fennie for the $n = 2$ Ruddlesden-Popper (RP) materials, $\text{Ca}_3\text{Ti}_2\text{O}_7$ and $\text{Ca}_3\text{Mn}_2\text{O}_7$. Octahedral rotations, corresponding to $a^0a^0c^+$ (X_2^+) and $a^-a^-c^0$ (X_3^-), couple trilinearly with the zone-centre polar Γ_5^- symmetry mode to break the inversion symmetry and allow in-plane polarisation, giving structures of $A2_1am$ symmetry, instead of the ideal $I4/mmm$ symmetry structure. This demonstrated how ferroelectric phase transitions can be driven by two non-polar lattice distortions. In contrast to the proper ferroelectrics, the

non-polar tilts stabilise polar displacements.^{40–42} This mechanism, termed hybrid improper mechanism,³⁹ was also found in Dion-Jacobson materials where *A*-site under-bonding in the idealised $P4/mmm$ structure drives the distortion to polar structures via trilinear coupling; here octahedral tilts can optimize the *A*-site bonding.^{43,44}

Both proper and improper mechanisms rely on the sizes and electron configurations of ions, meaning that the properties of materials can be tuned, which has led to a lot of curiosity by material scientists in this area.

1.3.2.2 Relaxor Ferroelectrics

Some ferroelectric materials exhibit a broad maximum in ϵ_r vs T which is changed by the frequency of applied electric field. This diffuse phase transition often results from compositional inhomogeneities in the materials which can give rise to polar nano-regions.⁴⁵ Disorder on the anion sublattice has also been suggested as a route to relaxor-like behaviour.⁴⁶

1.4 Magnetism

This section discusses different types of magnetism. Diamagnetism is a weak effect found in all materials with paired electrons which gives rise to a magnetic field that opposes an applied magnetic field. This causes (weak) repulsion of diamagnets by an applied magnetic field.

Unpaired electrons are associated with paramagnetism which is a stronger effect and causes paramagnetic materials to be attracted by an applied magnetic field. Paramagnetic materials have magnetic moments randomly oriented, but an applied magnetic field will induce a small paramagnetic moment causing weak attraction. Transition metal complexes are often paramagnetic. The origin of an electron's magnetic moment is its spin and orbital angular momenta.

Ferromagnetism is a type of permanent magnetisation, meaning that even after an applied magnetic field is removed the material will retain some magnetization, analogous to the hysteresis observed in a ferroelectric (*Figure 1.3.1*). The magnetic moments in a ferromagnet point in the same direction, which can be switched by an external magnetic field. This type of magnetisation occurs in only a few metals, including iron, cobalt, nickel, and a few lanthanoids. This is because the transition metal here has narrow 3d bands, which have less overlap than 4s, 4p, 4d or 5d orbitals, and can have up to five 3d orbitals. This causes a high density of states in the fermi band making the material energetically favourable to support high numbers of parallel unpaired electrons without a magnetic field. Lanthanoid ferromagnets work in a similar way, by interactions of delocalised d electrons and localised f electrons which align parallel to reduce the electron repulsion. Ferromagnetic materials only have this permanent magnetic moment below the critical temperature or Curie temperature, T_c , whereas above T_c , they will be paramagnetic.

Antiferromagnetic materials behave similarly but with an antiparallel arrangement of spins giving a net zero magnetisation. This spontaneous antiferromagnetic order is disrupted above the Néel temperature T_N , and the material becomes paramagnetic.

1.5 Aims

Chapters 3 & 4 of display the results, discussion and concluding remarks of the research presented in this thesis. In chapter 3, we characterise the atomic unit cell of $\text{Bi}_2\text{CoO}_2\text{F}_4$ using neutron powder diffraction (NPD), investigating potential long-range octahedral distortions, and determination of low temperature antiferromagnetic structure. In chapter 4, we perform symmetry analysis on the $\text{Bi}_2\text{TiO}_4\text{F}_2$ to demonstrate the possibility of breaking inversion in heteroanionic systems by ordering O^{2-} and F^- over anion sites and an also through coupling of octahedral rotations.

Chapter 3 in this thesis had the following aims for research conducted on $\text{Bi}_2\text{CoO}_2\text{F}_4$:

- Using 50 K NPD data investigate long-range octahedral distortions to determine the low symmetry structure.
- Perform bond valance sum analysis to determine likely anion arrangements.

- Using 5 K NPD data determine the low temperature magnetic structure.
- Determine the cobalt oxidation state using XANES data and confirm stoichiometry of material.
- Second harmonic generation tests will be done to distinguish whether the material is centrosymmetric.

Chapter 4 in this thesis had the following aims for research conducted on $\text{Bi}_2\text{TiO}_4\text{F}_2$:

- Perform symmetry analysis to determine likelihood of octahedral anion occupational modes coupling to break inversion symmetry.
- Perform further analysis to determine the possibility of non-polar anion occupation coupling with non-polar rotational modes to break inversion symmetry.

CHAPTER TWO

Experimental and Analysis Methods

2.1 Experimental Methods

2.1.1 Solid State Synthesis

Commonly referred to as the ceramic method, the solid-state synthesis method, involving direct reaction of reagents in the solid state (often at high temperatures) is widely used to make polycrystalline samples. The usual premise of a solid-state reaction requires reagents, of desired stoichiometry, to be ground together, whether by pestle and mortar or ball milling, for maximum surface area of reagents and to create a homogeneous mixture. The sample may be pelletised before heating to high reaction temperatures (below the decomposition or melting temperatures of the reagents). Long reaction times are often needed, and the sample may be cooled and reground, and the high temperature reaction continued until no further change is observed in the reaction products. The rate of the reaction depends on the extent of mixing of reagents, and the diffusion of reagents to reaction points.

This type of synthesis is not without its limitations. For atoms to diffuse, high reaction temperatures and long reaction times are required to overcome the activation energies for diffusion. This makes it difficult to prepare kinetic phases and to avoid the formation of undesired thermodynamic phases.

At the start of this project, the solid-state method was used to synthesis materials in the potential solid solution $\text{Sr}_{3-x}\text{Ca}_x\text{Zr}_2\text{O}_7$, but this synthetic aspect of the project was stopped due to interruption caused by the covid-19 pandemic.

2.1.2 Hydrothermal Synthesis

This synthetic route involves heating reagents in an autoclave with water. Water heated in an autoclave will remain liquid above 100°C (called superheated water). This form of synthesis allows lower temperatures and high-pressure reactions, which can be used to prepare metastable phases. Autoclaves are made from stainless steel and can be lined with non-reactive materials, usually quartz or Teflon. Aside from the risk of the high-pressure metal apparatus, this method allows relatively low reaction temperatures compared to traditional solid-state method.

Hydrothermal synthesis was used by our collaborators E. M. Vagourdi and Dr M. Johnson, at the Department of Materials and Environmental Chemistry, Stockholm University, for the preparation of the $\text{Bi}_2\text{CoO}_2\text{F}_4$ Aurivillius phase characterised in this project.⁴⁷

2.2 Analytical Methods

2.2.1 X-Ray Powder Diffraction

X-ray powder diffraction (XRPD) can be used to identify and characterise crystalline materials. X-rays are waves of electromagnetic radiation, with wavelengths between 0.1 and 100 Å. These waves can be scattered by the periodically arranged electron clouds around atoms in crystals and are most sensitive to heavier atoms with more electrons.

As X-rays are diffracted by crystalline materials, their diffraction patterns can be analysed to investigate the sample's component phases, their unit cell sizes and symmetries, their crystal structures as well as microstructure (particle size, stress and strain).

X-ray diffraction can be carried out on single crystals or on powder samples. In single-crystal X-ray diffraction (SCXRD), accurate crystal structures can usually be determined. However, it can be challenging to prepare high quality single crystals of complex materials and results from SCXRD are not always representative of the bulk sample.

In X-ray powder diffraction (XRPD), X-rays are scattered by a polycrystalline sample (made up of a huge number of randomly oriented crystallites) and the diffraction patterns can be analysed to determine the phases present in a sample, its purity and unit cell parameters. Due to the speed at which diffraction patterns can be collected, measurements can be taken as a function of temperature, pressure and/or other environments.

The Bragg reflection angles and reflection intensities are both measured in a diffraction experiment and can give information on the average crystal structure. The scattering angle, θ , is defined by the Bragg equation:

$$n\lambda = 2d \sin\theta$$

where n is the diffraction order; λ is the wavelength of the incident X-ray, d is the distance between planes, and θ the Bragg angle.

In a diffraction experiment, constructive interference (and a peak in the diffraction pattern) occurs when X-rays are scattered by angles of θ , such that $\sin\theta = \frac{n\lambda}{2d}$. In-phase X-rays that interfere constructively give peaks in the diffraction pattern.

The intensity of the peaks in the diffraction pattern can be analysed to determine the crystal structure. In contrast to SCXRD, there can be significant peak overlap in XRPD which makes solving crystal structures from XRPD more challenging. X-ray powder diffraction (XRPD) data were collected for this thesis using a PANalytical Empyrean diffractometer with Cu $K\alpha_1$ radiation (with a Ge monochromator), an X'Celerator detector and an Oxford Cryosystems Phenix cryostat.

2.2.2 Neutron Powder Diffraction

Neutron powder diffraction (NPD), in which neutrons are scattered by a sample, can give complementary information to XRPD. Neutrons, being uncharged particles with momentum, energy, and spin, can be propelled towards a sample and diffracted. Whilst X-rays are scattered by the electron cloud of an atom (making X-rays relatively insensitive to light elements), neutrons are scattered by the nuclei of the atoms and have scattering lengths dependant on the isotope. This gives greater sensitivity to lighter elements (such as oxygen and fluorine) than XRPD.

2.2.2.1 Time-of-Flight Neutron Powder Diffraction

Due to the principle of wave-particle duality, neutrons have an associated wavelength. By timing the neutrons over a fixed path length L , their velocity can be determined. This allows for the wavelength λ of the neutron to be calculated, using de Bröglie equation. Applying the de Broglie equation with the Bragg equation gives:

$$\lambda = ht / mL = 2d \sin\theta$$

where, L is the path length, m is the mass of the neutron, t is the time-of-flight and h is Planck's constant.

Time-of-flight neutron powder diffraction can use spallation neutron sources, where pulses of neutrons are produced with a broad band of wavelengths. The neutrons are diffracted by the sample and are detected by banks of detectors. This allows for simultaneous collection of diffraction patterns over large ranges of d spacing. The speed at which this data collection can take place allows for in-situ analysis, for example, the application of heat or mechanical stress on the material.

Medium resolution neutron powder diffraction data for the $\text{Bi}_2\text{CoO}_2\text{F}_4$ characterisation section of this thesis were collected at the ISIS Neutron and Muon Source using the General Materials (GEM) Diffractometer. It is a good-resolution, high flux, low-background time-of-flight neutron powder diffractometer for crystalline materials, with a wide-angular (Q) range and high-count rate which allows in-situ sample study under varying conditions such as temperature, pressure and chemical reaction.⁴⁸

2.2.2.2 Magnetic Structure Determination from Neutron Powder Diffraction data

Neutrons carry a spin, and therefore have a magnetic moment which can interact with orbital or spin magnetic moments in samples. In addition to nuclear scattering, neutrons can also be scattered by long-range ordering of magnetic moments within a sample. This magnetic scattering depends on the site, the magnitude and the orientation of ordered magnetic moments in the sample. These magnetic Bragg peaks can therefore be used to determine possible magnetic structures consistent with the nuclear symmetry and the NPD data below a magnetic ordering transition. In this work, ISODISTORT^{49,50} was used to explore possible magnetic structures.

2.2.3 Rietveld Refinement Analysis

To overcome the challenges in extracting structural information from Bragg intensities in powder diffraction patterns due to peak overlap, the Rietveld method was developed in the 1960s. This method involves the least-square-refinement of a good starting model to give a good fit of the calculated diffraction pattern for this model to the observed diffraction pattern. This method considers the structural model and instrumental factors and other features that can be modelled if wished.

The least-square refinement is systemically done using the following equation:

$$S_y = \sum_i w_i (y_i - y_{ci})^2$$

where, y_{ci} is the calculated intensity at the i^{th} step, y_i is the observed intensity at the i^{th} step and w_i is equal to $1/y_i$.

Several equations have been developed to measure the quality of the fit, see *Table 2.2.1*. The R factors give an indication of how good the fit is between the observed and calculated diffraction patterns and can consider the number of data points and the number of refined parameters. The R-factor equations are also useful as an indication of the progress after each iteration, which is necessary to make sure the refinement is converging or has reached an end point.

Table 2.2.1 - R-factor equations used to quantify the fit in a Rietveld refinement.

Corresponding R-factor	Equation
R-structure factor	$R_F = \frac{\sum (I_K('obs'))^{1/2} - (I_K(calc))^{1/2} }{\sum (I_K('obs'))^{1/2}}$
R-Bragg factor	$R_B = \frac{\sum I_K('obs') - I_K(calc) }{\sum I_K('obs')}$
R-pattern	$R_P = \frac{\sum y_i(obs) - y_i(calc) }{\sum y_i(obs)}$
R-weighted pattern	$R_{wp} = \left\{ \frac{\sum w_i (y_i(obs) - y_i(calc))^2}{\sum w_i (y_i(obs))^2} \right\}$

The most widely used R-factor in powder diffraction is the weighted pattern R-factor, R_{wp} . However, R_{wp} does not take in to account the number of parameters nor the number of constraints in the calculations. The expected R-factor, R_{exp} , can also be calculated:

$$R_{exp} = \left[\frac{N - P + C}{\sum w_i y_{oi}^2} \right]^{1/2}$$

with $N - P$ representing the number of data points minus the number of varied parameters and C is the number of constraints.

The ratio between these two R-factors will give chi-squared values.

$$\chi^2 = (R_{wp}/R_{EXP})^2$$

For χ^2 and (goodness of fit), the statistics determine that the lower the value, the better the fit, however, but value should never fall below 1. These statistics will be extremely useful in determining the model with the best fit and the quality of our Rietveld refinements of crystal and magnetic structures in this report.

2.2.4 Pawley Method

The Pawley method is another whole pattern fitting least-squares procedure. The main difference between this method and the Rietveld method is the Pawley method does not rely on a model to fit to the data and depends only on the unit cell size and symmetry. This makes it useful to compare possible space groups before full Rietveld analysis is carried out.

2.2.5 ISODISTORT

ISODISTORT^{49,50} is an online tool for exploring structural and magnetic distortions. This powerful tool, once given a parent phase, will allow the user to explore the symmetry relationships between the parent phase and lower-symmetry phases. This is helpful for exploring structural distortions and determining lower symmetry subgroups. The software can apply displacive, occupational, magnetic, and rotational modes as desired to existing materials.

2.2.6 X-Ray Absorption Near-Edge Structure (XANES) Analysis

X-ray Absorption Near-Edge Structure (XANES) and Extended X-ray Absorption Fine Structure (EXAFS) are subsets of X-ray Absorption Spectroscopy. Here we shall discuss only the XANES methodology as it is used in this research.

X-rays are ionizing radiation that have sufficient energy to excite core electrons to a higher energy state (the excited state). In XANES, as the x-ray beam is fired at the sample, the core electrons absorb radiation at specific energies and the observed absorption edges correspond to specific electronic transitions. The absorption edge is described in terms of the principal quantum number, e.g., the K-edge corresponds to the excitation of 1s electrons, the L-edge corresponds to excitation of electrons in the 2s and 2p orbitals.

The absorption edge in XANES is dependent on the oxidation state of the element being investigated: higher oxidation states require more energy for excitation, increasing the absorption edge energy. XANES data can be assessed quantitatively to investigate oxidation states by comparing an element's edge in a sample with reference data of the same element in several oxidation states. The pre-edge can be used to determine the coordination of the target element in a material because the geometry of an atom's coordination environment can alter the scattering pathways.

The absorption edge and features within 50 eV of the edge and the pre-edge are investigated in X-ray Absorption Near Edge Structure (XANES) whereas the oscillatory structure beyond this is referred to as the Extended X-ray Absorption Fine Structure (EXAFS).

The XANES data collected for the $\text{Bi}_2\text{CoO}_2\text{F}_4$ sample in this report was done simultaneously with a cobalt metal foil. A shift was applied to both the sample and its associated foil's data, such that the 1st peak in the derivative of the foil's spectrum occurs at the same energy as the reference metal foil data, i.e. at 7708.9 eV.⁵¹ This is to standardise all sample and reference data to the same energy level for proper comparison and evaluation.

2.2.7 Second Harmonic Generation

Second Harmonic Generation (SHG) is a second-order non-linear optical process where two photons of the same frequency (usually produced by a laser) interact with a non-linear material and combine to a new photon with half the wavelength and twice the frequency, i.e., doubling the energy. Materials that behave this way are SHG active. This phenomenon only happens in non-linear materials, and so is not allowed by materials with an inversion symmetry. Among other uses, such as characterisation of biological tissues,⁵² it can be a good tool for determining whether or not a crystal has inversion symmetry (and therefore whether it might be non-centrosymmetric). All polar materials are non-centrosymmetric and so materials that adopt polar crystal structures must also be SHG active, but not all SHG active materials are polar.⁵³

CHAPTER THREE

Characterisation of $\text{Bi}_2\text{CoO}_2\text{F}_4$

3.1 Background

The recently reported oxide-fluoride $\text{Bi}_2\text{CoO}_2\text{F}_4$, prepared through a hydrothermal synthesis route, is a low oxidation state cobalt (Co^{2+}) $n=1$ oxide fluoride Aurivillius phase and the first Aurivillius phase with only magnetic B site cations.⁴⁷ This material has been synthesised and characterised, by Vagourdi et al, through single-crystal X-ray diffraction and Raman scattering between 10 – 300 K. This analysis work suggested that the material crystallises in the centrosymmetric tetragonal space group, $I\bar{4}$ with lattice parameters of $a = 3.843(2)$ Å and $c = 16.341(8)$ Å and takes up the structure of a $n = 1$ Aurivillius phase. XRD of the $\text{Bi}_2\text{CoO}_2\text{F}_4$ shows positional disordering of the anion sites, with equatorial and apical sites in the perovskite block split into lower symmetry 4-fold sites. (Figure 3.1.1)

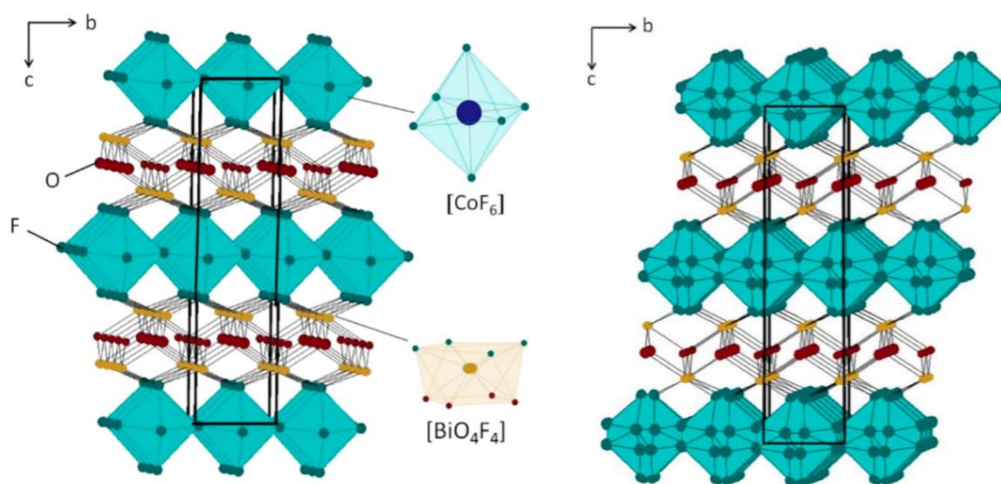


Figure 3.1.1 – (left) The ideal high symmetry structure of the $n = 1$ Aurivillius phase, $\text{Bi}_2\text{CoO}_2\text{F}_4$, and (right) the observed structure of $\text{Bi}_2\text{CoO}_2\text{F}_4$ through X-ray diffraction, showing a 4-fold split of F^- anion positions. Reproduced from reference⁴⁷.

Raman data collected on cooling from 300 K to 10 K showed a transformation of broad nodes to sharp nodes indicating that as temperature decreases, the structure becomes more ordered. The transition between ordered and disordered comes as a gradual freezing of rotational degrees of freedom at lower temperatures.

Heat capacity and magnetic susceptibility measurements of $\text{Bi}_2\text{CoO}_2\text{F}_4$ showed that below the Néel temperature of ~ 50 K there were indications of long-range antiferromagnetic ordering. Inverse magnetic susceptibilities of $\text{Bi}_2\text{CoO}_2\text{F}_4$ measured at magnetic fields of 5 T and 7 T above 150 K showed an effective magnetic moment of $5.62(5) \mu_B$ per Co^{2+} cation and a Curie–Weiss temperature of $142(2)$ K. This is further confirmed by a maximum in susceptibility at high magnetic fields, indicating long range antiferromagnetic ordering. However, at lower magnetic fields and at ~ 40 K anomalies occur which may suggest the development of ferro or ferrimagnetism, due to some spontaneous magnetisation. Details of the exchange paths have not been determined, but the finite interlayer coupling eventually causes long-range ordering below ~ 50 K.⁴⁷

3.2 Aims

Our research builds on the characterisation measurements reported by Vagourdi et al:⁴⁷ we characterised their sample using neutron powder diffraction (NPD). NPD is relatively more sensitive to the positions of light ions (e.g., F⁻ and O²⁻) in the presence of heavy ions, than XRPD, and so, will be used to investigate the long-range structural distortions brought on by the tilts/rotations of the Co(O,F)₆ octahedra.

An interest lies in determining the distribution of oxide and fluoride ions over the anion sites, but they have almost identical X-ray and neutron scattering lengths (neutron scattering lengths for oxygen; $b_c = 5.803(4)$ fm, and for fluorine; $b_c = 5.654(12)$ fm⁵⁴). Bond valence sum analysis^{55,56} could be used to give an indication of how favourable a particular anion arrangement might be. However, this relies on accurate experimental bond lengths, ideally from analysis of the NPD data.

Magnetic susceptibility measurements suggested long-range antiferromagnetic ordering at temperatures below ~50 K, we attempted to determine this magnetic structure from analysis of low temperature neutron powder diffraction data.

These neutron powder diffraction studies will be complemented by second-harmonic generation tests to determine whether the structure is centrosymmetric, as well as XANES data to determine the cobalt oxidation state and confirm the stoichiometry of the material.

3.3 Experimental Method

Pink polycrystalline samples of Bi₂CoO₂F₄ were made hydrothermally by E. Vagourdi, as described previously.⁴⁷ Variable temperature X-ray powder diffraction (XRPD) data were collected by Dr V. A. Cascos using a PANalytical Empyrean diffractometer with Cu K α 1 radiation (with a Ge monochromator), an X'Celerator detector and an Oxford Cryosystems Phenix cryostat. 20-minute scans were collected at 20 K intervals on warming from 12 K to 300 K, with dwell times of 10 minutes for temperature equilibration before each scan.

Neutron powder diffraction (NPD) data were collected at the ISIS neutron and muon source by Dr V. A. Cascos and Dr E. E. McCabe. One batch (0.84 g) was used to collect medium resolution NPD data on the GEM diffractometer: the sample was placed in a cylindrical vanadium sample can (of diameter 6 mm) to a height of ~1 mm and data were collected at 50 K and at 5 K. Powder diffraction data were analysed using TopasAcademic software^{57,58} and ISODISTORT⁴⁹ was used to explore possible structural distortions and magnetic ordering arrangements.

The cobalt K-edge X-ray absorption spectra were collected by continuous scanning (QEXAFS) on beamline B18-CORE XAS at the Diamond Light Source at the Harwell Science and Innovation Campus in Oxfordshire.⁵⁹ The synchrotron energy and current were 3 GeV and 298.7 mA, respectively. Athena was used to normalise spectra.⁶⁰

3.4 Structural Refinement Using X-ray Powder Diffraction Data

Structural refinements were carried out using XRPD data collected for Bi₂CoO₂F₄. There are three anion sites in the main phase, two in the perovskite layer, and one in the fluorite layer these sites are labelled O(ap.), O(eq.) and O(fl.) displayed in *Figure 3.4.1*. No attempt was made to distinguish between O²⁻ and F⁻ ions within the XRPD refinements as both anions are isoelectronic.

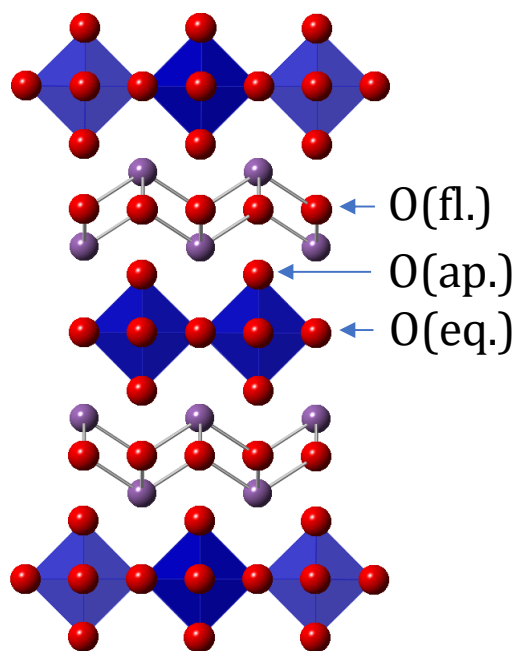


Figure 3.4.1– Representation of types of anionic sites in the Aurivillius structure. Anion sites are shown by red spheres whilst bismuth is represented by purple spheres and CoX₆ octahedra are shown in blue, shading indicates depth.

These preliminary Rietveld refinements using XRPD data indicated that the main peaks were consistent with an $n = 1$ Aurivillius phase. An impurity Bi₇F₁₁O₅ (14.4 (6) % by mass) was also detected (Figure 3.4.2a). Pawley fits of the Bi₂CoO₂F₄ XRPD data were done to compare refinements between an orthorhombic unit cell (Figure 3.4.2b) and a tetragonal unit cell (Appendix A.1). The orthorhombic symmetry gave a better fit to the data indicating a lower symmetry model may be better for describing the structure.

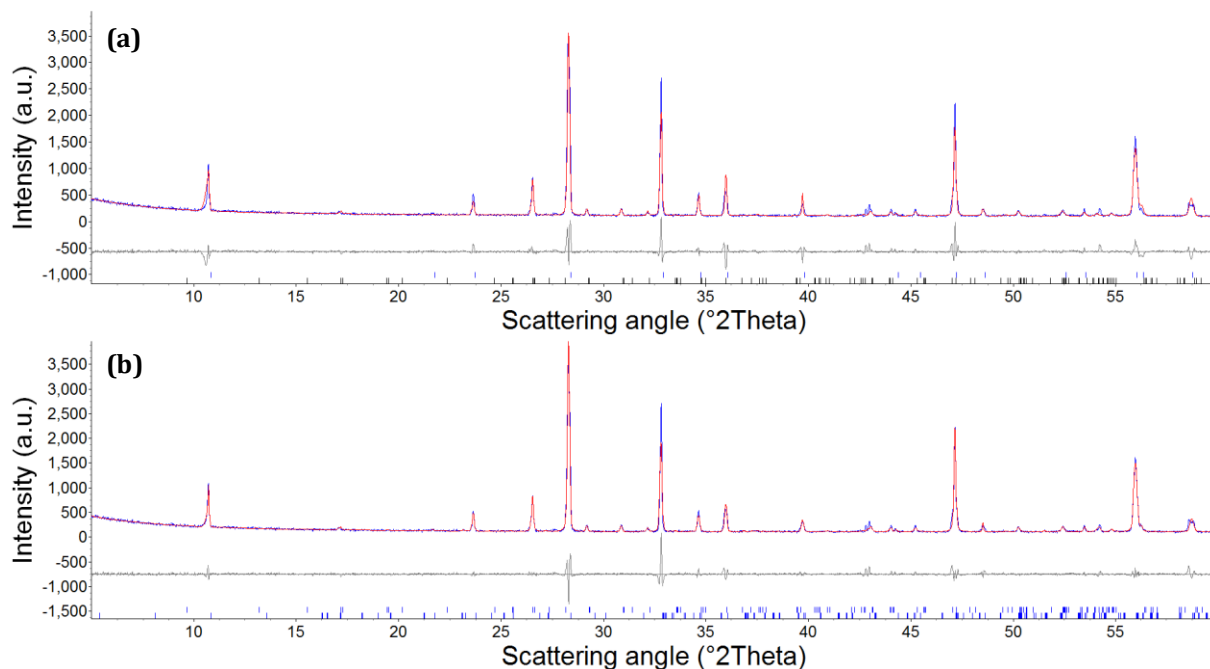


Figure 3.4.2 – Observed (-), calculated (-) and difference (-) profiles from refinements using room temperature XRPD data for Bi₂CoO₂F₄. (a) Rietveld refinement using Tetragonal I4/mmm, $a = 3.8455(1) \text{ \AA}$, $c = 16.316(1) \text{ \AA}$, $R_{wp} = 13.36\%$, $R_p = 9.14\%$ and (b) Pawley refinements using Orthorhombic P222, $a = 5.4331(5)$, $b = 5.4428(6)$, $c = 32.633(3)$, $R_{wp} = 11.00\%$, $R_p = 7.71\%$, $\chi^2 = 2.37$; reflection positions of main phase and Bi₇F₁₁O₅ (14.4(6) % by mass) are marked by upper blue ticks and lower black ticks, respectively,

3.4.1 Variable temperature XRPD

Sequential Pawley refinements, using an orthorhombic $P222$, $c \times \sqrt{2}a \times \sqrt{2}a'$ unit cell, on $\text{Bi}_2\text{CoO}_2\text{F}_4$ XRPD data collected between 20 and 290 K were carried out to determine unit cell parameters as a function of temperature (Figure 3.4.3).

Lattice parameters and unit cell volume increased smoothly with temperature as expected. However, between the temperatures of 50 – 100 K a slight change in slope of unit cell parameters a and b occurs which could suggest a structural change.

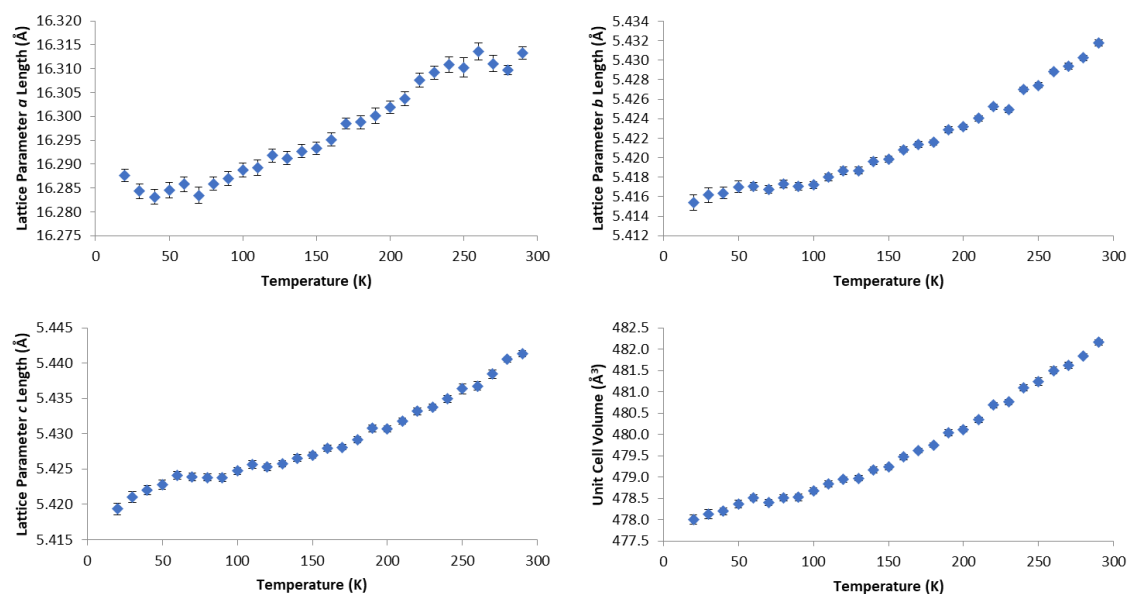


Figure 3.4.3 - Graph depicting the change in lattice parameters a , b and c (measured in Å) and Volume (measured in Å³) as a function of temperature (K), data collected from Variable Temperature XRPD of $\text{Bi}_2\text{CoO}_2\text{F}_4$, using an orthorhombic $P222$ space group as a model, between 20 K and 290 K, with error bars.

3.5 Investigation of Co Oxidation State Through XANES/EXAFS Data

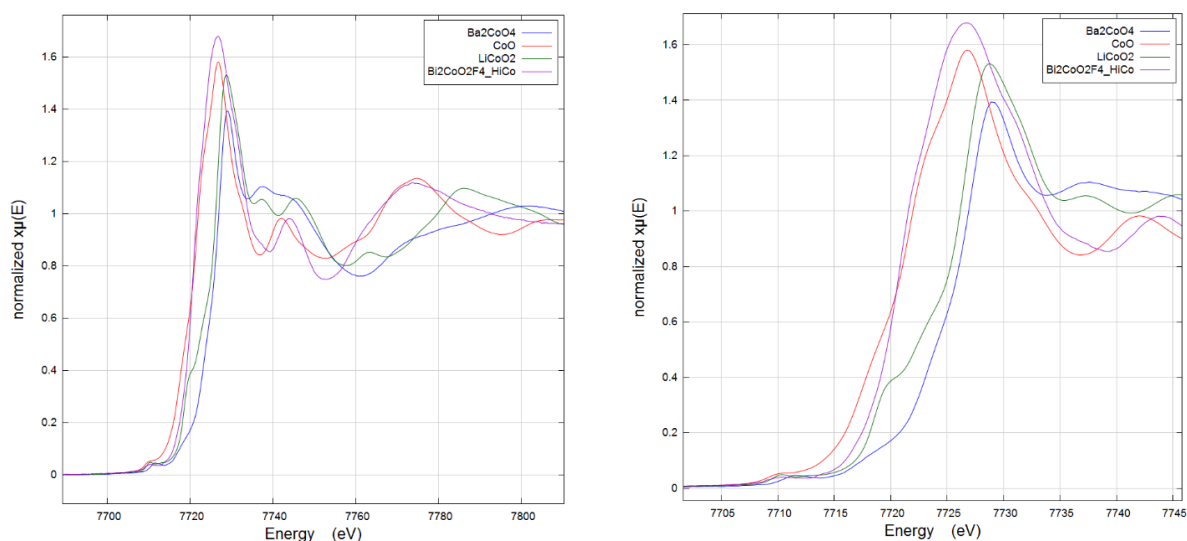


Figure 3.5.1 – (left) full view and (right) enhanced view of X-ray absorption near-edge structure of $\text{Bi}_2\text{CoO}_2\text{F}_4$ data. Observed data marked by purple lines, with reference data; CoO (red), LiCoO_2 (green) and Ba_2CoO_4 (blue).

X-ray absorption near-edge structure data was obtained for $\text{Bi}_2\text{CoO}_2\text{F}_4$ to investigate the oxidation state of cobalt. Figure 3.5.1 shows the Co K-edge data for $\text{Bi}_2\text{CoO}_2\text{F}_4$ together with the reference data for CoO, LiCoO_2 and Ba_2CoO_4 . By comparing the pre-edge and rising edge of the XANES and subsequent reference data, we can determine the likely oxidation state of the B site cation. The reference data represents the increasing oxidation state which is possible by Co; CoO (Co^{2+}), LiCoO_2 (Co^{3+}) and Ba_2CoO_4 (Co^{4+}).

Figure 3.5.2 shows only the $\text{Bi}_2\text{CoO}_2\text{F}_4$ and CoO reference data illustrating the similar positions of the rising edge (~ 7726.8 eV) and shape for both materials. This suggests that the cobalt oxidation state in $\text{Bi}_2\text{CoO}_2\text{F}_4$ is close to +2. However, the anion sites coordinated around the cobalt is thought to be occupied by the more electronegative F^- rather than O^{2-} , which is likely to increase the Co K-edge energy.⁶¹ This would indicate that the oxidation state of Co would be slightly lower than thought, which is consistent with vacancies in the anion sublattice. Further comparisons with cobalt fluoride references are needed to confirm this.

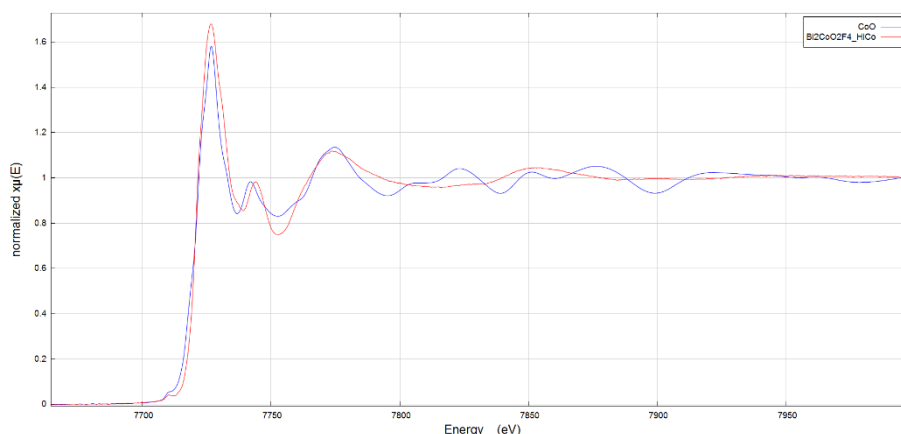


Figure 3.5.2 – X-ray absorption near-edge structure of $\text{Bi}_2\text{CoO}_2\text{F}_4$ data, marked by red lines, with reference data; CoO (blue).

3.6 Structural Refinement Using 50 K Neutron Powder Diffraction Data

Here we discuss the 50 K NPD analysis of $\text{Bi}_2\text{CoO}_2\text{F}_4$. Firstly, a Rietveld refinement was carried out using the ideal $I4/mmm$ structure as a starting model. All anion sites were modelled as oxygen, no attempt was made to differentiate between anion occupancy at this stage due to the almost identical neutron scattering lengths of fluorine and oxygen.⁵⁴

The refinement profiles are given in *Figure 3.6.1a*. The refinement showed the main peaks are well matched to an $n = 1$ Aurivillius phase. However, unindexed reflections (e.g., at 16200 μs , 15480 μs , 12450 μs and 11770 μs) are observed.

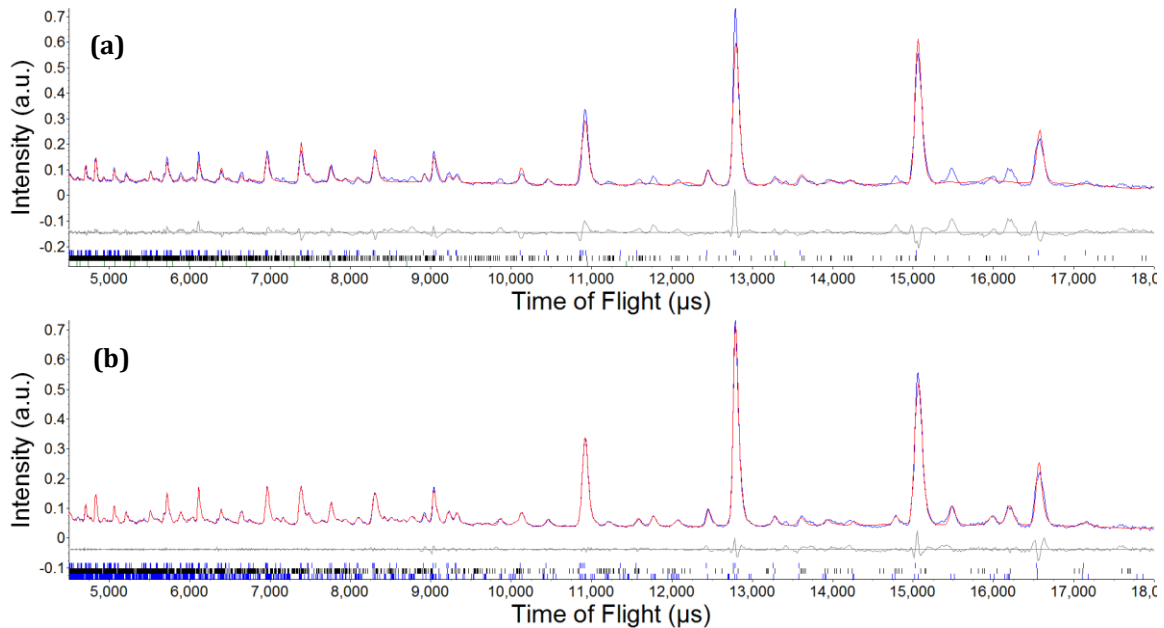


Figure 3.6.1 – Observed (-), calculated (-) and difference (-) profiles from refinements using 50 K NPD data of $\text{Bi}_2\text{CoO}_2\text{F}_4$. (a) Rietveld refinement using tetragonal $I4/mmm$ model, $a = 3.8422(3) \text{ \AA}$, $c = 16.354(2) \text{ \AA}$, $R_{wp} = 9.77\%$, $R_p = 6.82\%$, $\chi^2 = 6.89$; and (b) $I4/mmm$ Rietveld Phase with a Pawley phase using orthorhombic $P222$ model, $a = 5.447(6)$, $b = 5.427(6) \text{ \AA}$, $c = 16.37(2)$, $R_{wp} = 7.57\%$, $R_p = 6.02\%$, $\chi^2 = 6.38$. Reflection positions of main phase and $\text{Bi}_7\text{F}_{11}\text{O}_5$ (8(2) % by weight) are marked by upper blue ticks and middle black ticks, respectively.

3.6.1 Determination of the Lattice Parameters

To index the diffraction patterns, Pawley refinements were carried out using tetragonal and orthorhombic unit cells of $P4$, $P222$, $I222$ and $C222$ symmetries, with various a , b and c lattice parameters; refinement profiles can be found in *Appendix A.3*.

The Pawley refinements indicated that $\sqrt{2}a \times \sqrt{2}a' \times c$ unit cells (relative to the ideal $I4/mmm$ structure) and lowering of symmetry (for example, due to rotations of the octahedra), indexed extra peaks giving a better fit than the $I4/mmm$ structure. Larger unit cells (e.g., $2a \times 2a \times c$; $\sqrt{2}a \times \sqrt{2}a \times 2c$ and their orthorhombic equivalents) were considered but did not give a further improvement of fit. *Figure 3.61(b)* shows a refinement using an $I4/mmm$ Rietveld Phase with a Pawley phase of $P222$ symmetry with $\sqrt{2}a \times \sqrt{2}a' \times c$ unit cell fitting the unindexed reflections.

3.6.2 Determination of Distortions in Octahedra and Fluorite-Like Layers

Symmetry analysis was carried out using ISODISTORT software.^{49,50} The software was used to map out the symmetries which can describe the structures of distorted $n = 1$ Aurivillius phases with distortions arising from tilts, rotations and displacements (*Figure 3.6.3*) corresponding to the modes X_3^+ , X_2^+ and Γ_5^- ; this is visualised in *Figure 3.6.2*. These distortion modes correspond to rotations of the BX_6 octahedra about in-plane axes, about the out-of-plane axis and in-plane polar distortions, respectively.

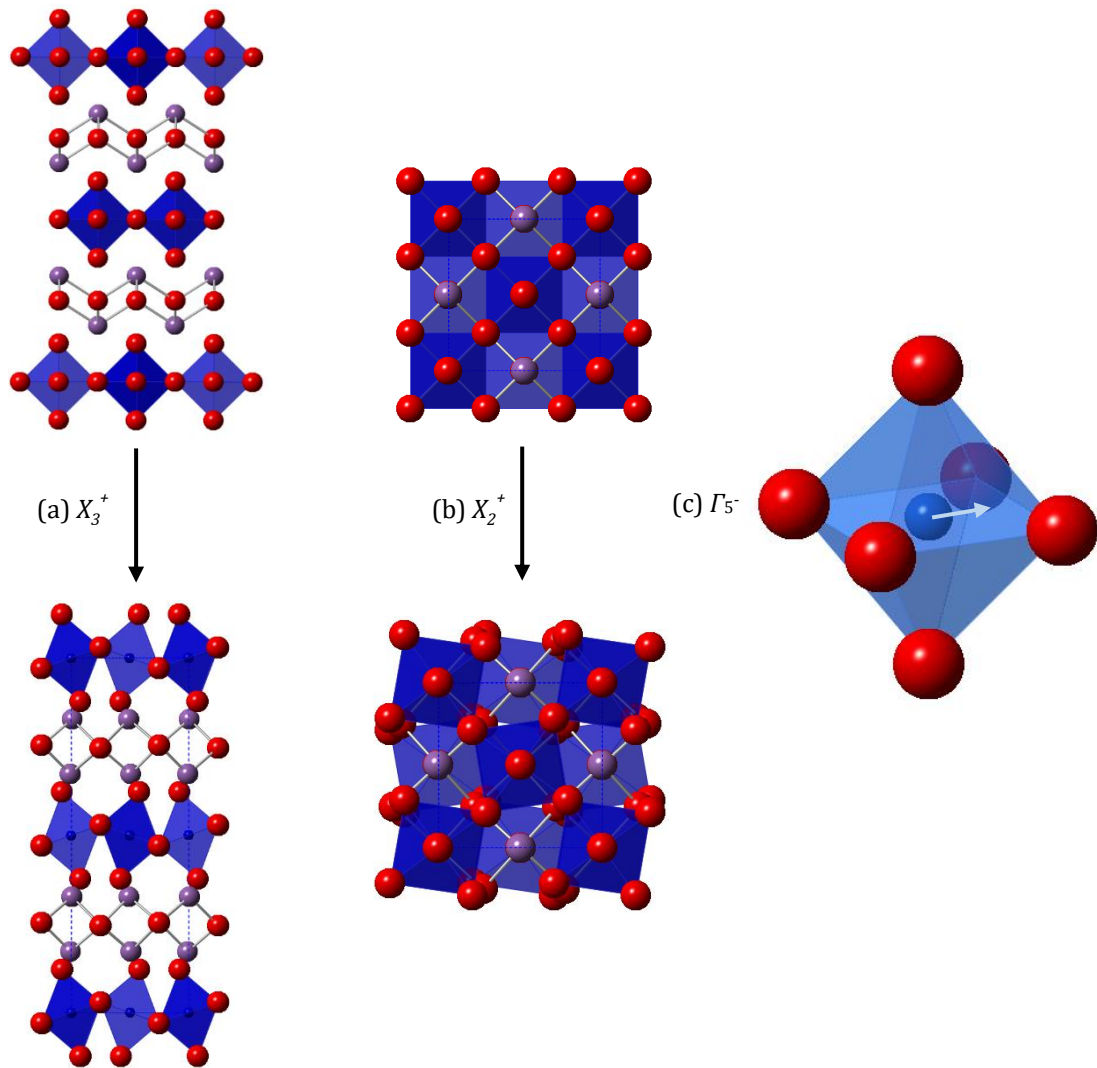


Figure 3.6.2 - Illustration of examples of rotations which can take place on the perovskite layer of an $n = 1$ Aurivillius phase. (a) Represents the rotations about the short in-plane axis which come about through X_3^+ modes, (b) represents the rotations about the long out-of-plane axis which come about through X_2^+ modes and (c) illustrates the off-centre displacement of the B-site cation which is associated with the Γ_5^- modes.

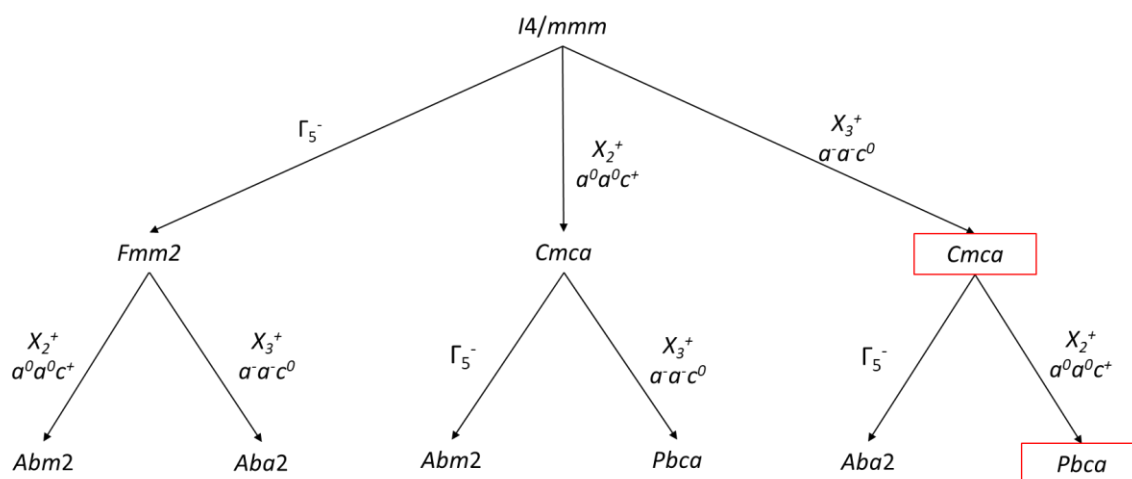


Figure 3.6.3 - Preliminary symmetry analysis using ISODISTORT showing types of distortions that $\text{Bi}_2\text{CoO}_2\text{F}_4$ can undergo with respect to the $I4/mmm$ space group. Irreducible representation is indicated by figures quoted on arms of symmetry map followed by respective Space group and glazer notation, showing extent of distortion.

ISODISTORT^{49,50} was used to obtain a description of a low symmetry model in terms of the parent $I4/mmm$ structure with distortions applied. The amplitudes of these distortions could then be refined to describe lower-symmetry distorted structures.

3.6.3 Mode Inclusion Simulated Annealing

The “mode inclusion method”⁶² was used to consider possible structural distortions in terms of the improvement of fit between the calculated and observed diffraction patterns. Possible distorted structures can be described in terms of the high symmetry $I4/mmm$ structure with various symmetry-adapted distortion modes applied. The amplitudes of these modes can be refined to give distorted structures.^{49,50} The mode inclusion method involves carrying out rounds of simulated annealing as modes are added individually (or in groups) to the refinement, and the R_{wp} of the best solution from each round of simulated annealing output. This allows the improvement in fit from individual or from several (grouped by symmetry) modes to be determined.⁶² These R_{wp} values for each mode or sets of modes are displayed by Figure 3.6.4.

The first round of refinements (Figure 3.6.4a), indicated that the best fit was obtained when the X_3^+ modes were included (R_{wp} decreases to 11.41% from 18.96%). The X_3^+ mode amplitude describes rotations of the BX_6 octahedra about the short in-plane axes (i.e., in Glazer notation: $a-a-c^0$).

A second cycle of simulations (Figure 3.6.4b) including all X_3^+ modes indicated that including X_2^+ modes (in addition to X_3^+) further improved the fit (R_{wp} decreased to 8.70%). The X_2^+ mode amplitude describes rotations of the BX_6 octahedra about the long out-of-plane axis (i.e., in Glazer notation: $a^0a^0c^+$)

To rule out the possibility of another symmetry element being present in the structure, a third simulation was made where X_3^+ and X_2^+ modes were included (Figure 3.6.4c). The results showed little further improvement in fit, suggesting that no other modes were necessary to describe the structure.

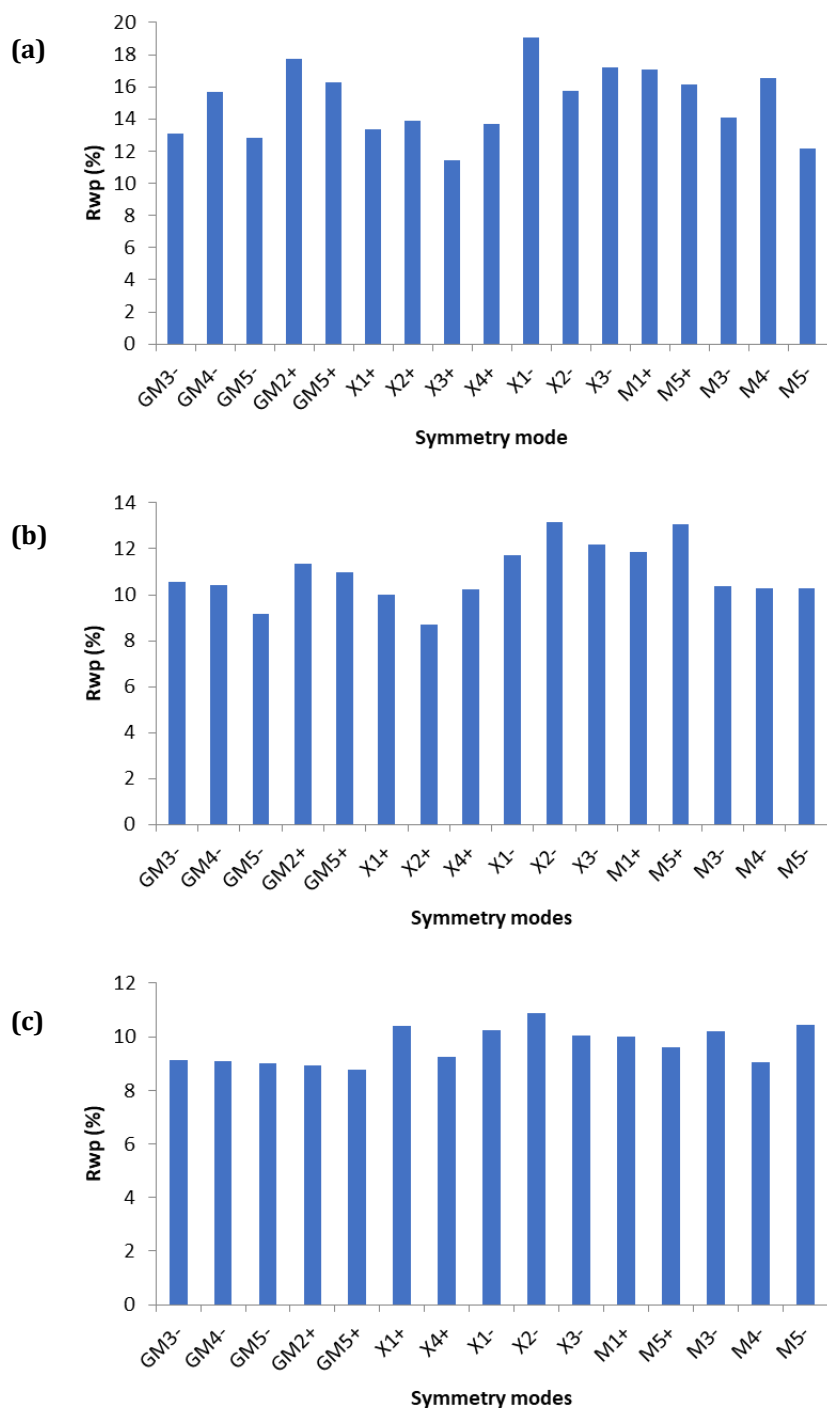


Figure 3.6.4 – Graphs representing: (first) the refinements details from the first round of the mode inclusion simulated annealing, (second) the refinements details from the second round of the mode inclusion simulated annealing with X_{3^+} modes included, (third) the refinements details from the third round of the mode inclusion simulated annealing with X_{3^+} and X_{2^+} modes included.

3.6.4 Pawley Refinements Using Low Symmetry Models

The mode inclusion analysis described above identified X_{3^+} and X_{2^+} modes as the most important to describe the distorted structure and the symmetry map shown in Figure 3.6.2 indicates that this model is expected to be of $Pbca$ symmetry. Fits to unit cells of $Cmca$ symmetry (X_{3^+} only) and $Pbca$ symmetry ($X_{3^+} + X_{2^+}$) were compared by Pawley refinements and the cell of $Pbca$ symmetry (Figure 3.6.5b) gave the better Pawley fit

to the data. The distorted structure is thought to include $a-a-c^+/-$ tilts. Refinements profiles using the space groups $Fmm2$, $Abm2$ and $Aba2$ as models can be found in *Appendix A.4*.

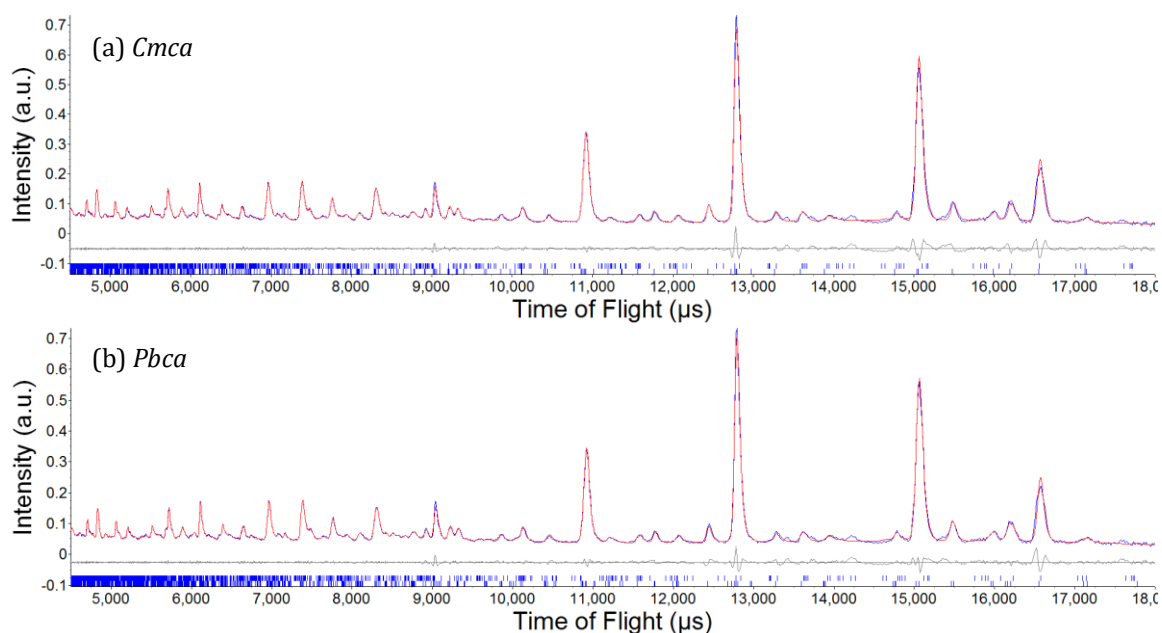


Figure 3.6.5 – Pawley refinements using high resolution banks of data showing observed (-), calculated (-) and difference (-) profiles using NPD data of $\text{Bi}_2\text{CoO}_2\text{F}_4$ with respect to (a) Orthorhombic $Cmca$, $R_{wp} = 5.21\%$, $R_p = 4.17\%$, $\chi^2 = 3.53$ and (b) Orthorhombic $Pbca$, $R_{wp} = 4.79\%$, $R_p = 3.77\%$, $\chi^2 = 4.50$. The impurity phase, $\text{Bi}_7\text{F}_{11}\text{O}_5$, and Pawley phase of $Cmca/Pbca$ symmetry are marked by upper blue ticks and lower blue ticks, respectively.

3.6.5 Rietveld Refinement of $\text{Bi}_2\text{CoO}_2\text{F}_4$

Here we discuss the Rietveld refinement of the NPD data using the lower symmetry space groups than the reported $I4/mmm$ model. Details of Rietveld refinements using the other models can be found in *Appendix A.5* for comparison.

3.6.5.1 Refinement of $Cmca$ model

Refinement profiles of $Cmca$ Rietveld refinement are given in *Figure 3.6.6*. There was a noticeable improvement in the refinement with the indexed peaks in comparison to the ideal higher symmetry $I4/mmm$ model, giving a R_{wp} value of 6.98%. This model allows for out of phase octahedral rotations about an axis in the ab plane and the octahedra are very slightly distorted, illustrated by *Figure 3.6.7*.

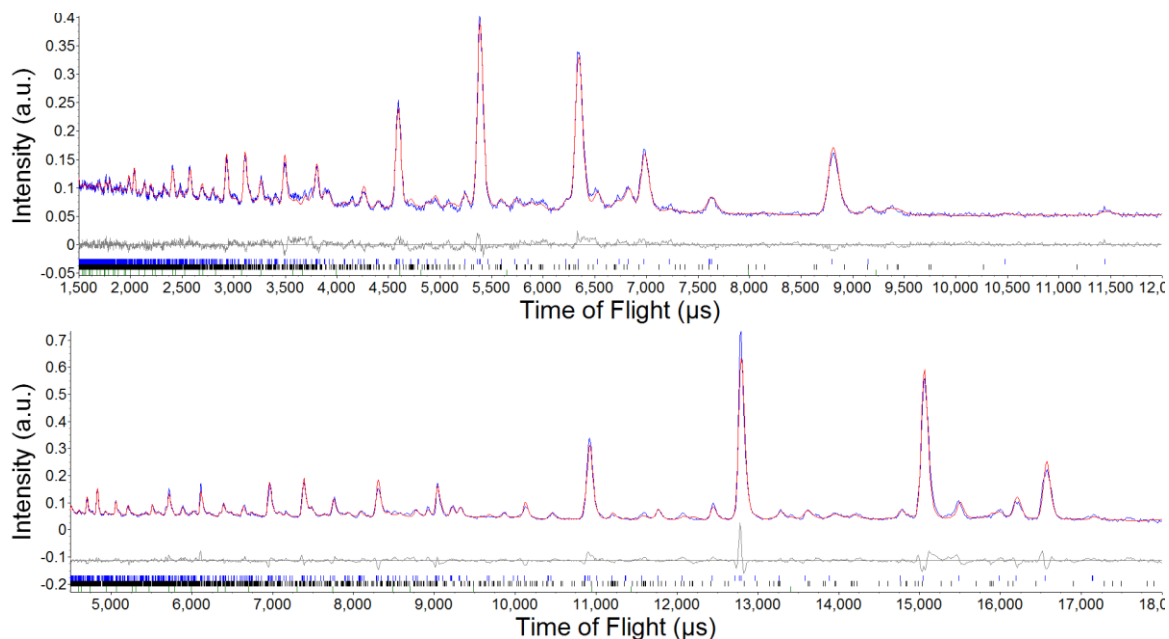


Figure 3.6.6 - Observed (-), calculated (-) and difference (-) profiles from Rietveld refinement using (top) bank 3 and (bottom) bank 5 of the 50 K NPD data of $\text{Bi}_2\text{CoO}_2\text{F}_4$. Cmca , $a = 5.434(5) \text{ \AA}$, $b = 16.350(1) \text{ \AA}$, $c = 5.4352(6) \text{ \AA}$, $R_{\text{wp}} = 6.98\%$, $R_p = 5.05\%$, $\chi^2 = 3.52$. Reflection positions of main phase and $\text{Bi}_7\text{F}_{11}\text{O}_5$ are marked by lower black ticks and upper blue ticks, respectively.

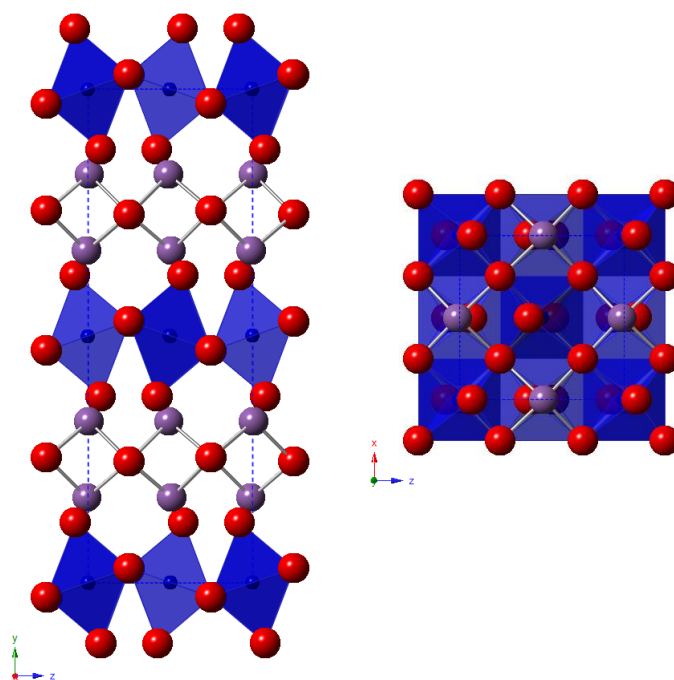


Figure 3.6.7- Representation of Cmca space group of $\text{Bi}_2\text{CoO}_2\text{F}_4$, allowing rotations of octahedra about the in-plane axis only. Oxide/fluoride anions (red) take up positions in the apical/equatorial anion sites in the perovskite octahedra and the anions sites in the fluorite-like layer, bismuth (purple) lies in the fluorite layer and cobalt (blue) is positioned within the perovskite block.

Details of the refinement are given in *Table 3.6.1*; with selected bond lengths given in *Table 3.6.2*. Fractional occupancies were fixed at 1 throughout the refinements. The refined model here revealed limitations of the model: the equatorial anion site had high atomic displacement parameters. This could reflect either static or dynamic displacements of the equatorial anion away from its ideal $8e$ site or could indicate some vacancies on this site.

Table 3.6.1 – Details from refinement in space group *Cmca* using 50 K NPD data for $\text{Bi}_2\text{CoO}_2\text{F}_4$; $a = 5.434(5)$ Å, $b = 16.350(1)$ Å, $c = 5.4352(6)$ Å, $R_{wp} = 6.98\%$, $R_p = 5.05\%$, $\chi^2 = 3.52$.

Atom	X	y	z	Occupancy	Beq (Å ²)	Site
Bi	0.0	0.3272(1)	0.0075(6)	1	0.37(4)	8f
Co	0.0	0.0	0.0	1	0.1(1)	4a
O(eq.)	0.25	0.5294(5)	0.25	1	7.4(2)	8e
O(ap.)	0.0	0.12209(2)	0.9129(9)	1	1.4(1)	8f
O(fl.)	0.25	0.7462(3)	0.25	1	0.48(4)	8e

Table 3.6.2 – Selected bond lengths for $\text{Bi}_2\text{CoO}_2\text{F}_4$ from NPD refinements in space group *Cmca*.

Bond	Lengths in Å at 50 K	Bond	Lengths in Å at 50 K
Bi – O(fl.)	2 x 2.291(4)	Bi – O(eq.)	2 x 3.050(6)
Bi – O(fl.)	2 x 2.309(6)	Co – O(eq.)	4 x 1.981(2)
Bi – O(ap.)	1 x 2.400(5)	Co – O(ap.)	2 x 2.041(4)
Bi – O(ap.)	2 x 2.867(1)		

3.6.5.2 Refinement of disordered *Cmca* model

Moving the equatorial anion to the general $16g$ site (and halving the site occupancy) to give a disordered model of *Cmca* symmetry improved the fit (R_{wp} decreased from 6.98% to 6.55% for 2 additional parameters) and gave a much lower atomic displacement parameter (ADP), (Table 3.6.3). The refinement profiles are given by Figure 3.6.8. The details and the selected bond lengths of the refinement are given by Table 3.6.3 and Table 3.6.4, respectively.

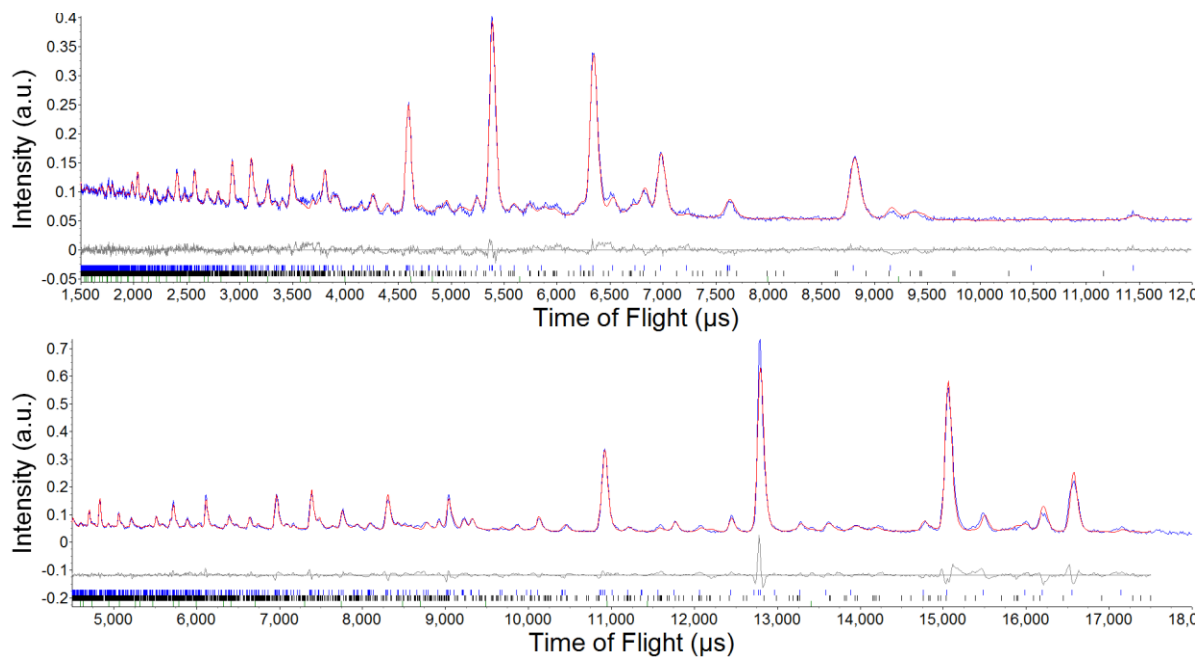


Figure 3.6.8 - Observed (-), calculated (-) and difference (-) profiles from Rietveld refinement using (top) bank 3 and (bottom) bank 5 of the 50 K NPD data of $\text{Bi}_2\text{CoO}_2\text{F}_4$. Cmca with disordered $O(1)$ anion site, $a = 5.434(5) \text{ \AA}$, $b = 16.350(1) \text{ \AA}$, $c = 5.4352(6) \text{ \AA}$, $R_{\text{wp}} = 6.55\%$, $R_p = 4.69\%$, $\chi^2 = 3.13$. Reflection positions of main phase and $\text{Bi}_7\text{F}_{11}\text{O}_5$ are marked by lower black ticks and upper blue ticks, respectively.

Table 3.6.3 – Details from refinement in space group *Cmca* with a disordered *O*(eq) site using 50 K NPD data for *Bi₂CoO₂F₄*; *a* = 5.434(5) Å, *b* = 16.350(1) Å, *c* = 5.4352(6) Å, *R*_{wp} = 6.55%, *R*_p = 4.69%, χ^2 = 3.13.

Atom	X	y	z	Occupancy	Beq (Å ²)	Site
Bi	0.0	0.3274(1)	0.0073(5)	1	0.42(3)	8f
Co	0.0	0.0	0.0	1	0.2(1)	4a
O(eq.)	0.298(2)	0.5314(4)	0.2977(2)	0.5	2.7(1)	16g
O(ap.)	0.0	0.1228(2)	0.9244(8)	1	1.36(9)	8f
O(fl.)	0.25	0.7469(3)	0.25	1	0.51(3)	8e

Table 3.6.4 – Selected bond lengths for *Bi₂CoO₂F₄* from NPD refinements in space group *Cmca* with a disordered *O*(eq) site.

Bond	Lengths in Å at 50 K	Bond	Lengths in Å at 50 K
Bi - O(fl.)	2 x 2.297(3)	Bi - O(eq.)	2 x 2.798(8)
Bi - O(fl.)	2 x 2.306(3)	Co - O(eq.)	4 x 2.02(1)
Bi - O(ap.)	1 x 2.408(5)	Co - O(eq.)	4 x 2.02(1)
Bi - O(ap.)	2 x 2.861(1)	Co - O(ap.)	2 x 2.050(3)

3.6.5.3 Refinement of *Pbca* model

The high atomic displacement parameter observed for the ordered *Cmca* model, which only allows rotation of *CoX₆* octahedra about an in-plane axis, could indicate additional rotation of *CoX₆* octahedra about an out-of-plane axis. If these rotations occurred over a long length scale in an ordered fashion, they would lower the symmetry of the structure to *Pbca* (see Figure 3.6.2), as suggested by mode inclusion analysis discussed above. 50 K NPD refinements were carried out in *Pbca* symmetry, which allows for rotation about both in-plane and out-of-plane axes (i.e., both *X₃⁺* and *X₂⁺* rotations). Refinement profiles, seen in Figure 3.6.9, showed a good match to the data, fitting peaks previously unfitted by the *I4/mmm* model. The refinement obtained a *R*_{wp} value of 6.51%, an improvement on the higher symmetry models, and the previously refined *Cmca* ordered model. It shows very similar fit to the data with the disordered *Cmca* model, which gave a *R*_{wp} of 6.54%.

The atomic positions, fractional occupancy and atomic displacement parameters of this refinement can be found in Table 3.6.5 with the selected bond lengths displayed in Table 3.6.6. On inspection of the atomic displacement parameters, there is a big improvement from the higher symmetry ordered *Cmca* model, however the *Pbca* model shows slightly worse *O*(eq) and *O*(ap) ADP than the disordered *Cmca* model.

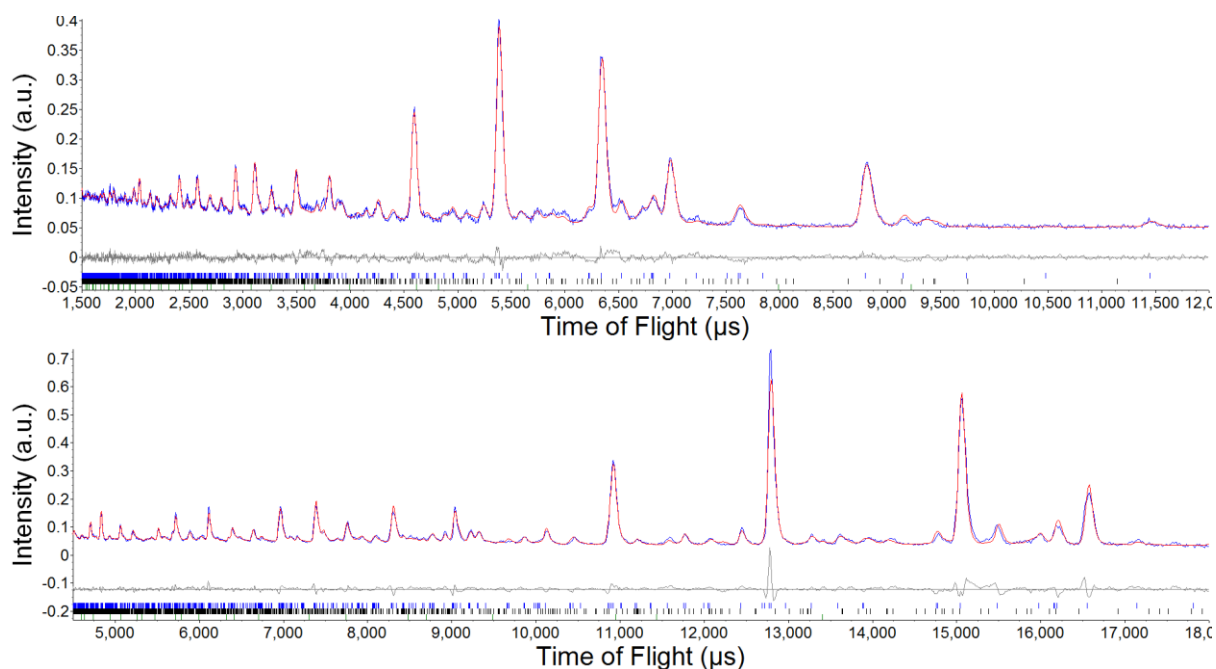


Figure 3.6.9 - Observed (-), calculated (-) and difference (-) profiles from Rietveld refinement using (top) bank 3 and (bottom) bank 5 of the 50 K NPD data of $\text{Bi}_2\text{CoO}_2\text{F}_4$. $Pbca$, $a = 16.350(1) \text{ \AA}$, $b = 5.4345(6) \text{ \AA}$, $c = 5.4342(6) \text{ \AA}$, $R_{wp} = 6.51\%$, $R_p = 4.73\%$, $\chi^2 = 3.07$. Reflection positions of main phase and $\text{Bi}_7\text{F}_{11}\text{O}_5$ are marked by lower black ticks and upper blue ticks, respectively.

Table 3.6.5 - Details from refinement in space group $Pbca$ using 50 K NPD data for $\text{Bi}_2\text{CoO}_2\text{F}_4$; $a = 16.350(1) \text{ \AA}$, $b = 5.4345(6) \text{ \AA}$, $c = 5.4342(6) \text{ \AA}$, $R_{wp} = 6.51\%$, $R_p = 4.73\%$, $\chi^2 = 3.07$.

Atom	X	y	z	Occupancy	Beq (\AA^2)	Site
Bi	0.3270(1)	0.9910(6)	0.999(1)	1	0.39(3)	8c
Co	0.0	0.0	0.0	1	0.09(9)	4a
O(eq.)	0.0293(4)	0.792(1)	0.299(1)	1	3.4(1)	8c
O(ap.)	0.1228(2)	0.0703(9)	0.996(2)	1	2.0(1)	8c
O(fl.)	0.2472(3)	0.741(1)	0.248(1)	1	0.51(4)	8c

Table 3.6.6 - Selected bond lengths for $\text{Bi}_2\text{CoO}_2\text{F}_4$ from NPD refinements in space group $Pbca$.

Bond	Lengths in \AA at 50 K	Bond	Lengths in \AA at 50 K
Bi - O(fl.)	1 x 2.27(1)	Bi - O(eq.)	1 x 2.845(8)
Bi - O(fl.)	1 x 2.27(1)	Bi - O(eq.)	1 x 2.87(1)
Bi - O(fl.)	1 x 2.319(9)	Co - O(eq.)	2 x 1.99(9)
Bi - O(fl.)	1 x 2.34(1)	Co - O(eq.)	2 x 2.036(9)
Bi - O(ap.)	1 x 2.428(6)	Co - O(ap.)	2 x 2.044(4)
Bi - O(ap.)	1 x 2.84(1)		

Significant tilting is found about the short, in-plane axis, and the long, out-of-plane axis. Tilting is out-of-phase and octahedra are slightly skewed in shape, with the *B*-site Co ions remaining in the centre of the CoX_6 octahedra, (Figure 3.6.10). The Co-O-Co angle of rotation about the long out of lane axis is 142.04° .

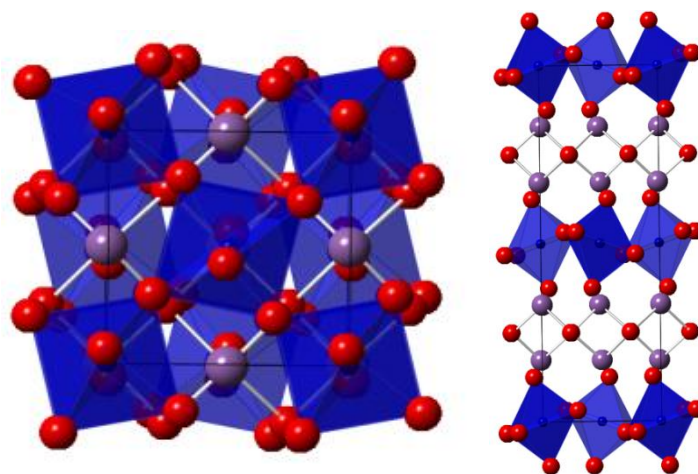


Figure 3.6.10 – Representation of *Pbca* structure for $\text{Bi}_2\text{CoO}_2\text{F}_4$, allowing in-phase rotations of octahedra about the short in-plane axis and out out-of-phase rotations about the long out-of-plane axis. Oxide/fluoride anions (red) take up positions in the apical/equatorial anion sites in the perovskite octahedra and the anions sites in the fluorite-like layer, bismuth (purple) lies in the fluorite layer and cobalt (blue) is positioned within the perovskite block.

3.6.5.4 SHG Measurements

Upon completion of the refinements previously, results of second harmonic generation (SHG) measurements returned, indicating that the $\text{Bi}_2\text{CoO}_2\text{F}_4$ is SHG active. This was exciting news, as it meant that the material lacked an inversion centre which is crucial for properties such as piezoelectricity and ferroelectricity. However, this means that the space group refinements listed above were not possible as both had inversion centres. This prompted us to look for space groups with an added polar mode, Γ_5^- .

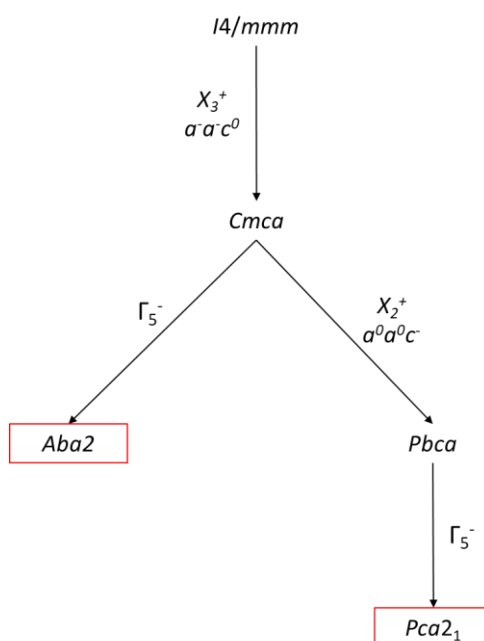


Figure 3.6.11 - Symmetry analysis using ISODISTORT showing types of distortions that $\text{Bi}_2\text{CoO}_2\text{F}_4$ can undergo with respect to the $I4/mmm$ space group. Irreducible representation is indicated by figures quoted on arms of symmetry map followed by respective Space group and glazer notation, showing extent of distortion.

Our mode inclusion analysis suggested that the X_{3^+} and the X_{2^+} modes gave the best fit for the NPD data, so we continued to follow this path. As indicated by *Figure 3.6.11*, the space groups represented by the red boxes; *Aba2*, derived from X_{3^+} and Γ_5^- modes, and *Pca2₁* that is made of a combination of X_{3^+} , X_{2^+} and Γ_5^- modes, forms the basis of our next two refinements.

3.6.5.5 Refinement of *Aba2* Model

Refinements of an *Aba2* model (allowing X_{3^+} rotations and polar displacements) gave a good fit to the data (*Figure 3.6.12*). The *Aba2* model is similar to the *Cmca* model but allows polar displacements. This *Aba2* model gave a slightly improved fit compared with the ordered *Cmca* model (*Figure 3.6.8*) with only 3 extra parameters (*Aba2*; 6.65% R_{wp} , 61 refined parameters, *Cmca*; 6.98% R_{wp} , 58 refined parameters). Details of the refinement are given in *Table 3.6.7*, showing a slightly high atomic displacement parameter on the equatorial anion site, and selected bond lengths are given in *Table 3.6.8*. However, on comparison with the disordered *Cmca* model, the fit was slightly worse despite an extra refinement parameter (disordered *Cmca*; 6.55% R_{wp} , 60 refined parameters).

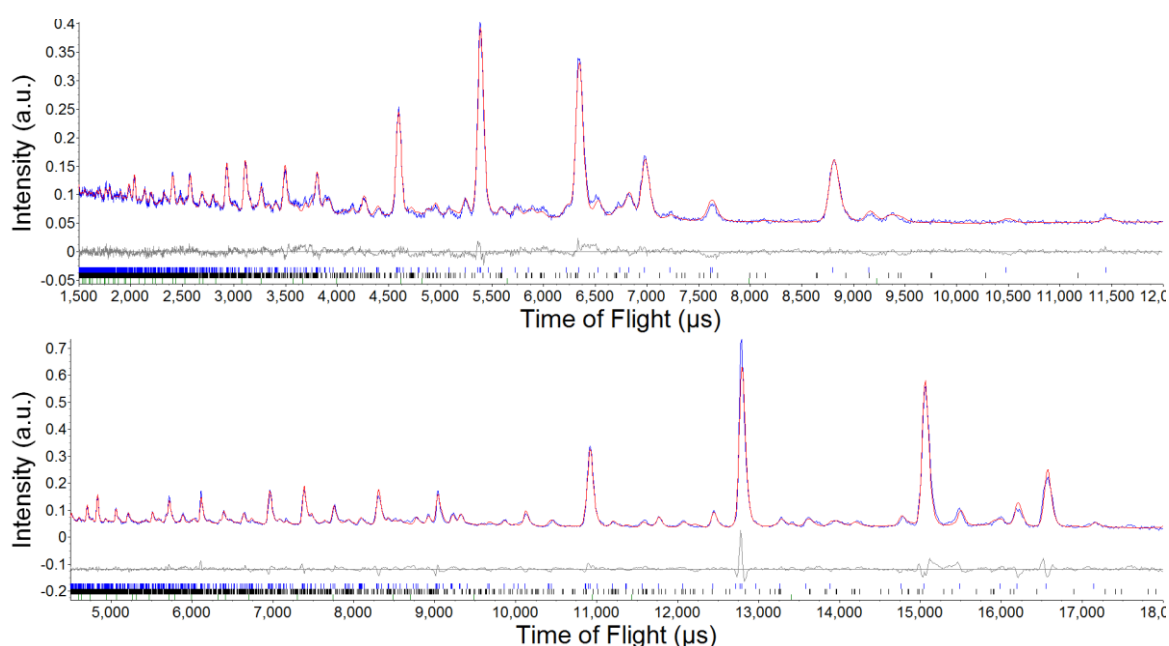


Figure 3.6.12 - Observed (-), calculated (-) and difference (-) profiles from Rietveld refinement using (top) bank 3 and (bottom) bank 5 of the 50 K NPD data of $\text{Bi}_2\text{CoO}_2\text{F}_4$. *Aba2*, $a = 5.4351(5) \text{ \AA}$, $b = 16.348(1) \text{ \AA}$, $c = 5.4342(5) \text{ \AA}$, $R_{wp} = 6.65\%$, $R_p = 4.80\%$, $\chi^2 = 3.21$. Reflection positions of main phase and $\text{Bi}_7\text{F}_{11}\text{O}_5$ are marked by lower black ticks and upper blue ticks, respectively.

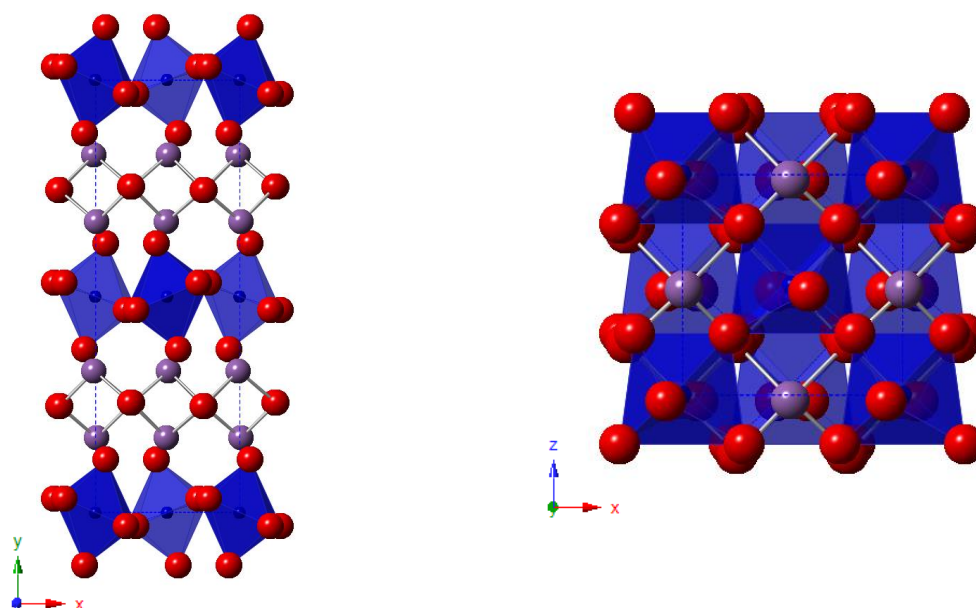


Figure 3.6.13 - Representation of *Aba2* space group of $\text{Bi}_2\text{CoO}_2\text{F}_4$, allowing rotations of octahedra about the short *c* plane and a slight displacement of cobalt cations. Oxide/fluoride anions (red) take up positions in the apical/equatorial anion sites in the perovskite octahedra and the anions sites in the fluorite-like layer, bismuth (purple) lies in the fluorite layer and cobalt (blue) is positioned within the perovskite block.

Cmca and *Aba2* models both share X_{3^+} rotational modes which can be seen in both the structural models, Figure 3.6.13 and Figure 3.6.7. *Aba2* also has a Γ_5^- mode which causes a polar displacement of the cobalt cations in the perovskite octahedra. Bond lengths, see Table 3.6.8, reveal that the Co^{2+} cations are displaced off centre by 0.021(9) Å along the in-plane *c* direction.

Table 3.6.7 - Details from refinement in space group *Aba2* using 50 K NPD data for $\text{Bi}_2\text{CoO}_2\text{F}_4$; $a = 5.4351(5)$ Å, $b = 16.348(1)$ Å, $c = 5.4342(5)$ Å, $R_{wp} = 6.65\%$, $R_p = 4.80\%$, $\chi^2 = 3.21$.

Atom	X	y	z	Occupancy	Beq (Å ²)	Site
Bi	0.990(5)	0.3276(1)	0.980(5)	1	1.19(4)	8b
Co	0.0	0.0	0.0	1	0.8(1)	4a
O(eq.)	0.715(2)	0.5307(4)	0.281(6)	1	5.1(1)	8b
O(ap.)	0.0753(8)	0.1225(2)	0.983(6)	1	2.09(9)	8b
O(fl.)	0.744(2)	0.7465(3)	0.235(6)	1	1.30(5)	8b

Table 3.6.8 – Selected bond lengths for $\text{Bi}_2\text{CoO}_2\text{F}_4$ from NPD refinements in space group Aba_2 .

Bond	Lengths in Å at 50 K	Bond	Lengths in Å at 50 K
Bi – O(fl.)	1 x 2.27(2)	Bi – O(ap.)	1 x 2.88(4)
Bi – O(fl.)	1 x 2.30(3)	Bi – O(eq.)	1 x 2.84(1)
Bi – O(fl.)	1 x 2.31(2)	Co – O(eq.)	2 x 1.99(2)
Bi – O(fl.)	1 x 2.34(3)	Co – O(eq.)	2 x 2.02(2)
Bi – O(ap.)	1 x 2.397(5)	Co – O(ap.)	2 x 2.046(4)
Bi – O(ap.)	1 x 2.84(4)		

3.6.5.6 Refinement of $\text{Pca}2_1$ model

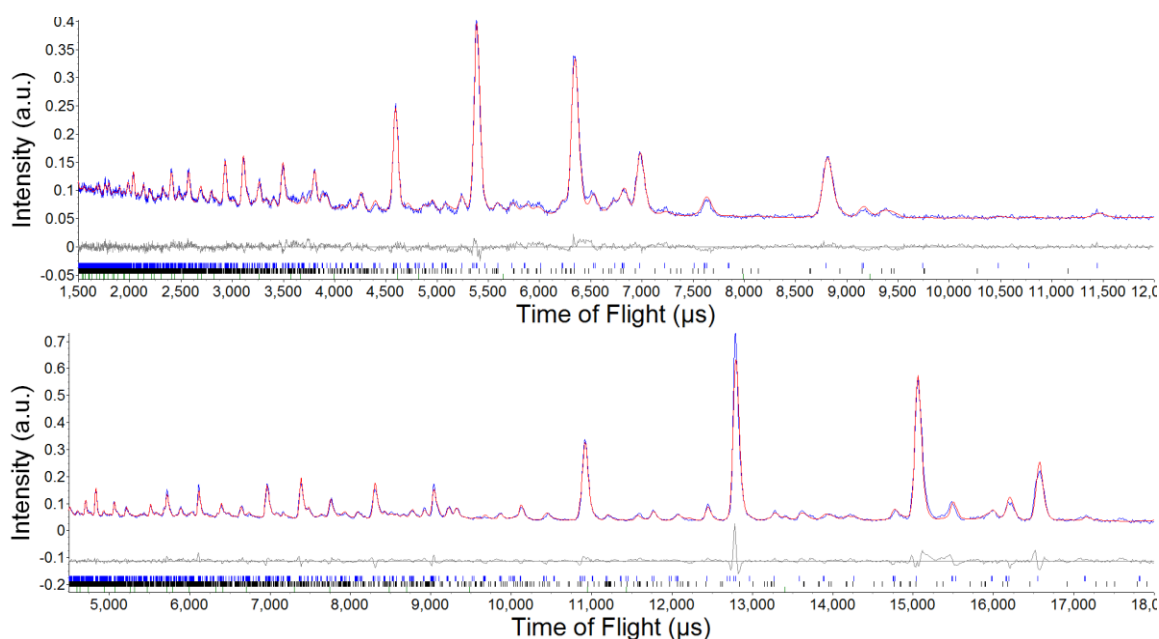


Figure 3.6.14 - Observed (-), calculated (-) and difference (-) profiles from Rietveld refinement using (top) bank 3 and (bottom) bank 5 of the 50 K NPD data of $\text{Bi}_2\text{CoO}_2\text{F}_4$. $\text{Pca}2_1$, $a = 5.434(6)$ Å, $b = 16.350(1)$ Å, $c = 5.4346(6)$ Å, $R_{\text{wp}} = 6.34\%$, $R_p = 4.66\%$, $\chi^2 = 2.92$. Reflection positions of main phase and $\text{Bi}_7\text{F}_{11}\text{O}_5$ are marked by lower black ticks and upper blue ticks, respectively.

Refinement profiles of $\text{Pca}2_1$ are given in Figure 3.6.14. There was a large improvement of fit in comparison to the Aba_2 model. However, there was a large increase in the number of refined parameters (Aba_2 ; 6.65% R_{wp} , 61 refined parameters, $\text{Pca}2_1$; 6.34% R_{wp} , 79 refined parameters). It was thought that the increase in the number of parameters for this refinement was justified for this refinement. Details of the refinement are given in Table 3.6.9 and selected bond lengths are given in Table 3.6.10. Fractional occupancies were fixed to 1 throughout the refinements.

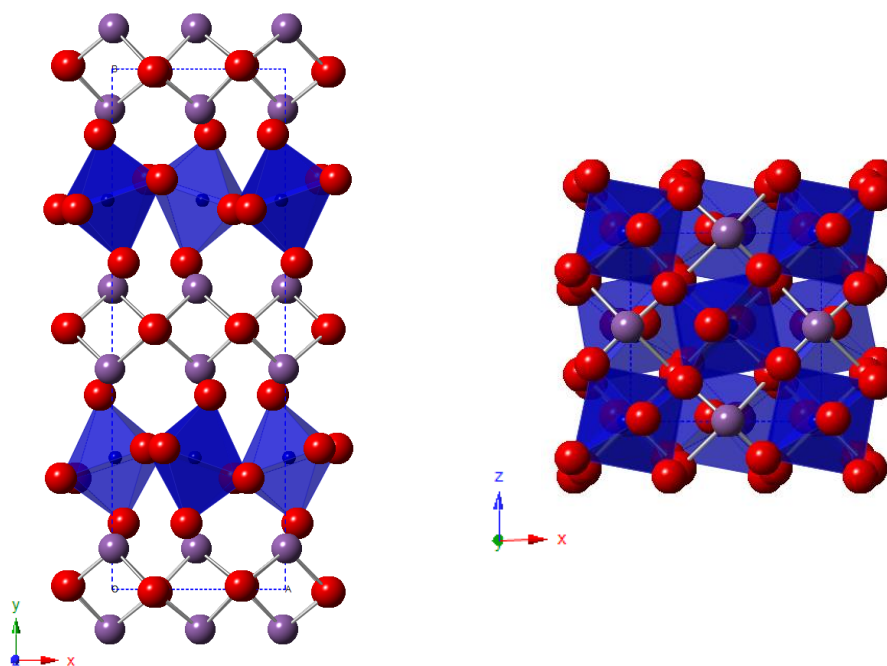


Figure 3.6.15 - Representation of $Pca2_1$ space group of $Bi_2CoO_2F_4$, allowing rotations of octahedra about the short in-plane axis, as well as about the long out-of-plane axis, and a slight displacement of Cobalt cations. Oxide/fluoride anions (red) take up positions in the apical/equatorial anion sites in the perovskite octahedra and the anions sites in the fluorite-like layer, bismuth (purple) lies in the fluorite layer and cobalt (blue) is positioned within the perovskite block.

The model, displayed by Figure 3.6.15, shows similar rotations of the octahedra about the in-plane axis as with the $Aba2$ and the $Cmca$ models and includes rotations about the out-of-plane axis given by addition of the X_2^+ mode. Polar displacements of the B -site cation are also shown in the $Pca2_1$ model. The Co-O-Co rotation angle is $139.48(6)^\circ$

Table 3.6.9 - Details from refinement in space group $Pca2_1$ using 50 KNPD data for $Bi_2CoO_2F_4$; $a = 5.434(6) \text{ \AA}$, $b = 16.350(1) \text{ \AA}$, $c = 5.4346(6) \text{ \AA}$, $R_{wp} = 6.34\%$, $R_p = 4.66\%$, $\chi^2 = 2.92$.

Atom	X	y	z	Occupancy	Beq (\AA^2)	Site
Bi (Bi_1)	0.011(2)	0.0775(7)	0.001(7)	1	1.5(2)	4a
Bi (Bi_2)	0.009(2)	0.5771(6)	0.502(7)	1	1.0(1)	4a
Co	0.978(5)	0.748(1)	0.0	1	0.6(2)	4a
O(eq.) (O1_1)	0.291(4)	0.7867(8)	0.205(8)	1	1.4(2)	4a
O(eq.) (O1_2)	0.199(4)	0.2705(9)	0.803(8)	1	1.9(3)	4a
O(ap.) (O2_1)	0.930(4)	0.874(1)	0.023(7)	1	1.8(3)	4a
O(ap.) (O2_2)	0.932(4)	0.373(1)	0.514(8)	1	1.6(4)	4a
O(fl.) (O3_1)	0.243(3)	0.0060(6)	0.250(8)	1	1.3(2)	4a
O(fl.) (O3_2)	0.256(4)	0.4997(7)	0.7435(8)	1	1.1(2)	4a

Table 3.6.10 - Selected bond lengths for $\text{Bi}_2\text{CoO}_2\text{F}_4$ from NPD refinements using $Pca2_1$ model.

Bond	Lengths in Å at 50 K	Bond	Lengths in Å at 50 K
Bi(1) - O(fl.)	1 x 2.27(4)	Bi(2) - O(fl.)	1 x 2.37(4)
Bi(1) - O(fl.)	1 x 2.30(4)	Bi(2) - O(ap.)	1 x 2.44(3)
Bi(1) - O(fl.)	1 x 2.31(4)	Bi(2) - O(ap.)	1 x 2.80(6)
Bi(1) - O(fl.)	1 x 2.35(4)	Bi(2) - O(ap.)	1 x 2.91(6)
Bi(1) - O(ap.)	1 x 2.41(3)	Bi(2) - O(eq.)	1 x 2.94(3)
Bi(1) - O(ap.)	1 x 2.73(5)	Co - O(eq.)	1 x 1.88(4)
Bi(1) - O(ap.)	1 x 2.96(5)	Co - O(eq.)	1 x 1.93(4)
Bi(1) - O(eq.)	1 x 2.75(3)	Co - O(eq.)	1 x 2.04(4)
Bi(1) - O(eq.)	1 x 3.19(3)	Co - O(eq.)	1 x 2.09(3)
Bi(2) - O(fl.)	1 x 2.26(4)	Co - O(ap.)	2 x 2.13(4)
Bi(2) - O(fl.)	2 x 2.28(4)		

Analysis of the 50 K NPD data do not allow a definitive decision between the $Aba2$ and the $Pca2_1$ models.

3.7 Investigation of Anion Distribution through Bond Valence Sum Calculations

The Co-O bond lengths are similar to those reported in the literature.⁶³ Bond valence sum (BVS) analysis was carried out.^{56,64} We note that these calculations using empirical values from room temperature structures should be carried out using bond lengths from refinements using data collected at room temperature. Our calculations here use 50 K data and should therefore not be interpreted quantitatively but might be useful to make comparisons between models. *Table 3.7.1* shows the calculated valence for each anion site in the material, using bond distances presented in *Tables 3.6.8 & 3.6.10*. Due to the low valence calculated for the apical and equatorial sites and the fluorite anion site having a calculated valence of around 2, the BVS results suggests that O(ap.) and O(eq.) are primarily occupied by fluoride anions whereas the O(fl.) sites are occupied by oxide anions. This is consistent with other $n = 1$ Aurivillius oxyfluoride materials, such as, Bi_2NbOF_5 .⁶⁵

Table 3.7.1 - Bond valence sum (BVS) analysis for the anion sites using bond lengths from Rietveld refinements of space groups *Aba2* and *Pca2₁*.

Ion	<i>Aba2</i> Valence		<i>Pca2₁</i> Valence	
	Oxygen calculated valence parameter	Fluorine calculated valence parameter	Oxygen calculated valence parameter	Fluorine calculated valence parameter
O(ap.)	1.00	0.85.	1.00 (O2_1 site)	0.80 (O2_1 site)
			1.05 (O2_2 site)	0.84 (O2_2 site)
O(eq.)	1.04	0.84	1.02 (O1_1 site)	0.87 (O1_1 site)
			0.99 (O1_2 site)	0.84 (O1_2 site)
O(fl.)	2.26	1.72	2.19 (O3_1 site)	1.67 (O3_1 site)
			2.33 (O3_2 site)	1.77 (O3_2 site)

Table 3.7.2 shows the BVS calculations of bismuth and cobalt using the cation–anion bond lengths from Tables 3.5.8 & 3.5.10. The results from Table 3.7.1 allowed for the estimation that O(ap.) and O(eq.) anion sites were occupied by fluorine and O(fl.) was occupied by oxygen, so respective valence parameters were used for each respective bond in these calculations. The results from the Bi and Co BVS calculations for the both the *Aba2* and *Pca2₁* models suggest that Bi has a valence of close to 3 and the valence for Co is very close to 2. This is consistent with the expected oxidation states.⁴⁷

Table 3.7.2 – Bond valence sum (BVS) analysis for the respective bismuth and cobalt cations associated with the bond lengths gathered from Rietveld refinements of space groups *Aba2* and *Pca2₁*.

Ion	<i>Aba2</i>	<i>Pca2₁</i>
Bi	2.88	2.82 (Bi_1), 2.83 (Bi_2)
Co	2.15	2.09

3.8 Magnetic Structural Characterisation Using 5 K Neutron Powder Diffraction Data

Neutron powder diffraction data were also collected at 5 K. Although we could not distinguish unambiguously between *Aba2* and *Pca2₁* models at 50 K, Raman scattering⁴⁷ indicates some ordering on cooling and so it is likely that the X_2^+ mode (allowed for the *Pca2₁* model) will be frozen in by 5 K and so we assume a nuclear model of *Pca2₁* symmetry. Magnetic measurements indicate long-range magnetic order below the Néel temperature, T_N , at ~50 K and so the low temperature NPD data will allow us to determine the nature of the magnetic ordering. Some additional magnetic Bragg peaks, with hkl values: (030) and (120), were observed in bank 3 of the data collected at 5 K (shown by arrows in Figure 3.8.1) that could be indexed by the same $\sqrt{2}a \times \sqrt{2}a' \times c$ unit cell as the *Pca2₁* nuclear structure.

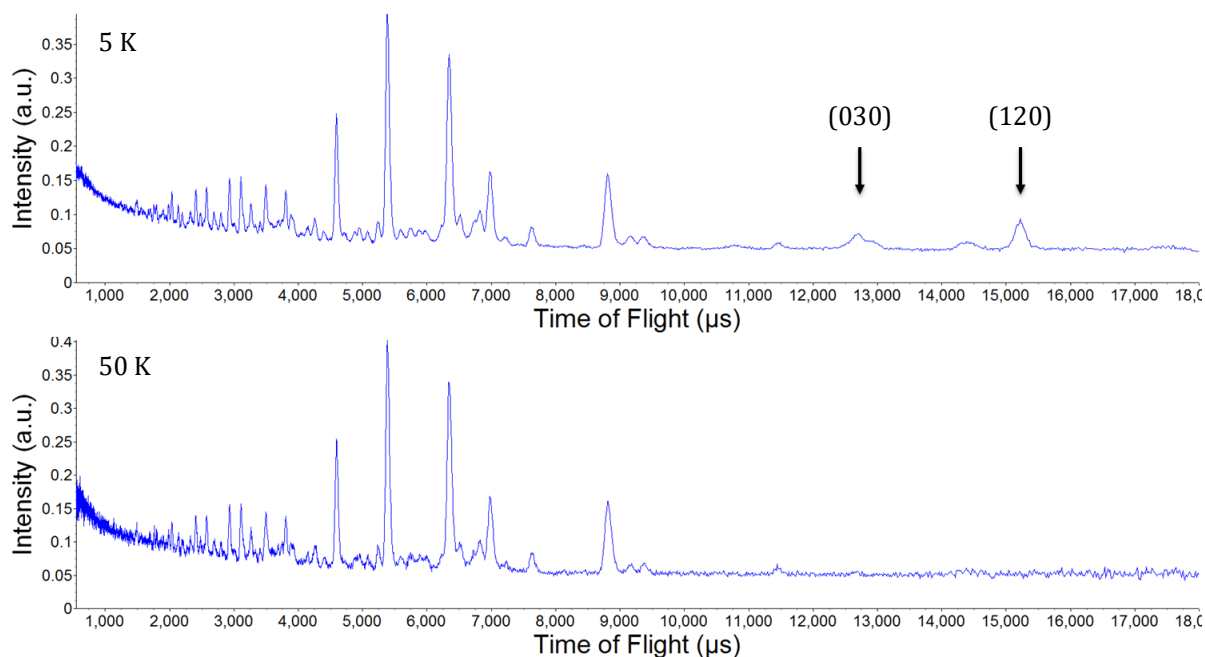


Figure 3.8.1 – Observed data plots of $\text{Bi}_2\text{CoO}_2\text{F}_4$ bank 3 neutron powder diffraction data taken at (top) 5 K and (bottom) 50 K, with arrows indicating extra peaks at hkl values: (030) and (120).

3.8.1 Simulated Annealing of Magnetic Modes

The mode inclusion method⁶² was used to consider different magnetic structures. The nuclear phase was fixed and a second, magnetic-only phase, was included. The long d-spacing range of the bank 3 data was used for mode inclusion analysis. The R_{wp} values for each magnetic mode or set of modes is displayed by Figure 3.8.2 and the relevant magnetic modes are shown in Figure 3.8.3.

The first round of refinements suggested that the $m\Gamma_2^+ A 1$ and $m\Gamma_1^+ A 3$ gave the best fit to the data (R_{wp} values of 5.21 % and 5.23 %, respectively), Figure 3.8.2. Both irreps describe collinear antiferromagnetic structures with moments along the in-plane axes; $m\Gamma_1^+$ has AFM moments in both axes whilst $m\Gamma_2^+$ shows an AFM and a ferromagnetic component along the in-plane axes, Figure 3.8.3. It is difficult to distinguish between these two models due to the very small orthorhombic distortion.

Literature suggests the material predominantly has antiferromagnetic long-range ordering, however, anomalies in the magnetic susceptibility measurements did occur below ~ 40 K at low magnetic fields which suggested development of ferromagnetic spontaneous magnetisation.⁴⁷ Potentially there could be a ferromagnetic phase with similar energy to the antiferromagnetic phase which could explain this anomaly. Although $m\Gamma_1^+$ order is purely AFM, the $m\Gamma_2^+$ irrep also allows a ferromagnetic out-of-plane component.

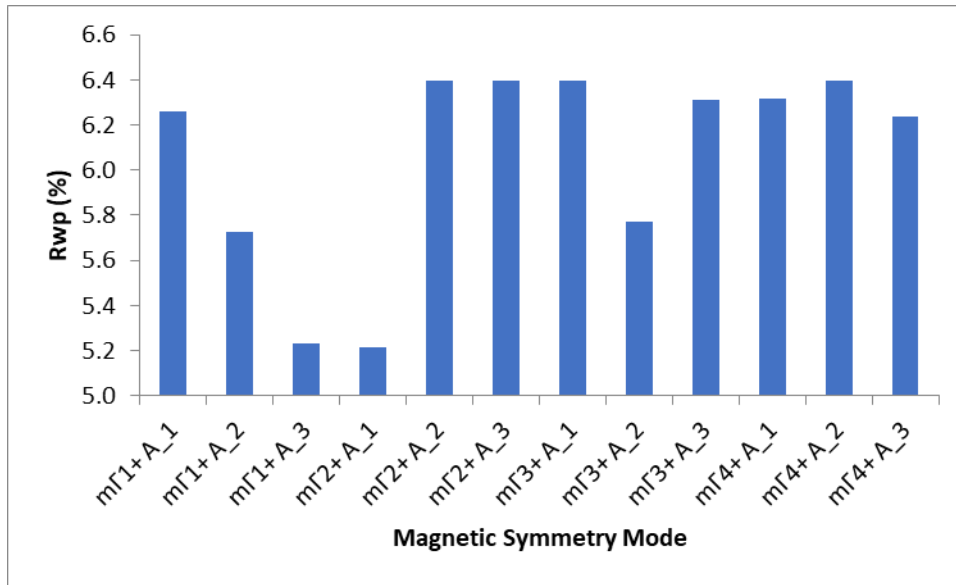


Figure 3.8.2 - Graph depicting the change in R_{wp} for the refinement of relevant magnetic modes to 5 K $\text{Bi}_2\text{CoO}_2\text{F}_4$ neutron powder diffraction data. These refinement details are from the first round of the mode inclusion simulated annealing.

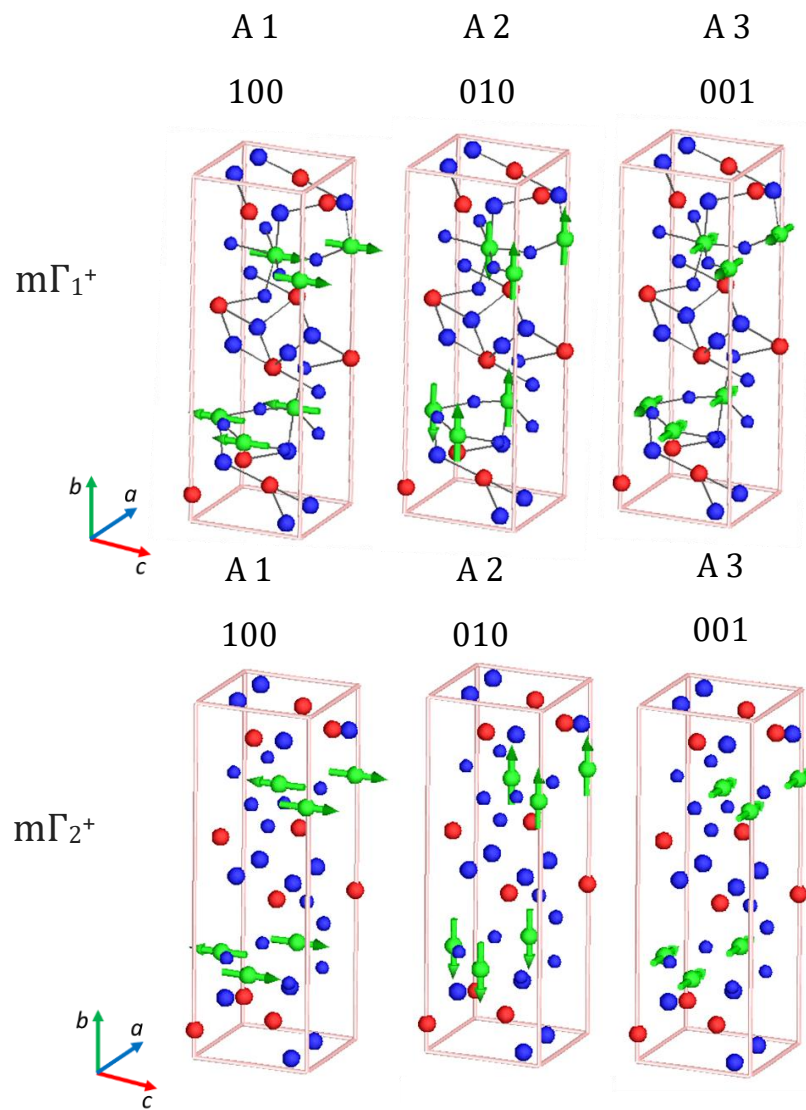


Figure 3.8.3 – depiction of the magnetic order type and direction of selected magnetic modes acting on the material, with cobalt (green), bismuth (red) and oxygen (blue).

3.8.2 Refinement of Magnetic Structure

3.8.2.1 Refinement of $m\Gamma_1^+$ model

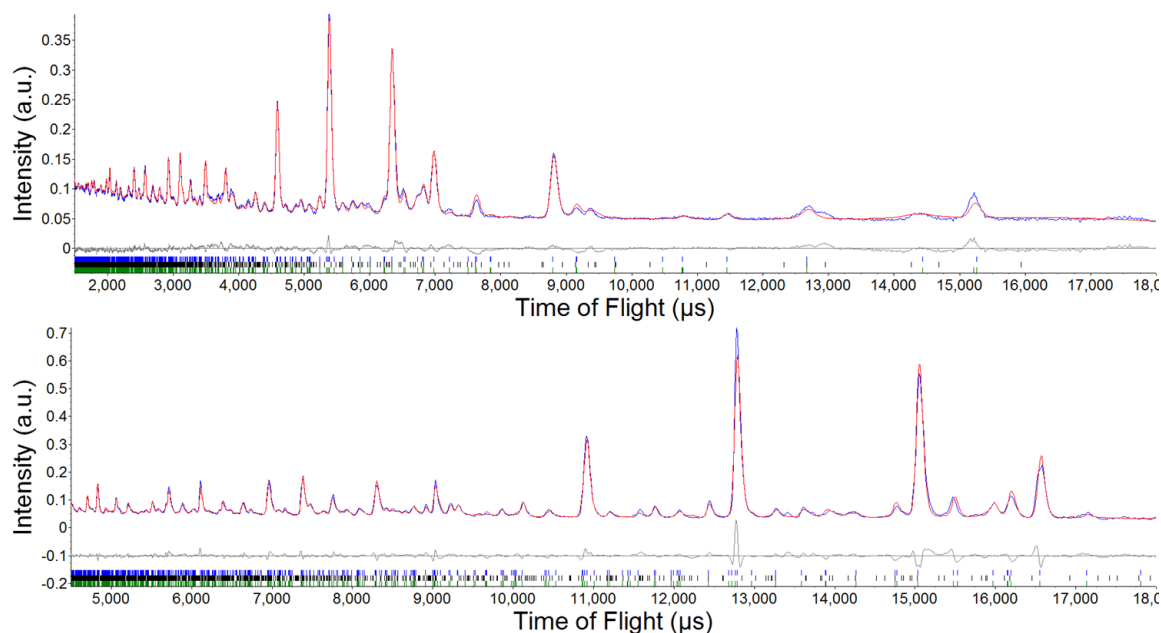


Figure 3.8.4 - Observed (-), calculated (-) and difference (-) profiles from Rietveld refinement using (top) bank 3 and (bottom) bank 5 of the 5 K NPD data of $\text{Bi}_2\text{CoO}_2\text{F}_4$. $Pca2_1$, $a = 5.4317(5) \text{ \AA}$, $b = 16.3472(1) \text{ \AA}$, $c = 5.4317(5) \text{ \AA}$, $R_{\text{wp}} = 5.22\%$, $R_p = 4.08\%$, $\chi^2 = 8.59$. Reflection positions of magnetic phase, main phase and $\text{Bi}_7\text{F}_{11}\text{O}_5$ are marked by lower green ticks, upper blue ticks, and middle black ticks, respectively.

For refinement of the $m\Gamma_1^+$ model, bank 5 and bank 3 data were included in the refinement allowing both nuclear and magnetic structures to be refined, see Figure 3.8.4. Although a good fit was obtained refining only the $m\Gamma_1^+$ _A3 mode (Co^{2+} moments along a direction, $R_{\text{wp}} = 5.65\%$), the $m\Gamma_1^+$ irrep also allows another AFM-in-plane component as well as an AFM out-of-plane component. Including the second in-plane component did not improve the fit and this parameter was strongly correlated with the $m\Gamma_1^+$ _A3 mode. Including the AFM out-of-plane component did give a slight improvement in fit ($R_{\text{wp}} = 5.63\%$) and allowed a small out-of-plane component (total Co^{2+} moment = $2.4(1) \mu_{\text{B}}$ of which $2.3(1) \mu_{\text{B}}$ in-plane and $0.7(2) \mu_{\text{B}}$ out-of-plane). The $m\Gamma_1^+$ magnetic model is shown in Figure 3.8.5. The calculated magnetic moment is a little smaller than that reported in the literature for La_2CoO_4 , with an effective magnetic moment of $\sim 2.6 \mu_{\text{eff}}$.⁶⁶

Table 3.8.1 – Details from rietveld refinement using 5 K data for $\text{Bi}_2\text{CoO}_2\text{F}_4$, with $\text{Pca}2_1$ nuclear model and magnetic-only $m\Gamma_1^+$ magnetic structure; $a = 5.4317(5) \text{ \AA}$, $b = 16.3472(1) \text{ \AA}$, $c = 5.4317(5) \text{ \AA}$, Co^{2+} moment = $2.4(1) \mu_B$ ($2.3(1) \mu_B$ along a , $0.7(2) \mu_B$ along b), $R_{\text{wp}} = 5.22\%$, $R_p = 4.08\%$, $\chi^2 = 8.59$.

Atom	X	y	z	Occupancy	Beq (\AA^2)	Site
Bi	0.012(1)	0.0778(4)	0.007(2)	1	0.48(8)	4a
Bi	0.008(1)	0.5768(4)	0.510(2)	1	0.09(6)	4a
Co	0.974(1)	0.7471(5)	0	1	0.71(2)	4a
F(eq.)	0.291(2)	0.7845(7)	0.208(3)	1	0.2(1)	4a
F(eq.)	0.199(3)	0.2710(8)	0.807(4)	1	1.4(2)	4a
F(ap.)	0.933(3)	0.874(1)	0.029(3)	1	1.1(2)	4a
F(ap.)	0.930(3)	0.373(1)	0.523(3)	1	0.6(2)	4a
O(fl.)	0.241(2)	0.9942(5)	0.256(3)	1	0.5(1)	4a
O(fl.)	0.253(2)	0.4987(5)	0.746(3)	1	0.011(6)	4a

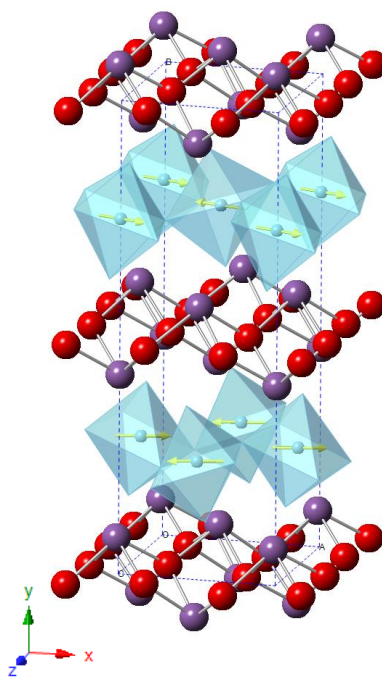


Figure 3.8.5 - Magnetic moments (yellow arrows) of each cobalt ion in the $\text{Bi}_2\text{CoO}_2\text{F}_4$ Aurivillius material using a $\text{Pca}2_1$ model with $m\Gamma_1^+$ magnetic model.

3.8.2.2 Refinement of $m\Gamma_2^+$ model

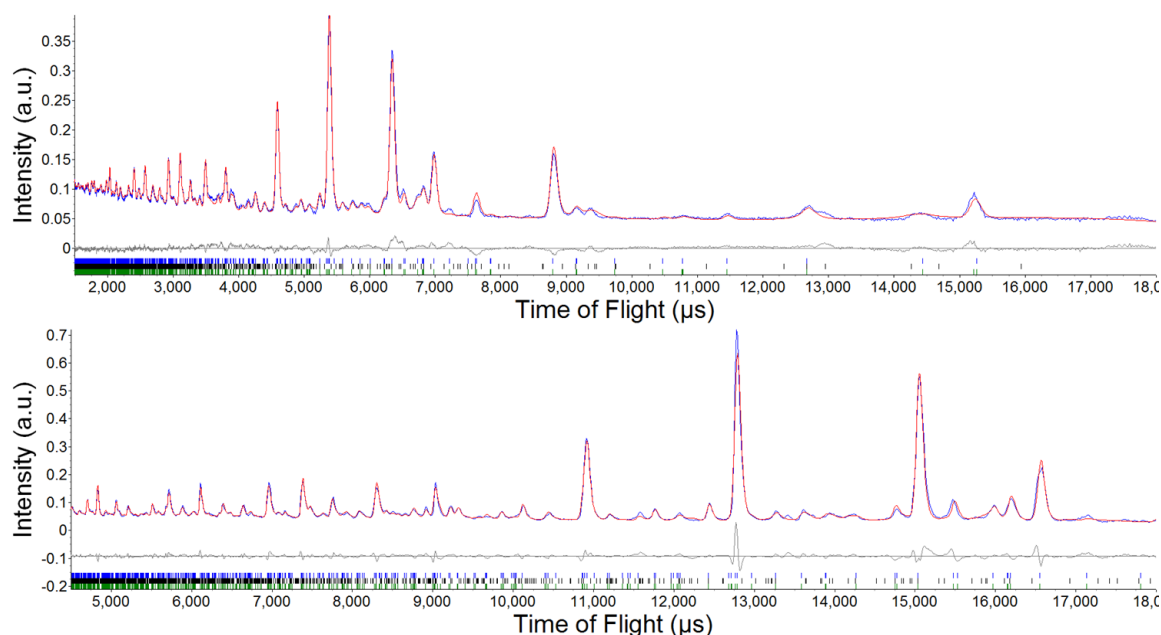


Figure 3.8.6 - Observed (-), calculated (-) and difference (-) profiles from Rietveld refinement of (top) bank 3 and (bottom) bank 5 of the 5 K NPD data of $\text{Bi}_2\text{CoO}_2\text{F}_4$. $\text{Pca}2_1$, $a = 5.4317(5) \text{ \AA}$, $b = 16.3472(1) \text{ \AA}$, $c = 5.431(5) \text{ \AA}$, $R_{\text{wp}} = 5.20\%$, $R_p = 4.04\%$, $\chi^2 = 8.55$. Reflection positions of magnetic phase, main phase and $\text{Bi}_7\text{F}_{11}\text{O}_5$ are marked by lower green ticks, upper blue ticks, and middle black ticks, respectively.

This refinement was carried out analogously to the $m\Gamma_1^+$ magnetic refinement, see *Figure 3.8.6*. Although the collinear AFM structure described by $m\Gamma_2^+$ _A1 gave a good fit to the data ($R_{\text{wp}} = 5.65\%$), the $m\Gamma_2^+$ irrep also allows a second AFM in-plane component, as well as a ferromagnetic in-plane component. Including the $m\Gamma_2^+$ _A2 out-of-plane mode did not improve the fit and had high errors. The $m\Gamma_2^+$ _A3 ferromagnetic in-plane component gave a slight improvement in fit ($R_{\text{wp}} = 5.62$) and allowed a small in-plane component along the a direction (total Co^{2+} moment = $2.6(1) \mu_{\text{B}}$ of which $2.42(7) \mu_{\text{B}}$ $m\Gamma_2^+$ _A1 and $0.9(2) \mu_{\text{B}}$ $m\Gamma_2^+$ _A3). The $m\Gamma_2^+$ magnetic model is shown in *Figure 3.8.7*, which shows antiferromagnetic ordering along the b direction, as well as a ferromagnetic component along the a direction, this model is thought to have a similar energy to the purely AFM $m\Gamma_1^+$ magnetic model. The calculated magnetic moment is very similar to the reported literature on the layered perovskite La_2CoO_4 , with an effective magnetic moment of $\sim 2.6 \mu_{\text{eff}}$.⁶⁶

Table 3.8.2 – Details from rietveld refinement using 5 K data for $\text{Bi}_2\text{CoO}_2\text{F}_4$, with $\text{Pca}2_1$ nuclear model and magnetic-only $m\Gamma_{2^+}$ magnetic structure; $a = 5.4317(5) \text{ \AA}$, $b = 16.3472(1) \text{ \AA}$, $c = 5.4318(5) \text{ \AA}$, Co^{2+} moment = $2.6(1) \mu_B$ ($2.42(7) \mu_B$ along c , $0.9(2) \mu_B$ along b) $R_{\text{wp}} = 5.20\%$, $R_p = 4.04\%$, $\chi^2 = 8.55$.

Atom	X	y	z	Occupancy	Beq (\AA^2)	Site
Bi	0.012(1)	0.0779(4)	0.0050(3)	1	0.55(8)	4a
Bi	0.007(1)	0.5768(4)	0.508(3)	1	0.04(5)	4a
Co	0.975(1)	0.7476(6)	0	1	0.61(4)	4a
F(eq.)	0.291(2)	0.7846(7)	0.206(4)	1	0.3(1)	4a
F(eq.)	0.198(3)	0.2716(8)	0.805(4)	1	1.3(2)	4a
F(ap.)	0.933(3)	0.874(1)	0.026(3)	1	1.1(2)	4a
F(ap.)	0.929(3)	0.3731(1)	0.519(4)	1	0.7(2)	4a
O(fl.)	0.241(2)	0.9941(5)	0.253(3)	1	0.5(1)	4a
O(fl.)	0.254(2)	0.4987(5)	0.743(3)	1	0.02(7)	4a

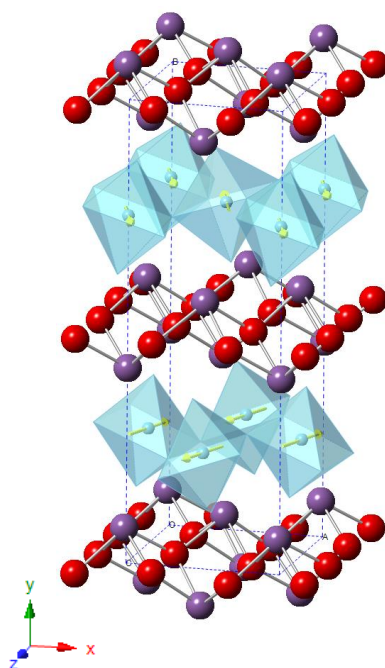


Figure 3.8.7 - Magnetic moments (yellow arrows) of each cobalt ion in the $\text{Bi}_2\text{CoO}_2\text{F}_4$ Aurivillius material using a $\text{Pca}2_1$ model with $m\Gamma_{2^+}$ magnetic modes.

3.9 Discussion

We have established that the ground state crystal structure of $\text{Bi}_2\text{CoO}_2\text{F}_4$ adopts octahedral tilts of CoF_6 about both the in-plane and out of plane axes, which is consistent with other $n = 1$ Aurivillius phases such as Bi_2WO_6 ,^{34,35} whereas the La_2CoO_4 RP phase only tilts about an in-plane axis.⁶⁷ Second harmonic generation activity was recorded indicating a non-centrosymmetric structure, and so polar displacements were considered, similar to Bi_2WO_6 , and unlike $\text{Bi}_2\text{NbO}_5\text{F}$.³³ This may indicate that anion order may be needed for polar symmetries.

BVS sum analysis gave further evidence to support that F^- preferentially takes up the octahedral anion sites, whilst oxygen takes up the sites in the fluorite layer. This could be due to the smaller fluoride anions preferring wider perovskite layers to reduce stacking strain. High atomic displacement parameters on the F3 site may indicate anion vacancies or problems with the position of the site in the model.

We have considered two possible magnetic structures for $\text{Bi}_2\text{CoO}_2\text{F}_4$. We are unable to definitively distinguish between these two magnetic models and density functional theory calculations may give further insight. The magnetic structure can be described by the same size unit cell as the nuclear structure, magnetic moments ordering approximately collinear with antiferromagnetic interactions. In-plane directed moments are dominant, as seen in La_2CoO_4 .⁶⁸ The $m\Gamma_2^+$ gives the interesting prospect that ferromagnetism could arise from $m\Gamma_2^+$ A 3 mode ordering on increasing temperature towards the Néel temperature, which would explain anomalies in magnetic susceptibility measurements.⁴⁷

Chapter 4

Anion Order to Break Inversion Symmetry

4.1 Introduction

4.1.1 How to Get Anion-Order

4.1.1.1 What is Anion Ordering

The main approaches to designing new transition metal compounds include tuning crystal chemistry via chemical substitution^{44,69} or applying external stimuli (e.g. pressure⁷⁰). A relatively recent advancement has been the use of anion substitution/ordering to tune properties. It has been found that the ordering of the anions, and the extent of this, gives new structures and physical properties.⁷¹

Heteroanionic crystals are solid materials where anion sites are occupied by two or more different anions. These anions, depending on several differing characteristics (e.g., atomic size, charge, electronegativity, etc) will be distributed among available anion sites. This distribution can be described as: disordered, where anions are distributed randomly over anion sites; ordered (with long-range ordering), where anions occupy distinct structural sites over a similar correlation length as the cation sublattice; or partially ordered, where incomplete or short-range ordering of anions may be observed (e.g., if several possible anion arrangements are of similar energy).⁷²

The differences in chemistry between the two anions will affect the extent of ordering. Long range order in heteroanionic materials is favoured where there is a large difference in ionic radius between the two anions, as seen in oxysulfides.⁷³ In general, when first row anions (most likely oxide) are mixed with second row anions, long-range ordering is expected as a result of their different size. This is seen in the oxychalcogenides, $\text{Sr}_2\text{MO}_2\text{Cu}_{2-\delta}\text{S}_2$ ($M = \text{Mn, Co, Ni}$),⁷⁴ with ordering dependent on the polarizability and the difference in chemistries of the anions. The study also suggests that layered perovskite-related structures offer a convenient way to develop ordering in heteroanionic materials because of the natural 2-dimensional layering offering better stability.

In heteroanionic materials with similarly sized anions, long range ordering is less common and short-range ordering is more likely.⁷⁵ This is seen in the oxynitride perovskites, SrMO_2N ($M = \text{Nb, Ta}$),⁷⁶ where partial anion order is formed with the preference for *cis*-ordering but often no long-range crystallographic ordering occurs. This *cis* preference may come about by a balancing of elastic energies, which is caused by strain from the metal-anion bond sizes and the electronic interactions with surrounding ions. If the elastic energies are sufficiently similar between different sites, then mixed anion occupancy would be expected.⁷¹

Possible ordered arrangements for similar-sized anions are often close in energy and so the anion arrangements may be controlled by synthesis route. Chemical properties can be altered by the extent of ordering and so different synthetic routes may be used to tune the degree of order and properties.⁷⁷ An example of this is the anion order-disorder transition in $\text{Sr}_2\text{FeO}_3\text{F}$ affected by temperature and pressure.⁷⁸ The oxynitride, SrTaO_2N , exhibits a preferred local *cis* ordering of octahedra, however, this can be transformed to *trans*- $[\text{TaO}_4\text{N}_2]$ configurations by growing compressed thin films.⁷⁹

Another factor that influences anion ordering is the difference in charge of the anions. A good example is the fluorination of Ce_2MnN_3 to $\text{Ce}_2\text{MnN}_3\text{F}_{2-\delta}$,⁸⁰ where the addition of fluoride anions expands the manganese coordination, driving structural change as the manganese coordination changes from almost square planar MnN_4 to layers of distorted octahedral MnN_5F . The N^{3-} anions take up the equatorial sites and one apical site and one F^- anion takes up the remaining apical site in an ordered fashion, and the other fluoride occupies an interstitial site between the apical fluoride anion site. The N^{3-} ions form strong Mn-N-Mn bonds in the equatorial positions and fluorine relaxes elastic energies by distorting the octahedra as well as coordinating to new cerium sites around the interstitial fluoride sites. The strong nitrogen bonds cause F^- insertion rather than F^-/N^{3-} substitution, which is usually found in fluorination with less diverse anion charges, such as in fluorination of A_2CuO_3 ($A = \text{Ca, Sr}$).⁸¹

Useful synthetic approaches to increase the likelihood of heteroanionic materials giving anion order are the chimie douce methods, where a thermodynamically stable phase is altered by soft-chemistry routes. These topochemically controlled synthesis routes occur at relatively low temperatures and give minimal structural change to the parent material.⁸² Low temperature fluorination reactions can be oxidative (e.g. inserting fluoride ions into interstitial sites), or substitutional (e.g. replacing an O^{2-} anion by two F^- anions) and are likely to favour F^- anions occupying specific anion sites in the lattice.¹⁵ Examples of anion-ordered oxyfluorides from topochemical routes include the fluorination of La_2NiO_{4+d} to $La_2NiO_3F_2$,⁸³ which produces an anion-ordered half occupancy of interstitial sites with F^- , prompting octahedral distortions; and the oxidative insertion reaction to convert $La_2SrCr_2O_7$ to $La_2SrCr_2O_7F_2$.¹⁷

Anion ordering will give different structures which influence properties, e.g., layered structures in the oxychalcogenides, and symmetry lowering in many oxyfluorides and oxynitrides. Theory work⁷¹ suggests that this symmetry lowering could be used to tune the properties of materials (e.g. to break inversion symmetry).

4.1.1.2 Anion Ordering in Oxyfluorides and other Layered Perovskites-Related Materials

This section considers layered perovskite-related heteroanionic materials and how the changes in topology can affect, properties with a focus on the oxyfluorides which are relevant to this study.

In perovskite-related materials the anions can take up either apical or equatorial positions of the BX_6 octahedra, see *Figure 4.1.1 (a)*, and the layered nature of Aurivillius and Ruddlesden-Popper phases can also influence anion arrangements. Octahedral units can exhibit half occupancy among the anion sites, which can be described as *cis* or *trans* in $[BX_2X'_4]$ octahedral units, or *fac* and *mer* in $[BX_3X'_3]$ octahedra, as illustrated in *Figure 4.1.1 (b)*. These units can be arranged in an ordered fashion in the long-range or in the short range or vary randomly from one unit-cell to the next in disordered structures.

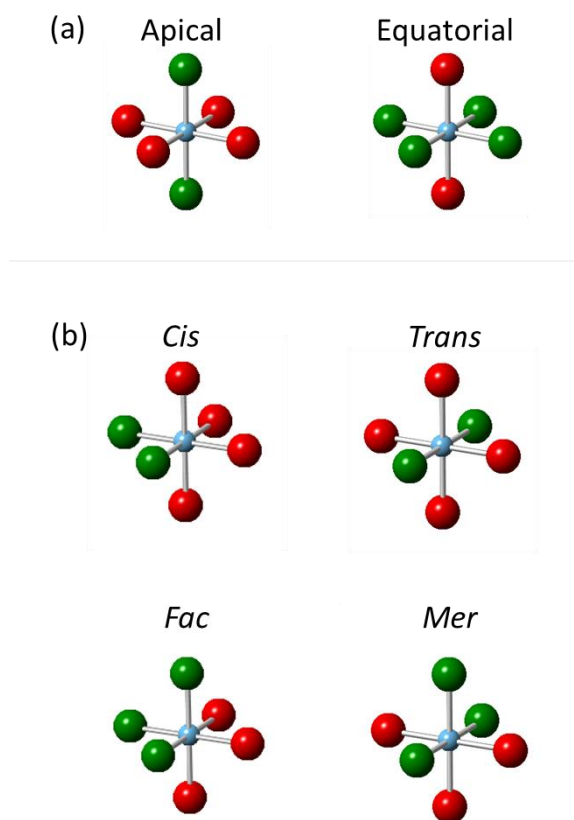


Figure 4.1.1 - Illustrations of (a) anion sites, and (b) cis, trans, mer and fac isomers for heteroanionic BX_6 units, where B (blue) represents metal cations and X (red) represents oxide anions and X' (green) represents the non-oxide anion.

In general, in heteroanionic materials with similarly sized anions, such as the oxyfluorides or oxynitrides, anion ordering is often only short-range, as seen in the Aurivillius oxyfluorides, $Bi_2TiO_4F_2$ ³² and Bi_2NbO_5F ,³³ as well as other perovskite-related oxyfluorides, such as the $K_2MoO_3F_3$ ⁸⁴ double perovskite phase.

The two-dimensional stacking in layered perovskite-like heteroanionic materials adds natural anisotropy, due to the lack of the third-dimension connectivity found in perovskites.^{71,77} In $n = 1$ layered perovskite-like compounds, such as, Sr_2BO_3F ($B = Sc, Mn, Fe, Co, Ni$)⁸⁵ Ruddlesden-Popper phases F^- occupies the apical sites. However, short-range ordering is preferred, only Sr_2FeO_3F exhibits long-range ordering, forming an antipolar structure. In the $n = 2$ Ruddlesden-Popper oxyfluoride, $Ba_3In_2O_5F_2$, the double perovskite layers are replaced by an indium-oxygen square pyramidal structure separated by BaF rocksalt layers, with fluorine situated at the terminal apical anion sites. It is not only the oxyfluorides that exhibit this behaviour, it can also be found in some oxychalcogenides such as $Ln_2Ti_2S_2O_5$,⁸⁶ where the anions' size difference is considerably larger and the larger volume of space at the terminal apical sites offer more stability to the larger anions.

However, in contrast to the these phase described above, there are also examples of F^- occupying equatorial sites, such as the $n = 2$ Dion-Jacobson materials, $ASrNb_2O_6F$ (where $A = Li, Na, Rb$)⁸⁷ and $RbLnTiNbO_6F$ ($Ln = La, Pr, Nd$)⁸⁸. In these materials the F^- anion prefers to occupy equatorial or central apical anion sites in the double perovskite-like layers. It is thought this comes about by balancing of elastic energies of electronic interactions and $B-X$ bonds. These materials do not show any degree of long-range ordering, however.¹³ Some oxynitride RP materials, like Sr_2TaO_3N ,⁸⁹ tend to have full oxygen occupancy on apical bond sites and mixed N/O occupancy on the in-plane equatorial sites, which is thought to come about by the shorter $N-B$ bond lengths relaxing elastic energies in equatorial positions and the $O-B$ bond lengths preferring the larger volume of space in the apical sites.

4.1.2 Summary of Proposals from Theory

Theory work by Rondinelli *et al*^{71,75} explores new ways of designing and tuning materials for desired properties by incorporating different anions to create heteroanionic transition metal compounds.

Mixed-anion materials can accommodate transition metals in different oxidation states opposed to the pure oxides parent materials. An example is the oxidative fluorination reactions in the chromium Ruddlesden-Popper phases¹⁷ which oxidise Cr³⁺ to Cr⁴⁺: in addition to the F- anions occupying interstitial sites, the reduction in chromium cation size can lead to structural distortions such as octahedral rotations which are not present in the parent oxide.

Another possible distortion involves polar displacements of cations in polyhedra. In heteroanionic materials, due to the nature of the different *B-X* bonding, ordered anion arrangements can lead to the cations displacing off-centre. This is seen in *cis*-ordered oxy-nitrides SrMO₂N (*M* = Nb, Ta),⁹⁰ in which cations displace towards the nitride anions. It should be noted that whilst this would occur with *cis*, *mer* and *fac* ordered octahedra, it would not occur in *trans* arrangements. These arrangements form dipoles in the octahedra and give the possibility to design materials that break inversion symmetry, this gives the potential to target and tune properties that rely on non-centrosymmetric structures if these polar units can be packed to give overall polar crystal structures.

4.1.3 Aurivillius Oxyfluorides

In 1952, Aurivillius characterised the first oxyfluoride *n* = 1 Aurivillius materials: Bi₂NbO₅F, Bi₂TaO₅F and Bi₂TiO₄F₂ using X-ray powder diffraction and suggested ideal structures of (centrosymmetric) *I4/mmm* symmetry (Figure 4.1.1). Later the high symmetry structures reported would be investigated further due to reports of ferroelectricity.⁶⁵ The presence of ferroelectric properties would imply that these materials are non-centrosymmetric, inconsistent with the proposed high symmetry *I4/mmm* structure. In light of this, these materials were expected to be analogous to other lower symmetry single layered Aurivillius materials, such as Bi₂WO₆ which crystallises in the orthorhombic non-centrosymmetric *Pca2₁* space group.³⁵ XRPD is not a good analytical technique for characterising octahedral rotation/tilts in Aurivillius materials due to the large scattering by Bi³⁺ ions, which masks the scattering from light anions making it difficult to precisely determine anion positions.

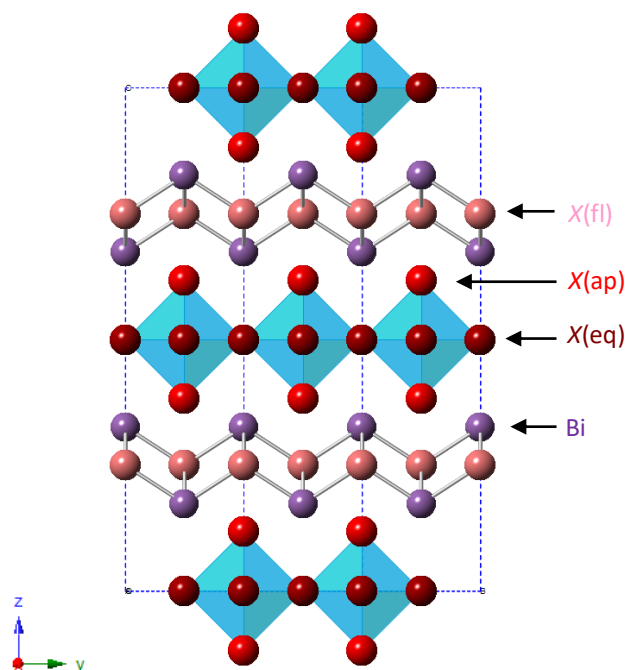


Figure 4.1.2 - Illustration of the structure of $\text{Bi}_2\text{TiO}_4\text{F}_2$ given a centrosymmetric $I4/mmm$ space group, showing BX_6 octahedra (blue), with apical, equatorial and fluorite $X(\text{ap})$, $X(\text{eq})$ and $X(\text{fl})$ anion sites highlighted in red, dark red and pink, respectively, separated by fluorite-like layers; consisting of bismuth (purple) and fluorite-layer anion site (pink).

A study by Needs *et al.*³² investigating the structures of both $\text{Bi}_2\text{NbO}_5\text{F}$ and $\text{Bi}_2\text{TiO}_4\text{F}_2$ suggested more distorted structures to those reported by Aurivillius.⁹¹ Room temperature NPD analysis found local disordering of the each anion site indicating some rotation of the BX_6 octahedra, but, found no evidence of an orthorhombic distortion. For $\text{Bi}_2\text{TiO}_4\text{F}_2$, it is difficult to differentiate between anions occupying each site at long and local ranges using NPD because of their similar neutron scattering lengths (for oxygen, O; $b_c = 5.803(4)$ fm, and for fluorine, F; $b_c = 5.654(12)$ fm⁵⁴). However, bond valence sum analysis showed that fluoride anions would probably take up the equatorial sites within the perovskite layers for both materials, in contrast to other oxyfluoride Ruddlesden-Popper phases in which the fluoride anions typically occupy apical sites.³² A slightly later study on $\text{Bi}_2\text{NbO}_5\text{F}$ proposed an orthorhombic structure of $Pbca$ symmetry (due to octahedral rotations) and suggested F^- occupancy of the apical anion sites in this Nb analogue.⁶⁵

The stoichiometry of $\text{Bi}_2\text{TiO}_4\text{F}_2$ implies that F^- anions could fully occupy anion sites in the fluorite layers, apical sites, or the equatorial sites. Madelung energy calculations for $\text{Bi}_2\text{NbO}_5\text{F}$ ⁶⁵ suggest that fluoride-occupation of anion sites in the fluorite-like layers is less favourable and it's likely that fluoride ions partially occupy anion sites in the perovskite-like layers. Madelung energy and bond valence sum calculations are likely to be sensitive to distortions such as rotations of BX_6 octahedra and for $\text{Bi}_2\text{TiO}_4\text{F}_2$, it is likely that F^- occupation of apical and equatorial sites are of similar energies, giving $[\text{TiO}_3\text{F}_3]$ octahedra. This led us to explore the thought experiment of possible ordered arrangements of *mer* and *fac* $[\text{TiO}_3\text{F}_3]$ units. There is no experimental evidence for such anion-ordering over long length scales in $\text{Bi}_2\text{TiO}_4\text{F}_2$ but if such ordering occurred even at a local length scale, short-range non-centrosymmetric regions could be found in the material, with interesting consequences for physical properties in perovskite-related oxyfluorides.

We hope to determine whether ordered arrangements of O and F over these two sites could break inversion symmetry. Our aim is to explore whether possible ordering patterns of O and F over the perovskite sites in $\text{Bi}_2\text{TiO}_4\text{F}_2$ can break inversion symmetry, and whether anion-ordering coupled with non-polar distortions (e.g., rotation of octahedra) might break inversion symmetry.

4.2 Symmetry Analysis

Here we discuss the symmetry analysis from our exploration of the possible lower symmetry anion-ordered structures of $\text{Bi}_2\text{TiO}_4\text{F}_2$ containing *mer* and *fac* $[\text{TiO}_3\text{F}_3]$ units. From a parent structure of $I4/mmm$ symmetry, the web-based ISODISTORT software^{49,50} was used to consider occupancy modes which could order anions over the apical (see Section 4.2.1.1) and equatorial (see Section 4.2.1.2) sites, see Figures 4.2.3. These modes could then be combined to give anion-ordered models of stoichiometry $\text{Bi}_2\text{TiO}_4\text{F}_2$ with O and F half occupying anion sites in perovskite layers in ordered arrangements. ISODISTORT was also used to explore further symmetry-lowering when non-polar octahedral rotations (X_2^+ and X_3^+) were coupled with non-polar anion-ordered arrangements to see whether this could be a further route to hybrid-improper polar behaviour.

4.2.1 Apical, Equatorial &/or Fluorite Layer occupancy

4.2.1.1 Ordering Over Apical Anion Sites

The O/F ordering of the apical anion sites (Figure 4.1.1a) can be described by the three irreps X_2^- , M_3^- and Γ_3^- , see Figure 4.2.1. The X_2^- irrep (Figure 4.2.1 left) describes ordering of O/F occupancy on upper and lower apical sites alternating within each perovskite layer. The M_3^- irrep (Figure 4.2.1 centre) shows ordering, where O/F occupancy of upper and lower apical sites alternates from layer to layer. Whilst these two ordering patterns causing local dipoles in the TiX_6 polyhedra, these two irreps give non-polar structures because individual dipoles are cancelled by neighbouring dipoles of opposite sign. The Γ_3^- irrep (Figure 4.2.1 right) is interesting as it lowers the symmetry to a polar $I4mm$ space group. It allows the O/F anions to occupy alternate apical sites between each layer of the Aurivillius material. This causes a net dipole along the long pseudo-tetragonal axis over the whole crystal.

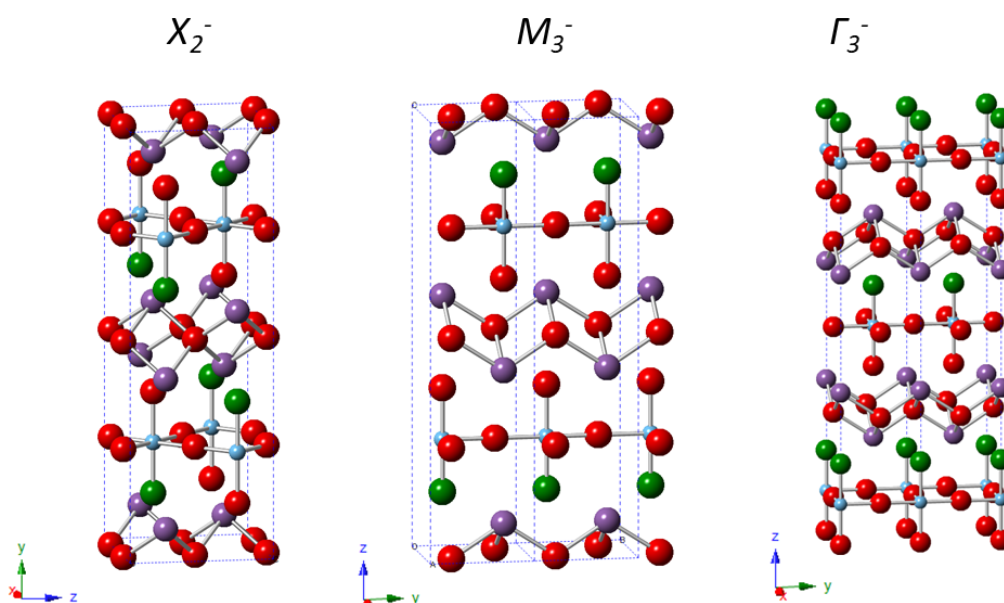


Figure 4.2.1 – Illustrations of $\text{Bi}_2\text{TiO}_4\text{F}_2$ space groups when acted on by apical anion site occupancy modes; (left) X_2^- , (centre) M_3^- and (right) Γ_3^- . Ions are represented by colours; bismuth (purple), titanium (blue), oxygen (red) and fluorine (green).

4.2.1.2 Ordering over Equatorial Anion Sites

Anion occupancy ordering of the equatorial anion sites (Figure 4.1.1a) can be described by four irreps: X_3^- , X_4^- , M_2^+ and Γ_2^+ , see Figure 4.2.2. The four irreps can be split into two groups; those that give *cis* ordering and those that give *trans* ordering. The M_2^+ and Γ_2^+ modes both give *trans* anion occupancy ordering. For M_2^+ the O/F occupation of equatorial sites alternate between layers, whereas, for the Γ_2^+ irrep the O/F occupation of the equatorial sites is the same on each layer. The X_3^- and X_4^- irreps both show *cis* anion

occupancy ordering; with X_4^- irrep showing the equatorial anion occupancy alternating along the long axis and the X_3^- irrep equatorial anion ordering alternates along the short axis.

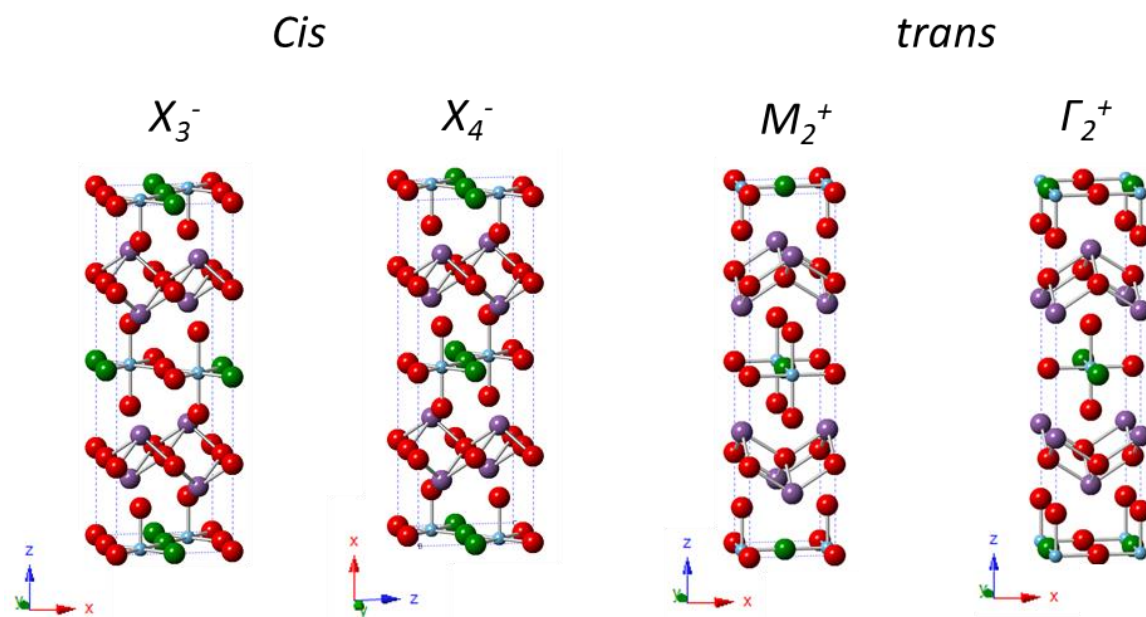


Figure 4.2.2 - Illustrations of $\text{Bi}_2\text{TiO}_4\text{F}_2$ space groups when acted on by equatorial anion site occupancy modes; (left) X_3^- ; (centre left) X_4^- ; (centre right) M_2^+ and (right) Γ_2^+ . Ions are represented by colours; bismuth (purple), titanium (blue), oxygen (red) and fluorine (green).

4.2.1.3 Ordered Anion Arrangements for $\text{Bi}_2\text{TiO}_4\text{F}_2$

Combining these apical and equatorial ordering modes will give stoichiometrically correct ordered structures containing either *mer*- or *fac*- $[\text{TiO}_3\text{F}_3]$ units. Combining any apical mode with *cis* equatorial modes (X_3^- and X_4^-) will give *fac* arrangements ($Pbcm$ (two settings), $Pccm$, $Ama2$, $Abm2$ and $Pnma$), whilst any apical mode with a *trans* equatorial modes (M_2^+ and Γ_2^+) will give *mer* arrangements ($P-4m2$, $Pmnn$, $P4_2mc$, $Imm2$, $Pnna$ and $Cmma$). The *fac* or *mer* arrangements adopted by the space groups are shown in Figure 4.2.4. To view the structure of each space group formed through the combinations of apical and equatorial occupancy modes listed in Figure 4.2.3, see Appendix B.1.

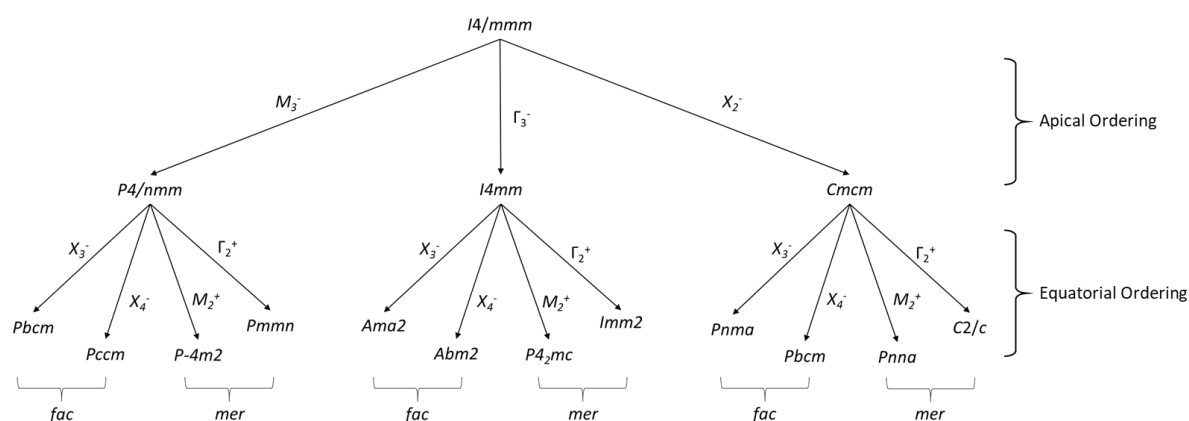


Figure 4.2.3 - Symmetry map showing possible space groups derived from likely apical anion occupational modes (1st tier) and likely equatorial anion occupational modes (2nd tier) when acting on high symmetry $I4/mmm$ $\text{Bi}_2\text{TiO}_4\text{F}_2$.

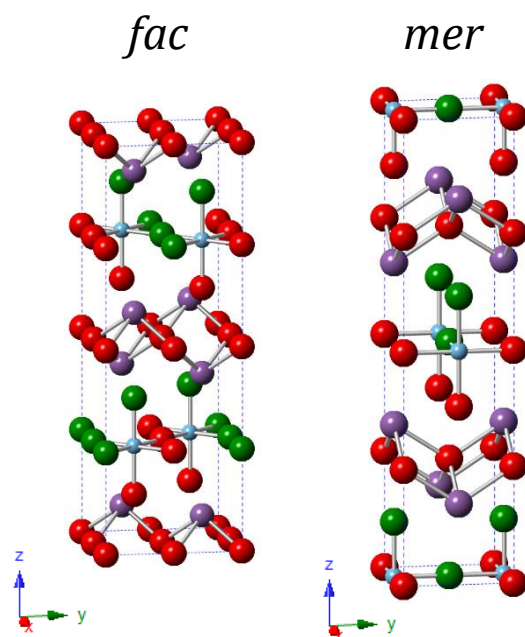


Figure 4.2.4 - Illustrations of possible anion-ordered structures of $\text{Bi}_2\text{TiO}_4\text{F}_2$ when acted on by anion site occupancy modes to give *mer* or *fac* arrangements. Ions are represented by colours; bismuth (purple), titanium (blue), oxygen (red) and fluorine (green). Showing (left) the *fac* arrangement of $Ama2$ symmetry from Γ_3^- and X_3^- modes and (right) the *mer* arrangement of $P4_2mc$ symmetry from Γ_3^- and M_2^+ modes

From the symmetry map above (see Figure 4.2.3), we note that there are six *fac* ordered structures: of $Pbcm$ symmetry (two settings), $Pccm$ symmetry, $Ama2$ symmetry, $Abm2$ symmetry and $Pnma$ symmetry. There are also six *mer* ordered structures: of $P-4m2$ symmetry, $Pmnn$ symmetry, $P4_2mc$ symmetry, $Imm2$ symmetry, $Pnna$ symmetry and $Cmma$ symmetry. Of the twelve structures, eight are non-polar ($P-4m2$, $Pbcm$ (appears twice), $Pccm$, $Pmnn$, $Pnna$, $Pnma$ and $Cmma$).

Polar apical ordering mode Γ_3^- breaks inversion symmetry giving non-centrosymmetric structures and would stabilise out-of-plane polarisation. Combinations of non-polar anion-ordering modes considered here do not combine to break inversion symmetry.

4.2.1.4 Anion ordering and non-polar displacive distortions for $\text{Bi}_2\text{TiO}_4\text{F}_2$

Our next concern was whether the combinations of non-polar occupational ordering modes might couple with non-polar distortions (octahedral rotational modes; X_2^+ and X_3^+) to break inversion symmetry. By applying octahedral rotational modes (X_2^+ and X_3^+) to the non-polar anion-ordered models we look at whether this can lead to the breaking of inversion symmetry.

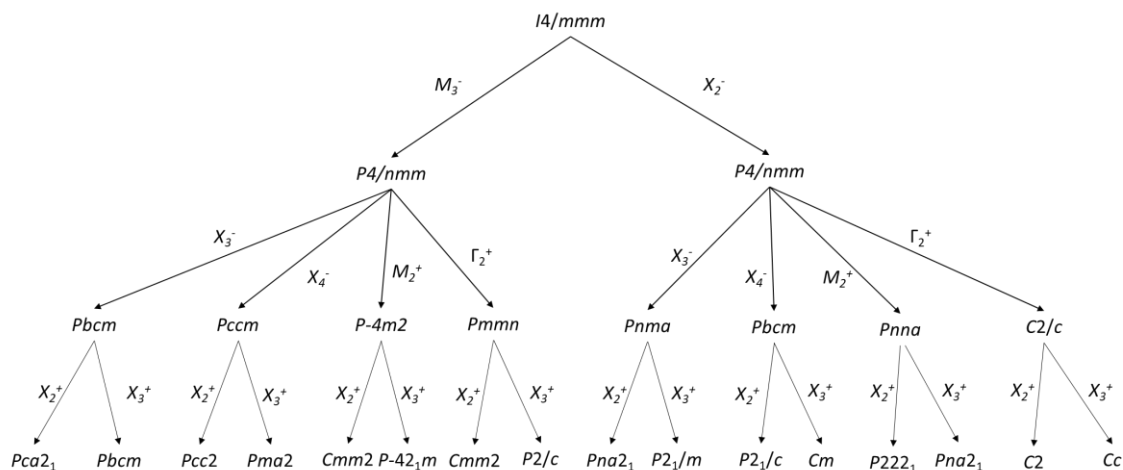


Figure 4.2.5 - Symmetry map showing possible space groups derived from the high symmetry $I4/mmm$ $Bi_2TiO_4F_2$ model. Showing (1st tier) Space groups when likely apical anion occupational modes applied and (2nd tier) Space groups when likely equatorial anion occupational modes are applied. (3rd tier) Space groups determined from coupling of non-polar apical and equatorial occupancy modes with non-polar octahedral rotation modes (X_2^+ and X_3^+).

We see from Figure 4.2.5, that the addition of non-polar rotational modes to the non-polar anion-ordered structures can give polar, non-centrosymmetric space groups (with the exception of a one space group: $P-42_1m$, being non-polar yet non-centrosymmetric). To view the structure of each space group in Figure 4.2.5, see Appendix B.2

4.2.2 Discussion

The symmetry analysis presented here has shown key factors that must be considered when deducing structure and anion ordering in heteroanionic materials. It has been shown that both apical and equatorial occupancy modes can couple to give lower symmetry anion-ordered materials (with *fac* or *mer* $[TiO_3F_3]$ units) with polar or non-polar symmetries. Combinations of non-polar occupancy modes cannot combine to break inversion symmetry, only the polar Γ_3^- apical occupancy mode can give polar structures. These structures stabilise the out-of-plane polarisation.

Although the $[TiO_3F_3]$ units are polar, the symmetry analysis presented here highlights the difficulty in using these polar units to design and synthesise polar materials: there are 12 possible anion-ordered models and only four are polar (resulting from the polar apical ordering mode Γ_3^-). It would be interesting to compare the relative energies of these structures by computational methods, especially if other distortions allowed by symmetry (such as out-of-centre displacements) are included.

As seen in Figure 4.2.5, non-polar anion-ordered models can couple with rotational modes, X_2^+ and X_3^+ , to give polar, non-centrosymmetric space groups. We find that all coupling combinations can lead to non-centrosymmetric symmetries, depending on the order parameter direction. These models are likely to be of similar energies and even if long-range order of anions and tilts may not occur, this symmetry analysis suggests the possibility of short-range polar/non-centrosymmetric regions.

4.2.3 Conclusion

Work by Rondinelli *et al.*⁷¹ has outlined the importance of heteroanionic materials in designing new functional materials. Our symmetry analysis of anion-ordered arrangements in $Bi_2TiO_4F_2$ containing polar $[TiO_3F_3]$ units illustrate the challenge in packing these polar units to give polar structures, rather than centrosymmetric packing arrangements which are statistically more likely. This has been explored in other classes of oxyfluorides⁸⁴ who also highlight the short-range ordering that can occur.

However, our finding that combining anion ordering and octahedral rotations can break inversion symmetry gives new direction in designing ferroic materials by combining non-polar structural features. Over short length scales, this could lead to materials with non-centrosymmetric, possibly polar, nano-regions and relaxor ferroelectric-like behaviour.^{46,92,93}

CHAPTER 5

Conclusions

5.1 Characterisation of $\text{Bi}_2\text{CoO}_2\text{F}_4$

Results discussed in *Chapter 3* show that the high symmetry tetragonal $\bar{1}4$ structure, suggested in literature,⁴⁷ was not sufficient to describe the $\text{Bi}_2\text{CoO}_2\text{F}_4$ structure determined from NPD analysis. Refinements using 5 K and 50 K NPD data, combined with symmetry analysis using ISODISTORT, suggested that the ground state structure of $\text{Bi}_2\text{CoO}_2\text{F}_4$ involves rotation of CoX_6 octahedral about both an in-plane and an out-of-plane axis. The non-centrosymmetric nature of the material, indicated by its SHG activity, suggests that the average structure is best described by a model of $Pca2_1$ symmetry. Bond valence sum analysis suggested that oxide anions are located in the fluorite-like $[\text{Bi}_2\text{O}_2]^{2+}$ layers, giving CoF_6 corner-linked octahedral in the perovskite layers.

NPD data at 5 K revealed extra Bragg peaks resulting from long-range magnetic order. These could be fitted fairly well by collinear antiferromagnetic models with Co^{2+} moments along either [100] or [001] directions of the nuclear unit cell. However, the two models expected by symmetry allow non-collinear moments and one model, the $m\Gamma_2^+$ model, allows a ferromagnetic component, consistent with magnetic susceptibility measurements on $\text{Bi}_2\text{CoO}_2\text{F}_4$.⁴⁷

It would be interesting to carry out magnetic susceptibility measurements and neutron diffraction measurements on single crystals of $\text{Bi}_2\text{CoO}_2\text{F}_4$ to give further insight into the magnetic order. In addition, density functional theory calculations would be able to probe the ground state structure and any phase transitions, as well as differentiate energy differences between the proposed magnetic structures.

Although reversible polarisation has not yet been demonstrated (e.g., by ferroelectric hysteresis loop), this material is promising in designing multiferroics, particularly with the ferromagnetic component to the magnetic structure. Other magnetic oxyfluoride Aurivillius materials might be prepared e.g., $\text{Bi}_2\text{MnO}_4\text{F}_2$, $\text{Bi}_2\text{NiO}_3\text{F}_3$ or $\text{Bi}_3\text{Fe}_x\text{Ti}_{2-x}\text{O}_5\text{F}_4$, making use of the lower B cation oxidation states possible in oxyfluorides compared with the pure oxide phases.

5.2 Anion Order to Break Inversion Symmetry

As seen in *Chapter 4*, occupational and structural symmetry analysis of possible anion-ordered structures built from polar $[\text{TiO}_3\text{F}_3]$ units was completed on the $n = 1$ Aurivillius heteroanionic oxyfluoride material $\text{Bi}_2\text{TiO}_4\text{F}_2$, reported in literature to be ferroelectric^{94,95} and have somewhat disordered occupancy of anions over anion sites.^{32,65} Experimental work has not given evidence for long-range ordering of the F^- and O^{2-} anions, however, it is likely that the F^- anions occupy half of the anion sites in the perovskite layer. The work we present explores the O^{2-}/F^- ordered arrangements over the apical and equatorial sites.

Our symmetry analysis highlights the difficulty of packing these polar units to give overall polar structures, with only a third of the anion-ordered models giving the possibility of non-centrosymmetric structures with a macroscopic polarisation. It would be interesting to explore the relative energies of these anion-ordered models (and models including displacements allowed by their lower symmetries) by computational methods.

Although not many combinations of anion ordering modes couple to break inversion symmetry, subsequent analysis has demonstrated that the addition of non-polar distortion modes (i.e., octahedral tilts/rotations) to these non-polar anion-ordered models will often break inversion symmetry, creating non-centrosymmetric, possibly polar, symmetries. This suggests a new avenue to explore the design of polar materials using hybrid-improper routes.

Multiferroic materials (combining more than one ferroic order parameter such as ferroelectricity and ferromagnetism) are rare.⁹⁶ The Aurivillius oxyfluorides should be explored more widely as potential multiferroics: replacement of some oxide coordinated around B cations the with fluoride anions can allow

lower oxidation states to be incorporated, e.g., as explored in *chapter 3* the magnetic Co^{2+} Aurivillius phase, but also other magnetic ions could be explored (e.g., Ni, Fe or Mn)

Stoichiometries that allow half partial occupation of apical and equatorial sites by both O^{2-} and F^- (e.g., $\text{Bi}_2\text{BO}_3\text{F}_3$, in addition to $\text{Bi}_2\text{BO}_4\text{F}_2$ explored here) could allow some anion-ordering, most likely short range, but combined with rotations of BX_6 octahedra, this could drive a break in inversion symmetry, even if only at a short length scale. This could provide a new route into the design of materials with relaxor behaviour.

Bibliography

- 1 R. Tilley, *Perovskites*, John Wiley & Sons, LTD, Chichester, 1st edn., 2016.
- 2 J. Hyuck Heo, S. Hyuk Im, J. Hong Noh, T. N. Mandal, C.-S. Lim, J. Ah Chang, Y. Hui Lee, H. Kim, A. Sarkar, M. K. Nazeeruddin, M. Grätzel and S. Il Seok, *Nat. Phot.*, 2013, **7**, 486–491.
- 3 N. A. Benedek, *Inorg. Chem.*, 2014, **53**, 3769–3777.
- 4 B. L. Chamberland, A. W. Sleight and J. F. Weiher, *J. Solid State Chem.*, 1970, **1**, 506–511.
- 5 H. F. Kay and P. C. Bailey, *Acta Crystallogr.*, 1957, **10**, 219–226.
- 6 C. Li, K. C. K. Soh and P. Wu, *J. Alloys Compd.*, 2004, **372**, 40–48.
- 7 L. M. Feng, L. Q. Jiang, M. Zhu, H. B. Liu, X. Zhou and C. H. Li, *J. Phys. Chem. Solids*, 2008, **69**, 967–974.
- 8 C. Li, X. Lu, W. Ding, L. Feng, Y. Gao and Z. Guo, *Acta Crystallogr. Sect. B Struct. Sci.*, 2008, **64**, 702–707.
- 9 N. A. Benedek, J. M. Rondinelli, H. Djani, P. Ghosez and P. Lightfoot, *Dalt. Trans.*, 2015, 44, 10543–10558.
- 10 D. Iwanaga, Y. Inaguma and M. Itoh, *J. Solid State Chem.*, 1999, **147**, 291–295.
- 11 A. Walsh, D. J. Payne, R. G. Egdell and G. W. Watson, *Chem. Soc. Rev.*, 2011, **40**, 4455–4463.
- 12 K. T. Butler, *J. Mater. Chem. C*, 2018, **6**, 12045–12051.
- 13 Y. Tsujimoto, K. Yamaura and E. Takayama-Muromachi, *Appl. Sci.*, 2012, **2**, 206–219.
- 14 C. Greaves and M. G. Francesconi, *Curr. Opin. Solid State Mater. Sci.*, 1998, **3**, 132–136.
- 15 E. E. McCabe and C. Greaves, *J. Fluor. Chem.*, 2007, 128, 448–458.
- 16 P. R. Slater and K. B. Gover, *J. Mater. Chem.*, 2001, **11**, 2035–2038.
- 17 R. Zhang, G. Read, F. Lang, T. Lancaster, S. J. Blundell and M. A. Hayward, *Inorg. Chem.*, 2016, **55**, 3169–3174.
- 18 R. Zhang, A. S. Gibbs, W. Zhang, P. Shiv Halasyamani and M. A. Hayward, *Inorg. Chem*, 2017, **56**, 9988–9995.
- 19 F. D. Romero, P. A. Bingham, S. D. Forder and M. A. Hayward, *Inorg. Chem.*, 2013, **52**, 3388–3398.
- 20 M. Dion, M. Ganne and M. Tournoux, *Mater. Res. Bull.*, 1981, **16**, 1429–1435.
- 21 A. J. Jacobson, J. T. Lewandowski and J. W. Johnson, *J. Less-Common Met.*, 1986, **116**, 137–146.
- 22 T. Zhu, T. Cohen, A. S. Gibbs, W. Zhang, P. Shiv Halasyamani, M. A. Hayward and N. A. Benedek, *Chem. Mater*, 2017, **29**, 9489–9497.
- 23 J. A. Kurzman and M. J. Geselbracht, in *Materials Research Society Symposium Proceedings*, Materials Research Society, 2006, vol. 988, pp. 74–79.
- 24 B. Aurivillius, *Ark. Kemi*, 1949, **1**, 463–480.
- 25 S. Dubey and R. Kurchania, *Bull. Mater. Sci.*, 2015, **38**, 1881–1889.
- 26 H. Djani, E. E. McCabe, W. Zhang, P. S. Halasyamani, A. Feteira, J. Bieder, E. Bousquet and P. Ghosez, *Phys. Rev. B*, 2020, **101**, 134113.
- 27 N. Kim, R. N. Vannier and C. P. Grey, *Chem. Mater.*, 2005, **17**, 1952–1958.
- 28 A. Kudo and S. Hiji, *Chem. Lett.*, 1999, 1103–1104.
- 29 E. E. McCabe and C. Greaves, *J. Mater. Chem.*, 2005, **15**, 177–182.

- 30 Z. Pan, P. Wang, X. Hou, L. Yao, G. Zhang, J. Wang, J. Liu, M. Shen, Y. Zhang, S. Jiang, J. Zhai and Q. Wang, *Adv. Energy Mater.*, 2020, **10**, 2001536.
- 31 J. G. Thompson, S. Schmid, R. L. Withers, A. D. Rae and J. D. F. Gerald, *J. Solid State Chem.*, 1992, **101**, 309–321.
- 32 R. L. Needs, S. E. Dann, M. T. Weller, J. C. Cherryman and R. K. Harris, *J. Mater. Chem.*, 2005, **15**, 2399–2407.
- 33 E. E. McCabe, I. P. Jones, D. Zhang, N. C. Hyatt and C. Greaves, *J. Mater. Chem.*, 2007, **17**, 1193–1200.
- 34 K. S. Knight, *Ferroelectrics*, 1993, **150**, 319–330.
- 35 N. A. McDowell, K. S. Knight and P. Lightfoot, *Chem. - A Eur. J.*, 2006, **12**, 1493–1499.
- 36 H. D. Megaw, *Acta Crystallogr.*, 1952, **5**, 739–749.
- 37 T. Zheng, J. Wu, D. Xiao and J. Zhu, *Prog. Mater. Sci.*, 2018, **98**, 552–624.
- 38 M. Stewart, M. G. Cain and D. A. Hall, *NPL Report CMMT(A) 152 Ferroelectric Hysteresis Measurement & Analysis*, 1999.
- 39 E. Bousquet, M. Dawber, N. Stucki, C. Lichtensteiger, P. Hermet, S. Gariglio, J. M. Triscone and P. Ghosez, *Nature*, 2008, **452**, 732–736.
- 40 N. A. Benedek and C. J. Fennie, *Phys. Rev. Lett.*, 2011, **106**, 107204.
- 41 N. A. Benedek, A. T. Mulder and C. J. Fennie, *J. Solid State Chem.*, 2012, **195**, 11–20.
- 42 M. S. Senn, A. Bombardi, C. A. Murray, C. Vecchini, A. Scherillo, X. Luo and S. W. Cheong, *Phys. Rev. Lett.*, 2015, **114**, 035701.
- 43 N. A. Benedek, *Inorg. Chem.*, 2014, **53**, 3769–3777.
- 44 V. A. Cascos, J. Roberts-Watts, C. Skingle, I. Levin, W. Zhang, P. S. Halasyamani, M. C. Stennett, N. C. Hyatt, E. Bousquet and E. E. McCabe, *Chem. Mater.*, 2020, **32**, 8700–8712.
- 45 J. D. Bobic, M. M. Vijatovic Petrovic and B. D. Stojanovic, in *Magnetic, Ferroelectric, and Multiferroic Metal Oxides*, Elsevier, 2018, pp. 233–249.
- 46 G. Stone, C. Ophus, T. Birol, J. Ciston, C. H. Lee, K. Wang, C. J. Fennie, D. G. Schlom, N. Alem and V. Gopalan, *Nat. Commun.*, 2016, **7**, 1–9.
- 47 E. Mitoudi Vagourdi, S. Mu, P. Lemmens, R. K. Kremer and M. Johnsson, *Cite This Inorg. Chem*, 2018, **57**, 9121.
- 48 A. C. Hannon, in *Nuclear Instruments and Methods in Physics Research, Section A: Accelerators, Spectrometers, Detectors and Associated Equipment*, North-Holland, 2005, vol. 551, pp. 88–107.
- 49 H. T. Stokes, D. M. Hatch and B. J. Campbell, ISODISTORT, ISOTROPY Softw. Suite, iso.byu.edu.
- 50 B. J. Campbell, H. T. Stokes, D. E. Tanner and D. M. Hatch, *J. Appl. Cryst.*, 2006, **39**, 607–614.
- 51 J. A. Bearden and A. F. Burr, *Rev. Mod. Phys.*, 1967, **39**, 125–142.
- 52 J. M. Bueno, F. J. Ávila and P. Artal, in *Microscopy and Analysis*, InTech, 2016.
- 53 K. M. Ok, E. O. Chi and P. S. Halasyamani, *Chem. Soc. Rev.*, 2006, **35**, 710–717.
- 54 V. F. Sears, *Neutron News*, 1992, **3**, 26–37.
- 55 N. E. Brese and M. O’Keeffe, *Acta Crystallogr. Sect. B*, 1991, **47**, 192–197.
- 56 I. D. Brown and D. Altermatt, *Acta Crystallogr. Sect. B*, 1985, **41**, 244–247.
- 57 A. A. Coelho, *J. Appl. Crystallogr.*, 2003, **36**, 86–95.
- 58 A. A. Coelho, *Topas Academic: General profile and structure analysis software for powder diffraction*

- data*, Bruker AXS: Karlsruhe, 2012.
- 59 A. J. Dent, G. Cibin, S. Ramos, A. D. Smith, S. M. Scott, L. Varandas, M. R. Pearson, N. A. Krumpa, C. P. Jones and P. E. Robbins, in *Journal of Physics: Conference Series*, Institute of Physics Publishing, 2009, vol. 190, p. 012039.
- 60 B. Ravel and M. Newville, in *Journal of Synchrotron Radiation*, J Synchrotron Radiat, 2005, vol. 12, pp. 537–541.
- 61 F. J. Berry, E. Moore, M. Mortimer, X. Ren, R. Heap, P. Slater and M. F. Thomas, *J. Solid State Chem.*, 2008, **181**, 2185–2190.
- 62 A. J. Tuxworth, E. E. McCabe, D. G. Free, S. J. Clark and J. S. O. Evans, *Inorg. Chem.*, 2013, **52**, 2078–2085.
- 63 X. Yu, E. Mitoudi-Vagourdi and M. Johnsson, *ChemCatChem*, 2019, **11**, 6105–6110.
- 64 N. E. Brese and M. O’Keeffe, *Acta Crystallogr. Sect. B*, 1991, **47**, 192–197.
- 65 E. E. McCabe, I. P. Jones, D. Zhang, N. C. Hyatt and C. Greaves, *J. Mater. Chem.*, 2007, **17**, 1193–1200.
- 66 J. Wang, W. Zhang and D. Y. Xing, *Phys. Rev. B - Condens. Matter Mater. Phys.*, 2000, **62**, 14140–14144.
- 67 J. H. N. Van Vucht and K. H. J. Buschow, *J. Less-Common Met.*, 1976, **46**, 133–138.
- 68 K. Yamada, M. Matsuda, Y. Endoh, B. Keimer, R. J. Birgeneau, S. Onodera, J. Mizusaki, T. Matsuura and G. Shirane, *Phys. Rev. B*, 1989, **39**, 2336–2343.
- 69 J. L. Knutson, J. D. Martin and D. B. Mitzi, *Inorg. Chem.*, 2005, **44**, 4699–4705.
- 70 D. Ghosh, A. Aziz, J. A. Dawson, A. B. Walker and M. S. Islam, *Chem. Mater.*, 2019, **31**, 4063–4071.
- 71 J. K. Harada, N. Charles, K. R. Poeppelmeier and J. M. Rondinelli, *Adv. Mater.*, 2019, **31**, 1–26.
- 72 L. Clark, J. Oró-Solé, K. S. Knight, A. Fuertes and J. P. Attfield, *Chem. Mater.*, 2013, **25**, 5004–5011.
- 73 G. Pilania, A. Ghosh, S. T. Hartman, R. Mishra, C. R. Stanek and B. P. Uberuaga, *npj Comput. Mater.*, 2020, **6**, 1–11.
- 74 S. J. Clarke, P. Adamson, S. J. C. Herkelrath, O. J. Rutt, D. R. Parker, M. J. Pitcher and C. F. Smura, *Inorg. Chem.*, 2008, **47**, 8473–8486.
- 75 N. Charles, R. J. Saballos and J. M. Rondinelli, *Chem. Mater.*, 2018, **30**, 32.
- 76 M. Yang, J. Oró-Solé, J. A. Rodgers, A. B. Jorge, A. Fuertes and J. P. Attfield, *Nat. Chem.*, 2011, **3**, 47–52.
- 77 Y. Tsujimoto, K. Yamaura and E. Takayama-Muromachi, *Appl. Sci.*, 2012, **2**, 206–219.
- 78 Y. Tsujimoto, Y. Matsushita, N. Hayashi, K. Yamaura and T. Uchikoshi, *Cryst. Growth Des.*, 2014, **14**, 4278–4284.
- 79 D. Oka, Y. Hirose, H. Kamisaka, T. Fukumura, K. Sasa, S. Ishii, H. Matsuzaki, Y. Sato, Y. Ikuhara and T. Hasegawa, *Sci. Rep.*, 2014, **4**, 1–6.
- 80 D. A. Headspith, E. Sullivan, C. Greaves and M. G. Francesconi, *Dalt. Trans.*, 2009, **42**, 9273–9279.
- 81 S. Adachi, T. Tatsuki, T. Sugano, A. Tokiwa-Yamamoto and K. Tanabe, *Phys. C*, 2000, **334**, 87–94.
- 82 J. Gopalakrishnan, *Chem. Mater.*, 1995, **7**, 1265–1275.
- 83 K. Wissel, J. Heldt, P. B. Groszewicz, S. Dasgupta, H. Breitzke, M. Donzelli, A. I. Waidha, A. Dominic, J. Rohrer, P. R. Slater, G. Buntkowsky and O. Clemens, *Inorg. Chem.*, 2018, **57**, 6549–6560.
- 84 R. L. Withers, F. J. Brink, Y. Liu and L. Norén, *Polyhedron*, 2007, **26**, 290–299.
- 85 Y. Tsujimoto, Y. Matsushita, N. Hayashi, K. Yamaura and T. Uchikoshi, *Cryst. Growth Des.*, 2014, **14**, 4278–4284.

- 86 M. Goga, R. Seshadri, V. Ksenofontov, P. Gütlich and W. Tremel, *Chem. Commun.*, 1999, 979–980.
- 87 J. H. Choy, J. Y. Kim, S. J. Kim, J. S. Sohn and Oc Hee Han, *Chem. Mater.*, 2001, **13**, 906–912.
- 88 G. Caruntu, L. Spinu and J. B. Wiley, *Mater. Res. Bull.*, 2002, **37**, 133–140.
- 89 N. Diot, R. Marchand, J. Haines, J. M. Léger, P. Macaudière and S. Hull, *J. Solid State Chem.*, 1999, **146**, 390–393.
- 90 J. P. Attfield, *Cryst. Growth Des.*, 2013, **13**, 4623–4629.
- 91 B Aurivillius, *Ark. Kemi*, 1952, **5(4)**, 39.
- 92 C. Elissalde, A. Simon and J. Ravez, *Ferroelectrics*, 1997, **199**, 217–221.
- 93 A. Peliz-Barranco, F. Caldern-Piar, O. Garca-Zaldvar and Y. Gonzalez-Abreu, in *Advances in Ferroelectrics*, InTech, 2012.
- 94 T. Katayama, S. Mo, T. Maruyama, A. Chikamatsu and T. Hasegawa, *Dalt. Trans.*, 2019, **48**, 5425–5428.
- 95 J. Chen, H. Liu, L. Zhu, Z. Fu and Y. Lu, *J. Alloys Compd.*, 2021, **873**, 159847.
- 96 N. A. Hill, *J. Phys. Chem. B*, 2000, **104**, 6694–6709.

Appendices

Appendix A - Characterisation of $\text{Bi}_2\text{CoO}_2\text{F}_4$

1.6 Pawley Refinements of XRPD Data

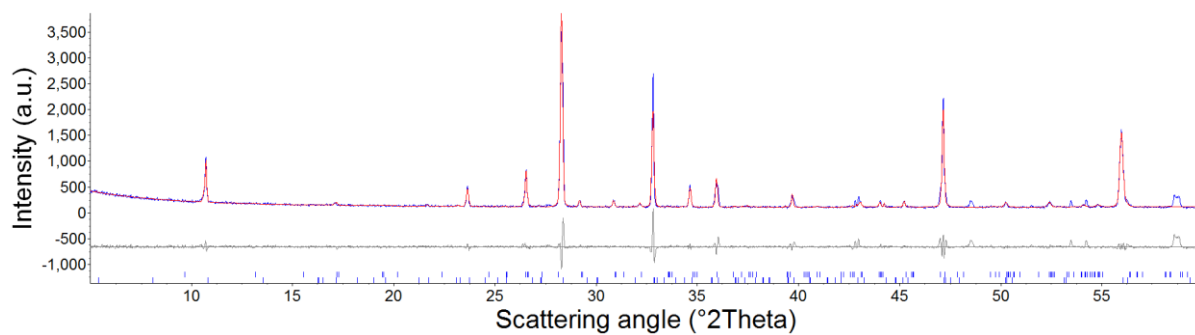


Figure 1.6.1 - Observed (-), calculated (-) and difference (-) profiles of Pawley refinement using XRPD data of $\text{Bi}_2\text{CoO}_2\text{F}_4$; Tetragonal $P4$, $a = 5.4402(3)$, $c = 32.6745(8)$, $R_{\text{wp}} = 13.38\%$, $R_p = 8.58\%$, $\chi^2 = 3.37$. The impurity phase, $\text{Bi}_7\text{F}_{11}\text{O}_5$ and lower symmetry elements are marked by upper blue ticks and lower blue ticks, respectively.

1.7 Enhanced Images of Tetragonal and Orthorhombic 50 K NPD Refinement Reflections

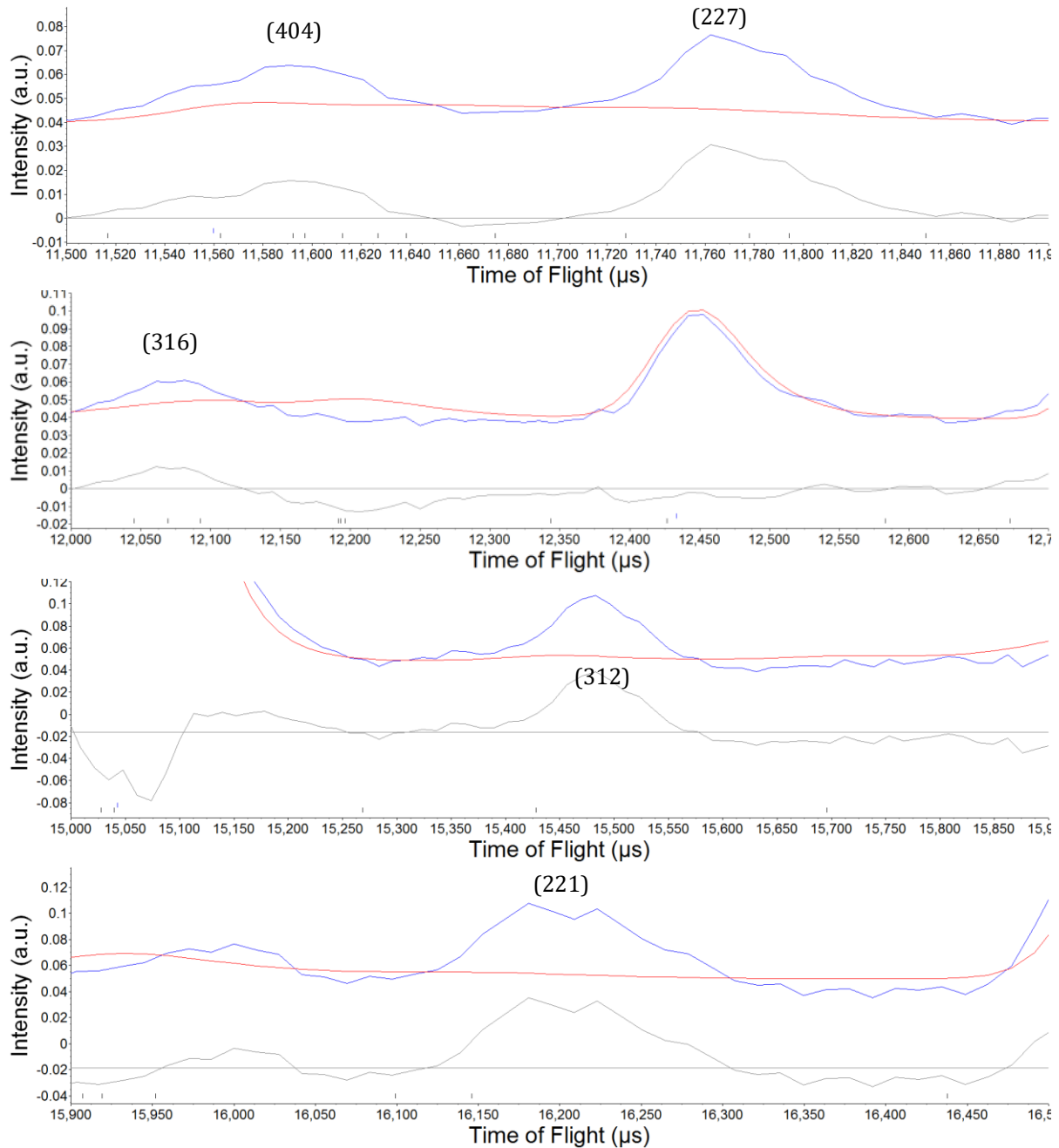


Figure 1.7.1 - Enhanced images of selected peaks from Rietveld refinement of 50 K NPD data of $\text{Bi}_2\text{CoO}_2\text{F}_4$ using tetragonal $I4/mmm$ model, $a = 3.8422(3) \text{ \AA}$, $c = 16.354(2) \text{ \AA}$, $R_{wp} = 9.77\%$, $R_p = 6.82\%$, $\chi^2 = 6.89$. Reflection positions of main phase and $\text{Bi}_7\text{F}_{11}\text{O}_5$ (8(2) % by weight) are marked by upper blue ticks and middle black ticks, respectively. The unmatched peaks are labelled with their hkl values with respects to the $P222$, $5.4 \text{ \AA} \times 5.4 \text{ \AA} \times 16.4 \text{ \AA}$ unit cell.

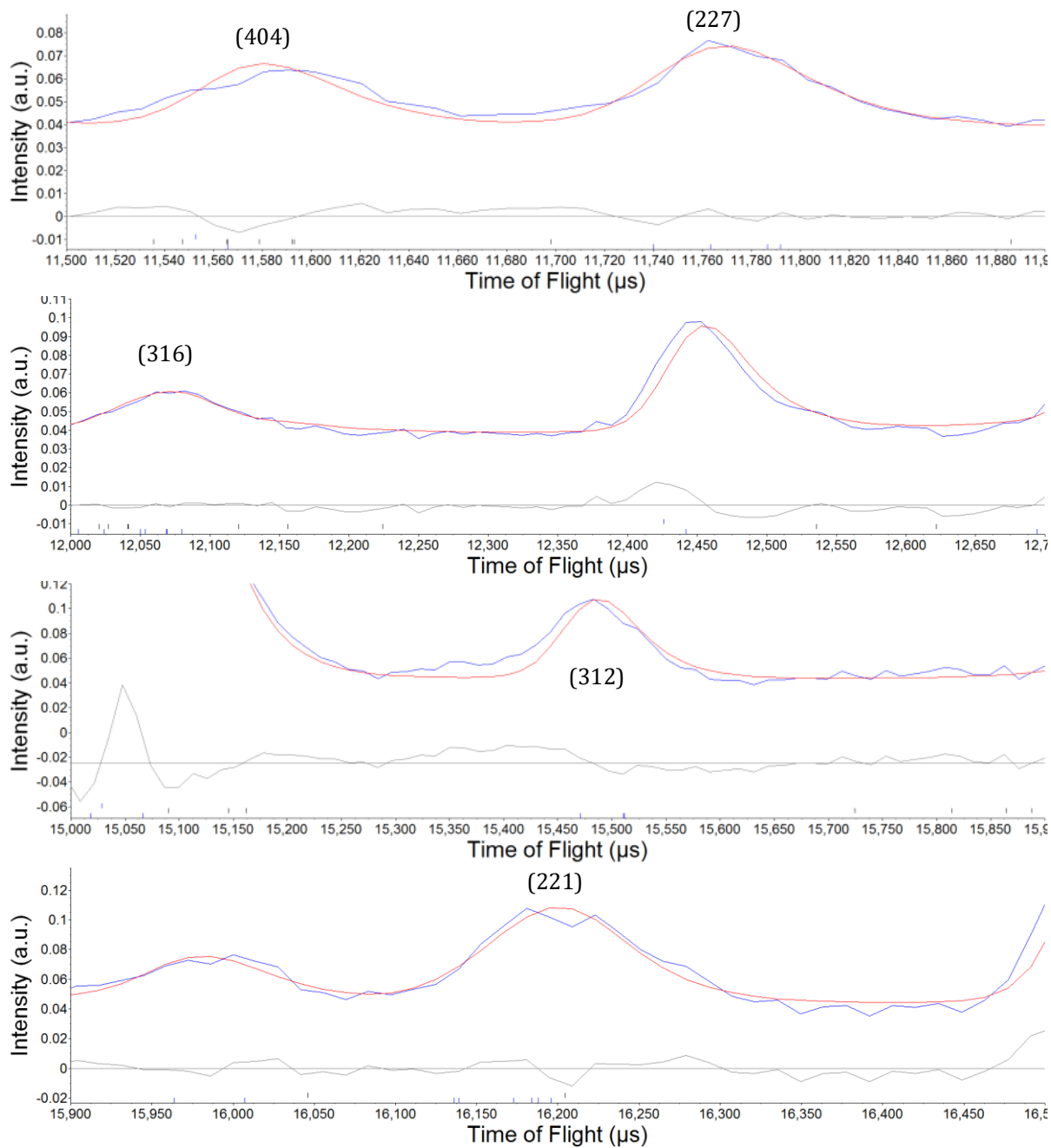


Figure 1.7.2 - Enhanced images of selected peaks from Pawley refinement of 50 K NPD data of $\text{Bi}_2\text{CoO}_2\text{F}_4$ using Orthorhombic P222 model $a = 5.447(6)$, $b = 5.427(6)$ Å, $c = 16.37(2)$, $R_{wp} = 7.57\%$, $R_p = 6.02\%$, $\chi^2 = 6.38$. Reflection positions of main phase and $\text{Bi}_7\text{F}_{11}\text{O}_5$ (8(2) % by weight) are marked by upper blue ticks and middle black ticks, respectively. The previously unmatched peaks are labelled with their hkl values with respects to the P222, 5.4 Å x 5.4 Å x 16.4 Å unit cell.

1.8 Pawley Refinements of 50 K NPD Data using Various Unit Cell Parameters

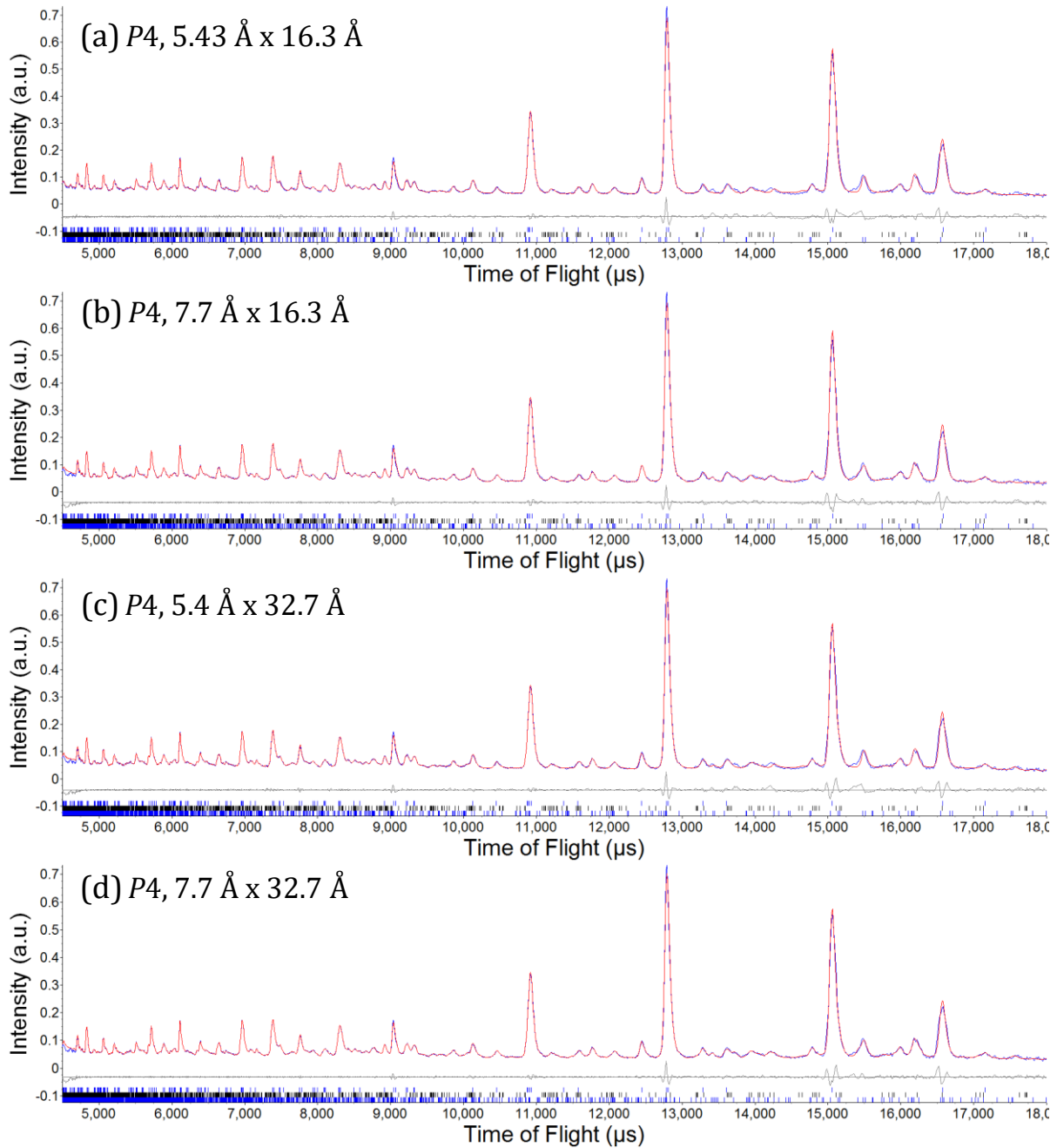


Figure 1.8.1 - Pawley refinements showing observed (-), calculated (-) and difference (-) profiles using 50 K NPD data of $\text{Bi}_2\text{CoO}_2\text{F}_4$ with respect to (a) Tetragonal $P4$, $a = 5.433(7)$, $c = 16.33(2)$, $R_{wp} = 8.17\%$, $R_p = 6.68\%$, $\chi^2 = 6.13$; (b) Tetragonal $P4$, $a = 7.684(2)$, $c = 16.336(2)$, $R_{wp} = 8.03\%$, $R_p = 6.49\%$, $\chi^2 = 8.36$; (c) Tetragonal $P4$, $a = 5.4323(9)$, $c = 32.68(1)$, $R_{wp} = 8.22\%$, $R_p = 6.65\%$, $\chi^2 = 8.66$; and (d) Tetragonal $P4$, $a = 7.683(8)$, $c = 32.7(1)$, $R_{wp} = 7.91\%$, $R_p = 6.35\%$, $\chi^2 = 39.68$. The main $14/mmm$ Rietveld phase, impurity phase, $\text{Bi}_7\text{F}_{11}\text{O}_5$ and lower symmetry Pawley phases are marked by upper blue ticks, middle black ticks, and lower blue ticks, respectively.

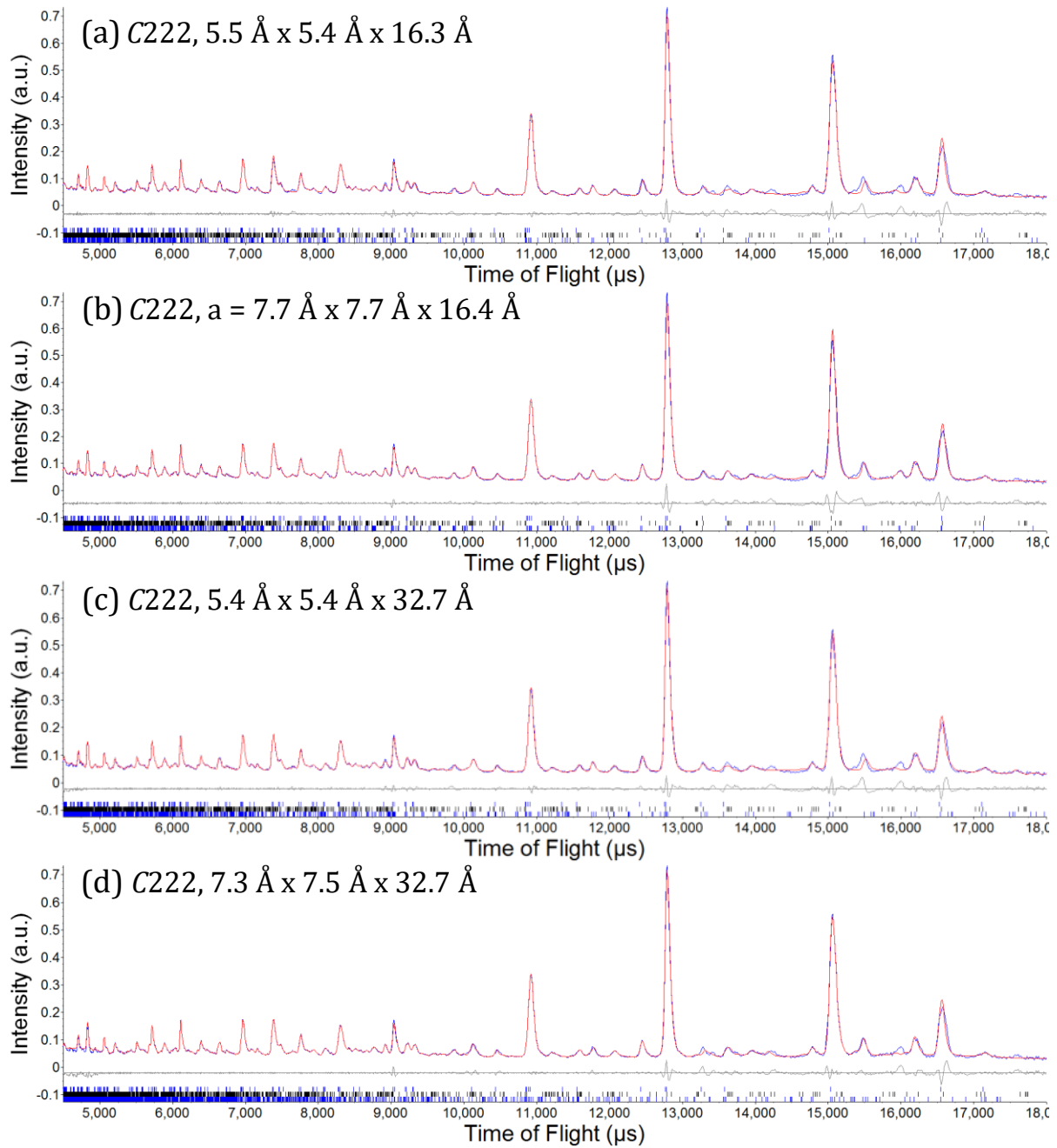


Figure 1.8.2 - Pawley refinements showing observed (-), calculated (-) and difference (-) profiles using 50 K NPD data of $\text{Bi}_2\text{CoO}_2\text{F}_4$ with respect to (a) Orthorhombic C222, $a = 5.450(1)$, $b = 5.428(1)$, $c = 16.316(5)$, $R_{wp} = 8.46\%$, $R_p = 6.85\%$, $\chi^2 = 5.88$; (b) Orthorhombic C222, $a = 7.691(6)$, $b = 7.683(6)$, $c = 16.390(7)$, $R_{wp} = 8.11\%$, $R_p = 6.61\%$, $\chi^2 = 6.24$; (c) Orthorhombic C222, $a = 5.448(2)$, $b = 5.425(2)$, $c = 32.664(9)$, $R_{wp} = 8.37\%$, $R_p = 6.77\%$, $\chi^2 = 6.77$; and (d) Orthorhombic C222, $a = 7.286(3)$, $a = 7.487(3)$, $c = 32.66(1)$, $R_{wp} = 8.17\%$, $R_p = 6.59\%$, $\chi^2 = 8.86$. The main 14/mmm Rietveld phase, impurity phase, $\text{Bi}_7\text{F}_{11}\text{O}_5$ and lower symmetry Pawley phases are marked by upper blue ticks, middle black ticks, and lower blue ticks, respectively.

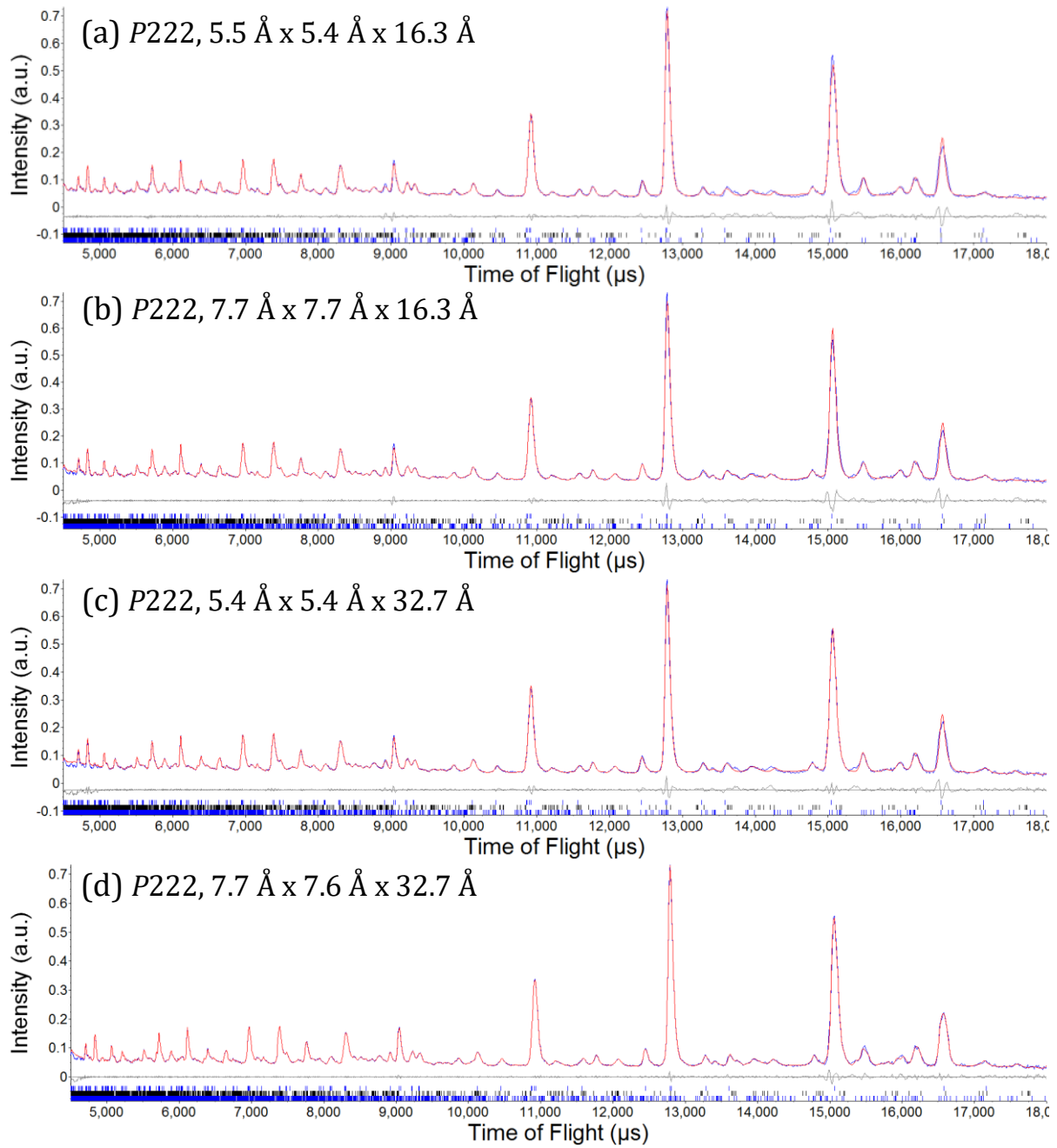


Figure 1.8.3 - Pawley refinements showing observed (-), calculated (-) and difference (-) profiles using 50 K NPD data of $\text{Bi}_2\text{CoO}_2\text{F}_4$ with respect to (a) Orthorhombic P222, $a = 5.454(2)$, $b = 5.428(2)$, $c = 16.349(8)$, $R_{wp} = 8.09\%$, $R_p = 6.60\%$, $\chi^2 = 6.311$; (b) Orthorhombic P222, $a = 7.68(1)$, $b = 7.67(1)$, $c = 16.337(9)$, $R_{wp} = 7.94\%$, $R_p = 6.46\%$, $\chi^2 = 9.01$; (c) Orthorhombic P222, $a = 5.441(5)$, $b = 5.422(5)$, $c = 32.69(2)$, $R_{wp} = 8.26\%$, $R_p = 6.65\%$, $\chi^2 = 10.06$; and (d) Orthorhombic P222, $a = 7.68(8)$, $b = 7.63(7)$, $c = 32.7(1)$, $R_{wp} = 7.65\%$, $R_p = 6.07\%$, $\chi^2 = 19.69$. The main $14/mmm$ Rietveld phase, impurity phase, $\text{Bi}_7\text{F}_{11}\text{O}_5$ and lower symmetry Pawley phases are marked by upper blue ticks, middle black ticks, and lower blue ticks, respectively.

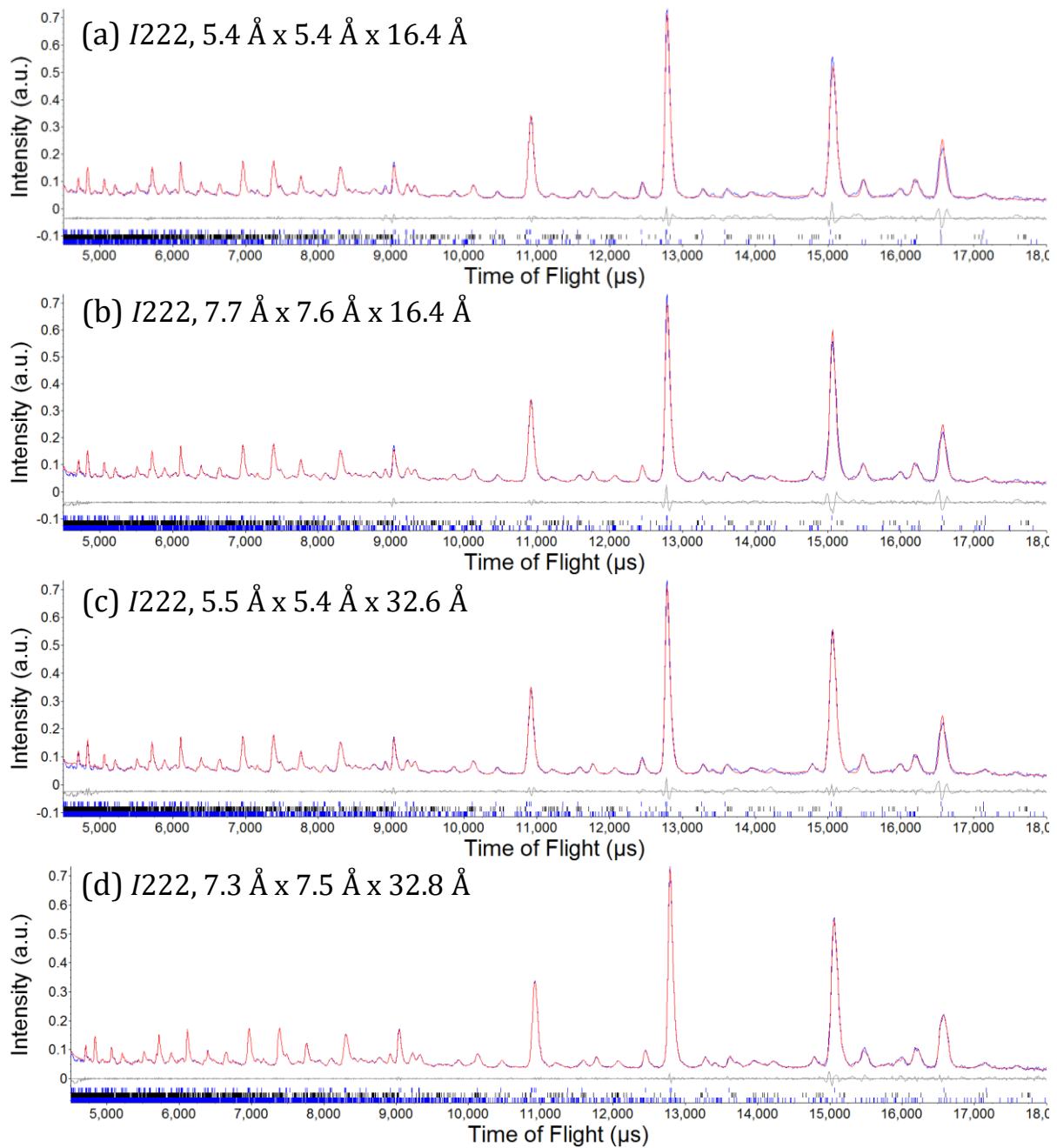


Figure 1.8.4 - Pawley refinements showing observed (-), calculated (-) and difference (-) profiles using 50 K NPD data of $\text{Bi}_2\text{CoO}_2\text{F}_4$ with respect to (a) Orthorhombic I222, $a = 5.438(2)$, $b = 5.409(1)$, $c = 16.389(4)$, $R_{wp} = 11.07\%$, $R_p = 8.21\%$, $\chi^2 = 10.07$; (b) Orthorhombic I222, $a = 7.70(2)$, $b = 7.626(3)$, $c = 16.412(4)$, $R_{wp} = 8.99\%$, $R_p = 7.08\%$, $\chi^2 = 7.78$; (c) Orthorhombic I222, $a = 5.452(2)$, $b = 5.428(2)$, $c = 32.64(1)$, $R_{wp} = 8.26\%$, $R_p = 6.65\%$, $\chi^2 = 10.06$; and (d) Orthorhombic I222, $a = 7.302(8)$, $b = 7.49(1)$, $c = 32.75(2)$, $R_{wp} = 9.81\%$, $R_p = 6.80\%$, $\chi^2 = 12.72$. The main 14/mmm Rietveld phase, impurity phase, $\text{Bi}_7\text{F}_{11}\text{O}_5$ and lower symmetry Pawley phases are marked by upper blue ticks, middle black ticks, and lower blue ticks, respectively.

1.9 Pawley Refinements of 50 K NPD Data using Space Groups deduced from IOSDISTORT

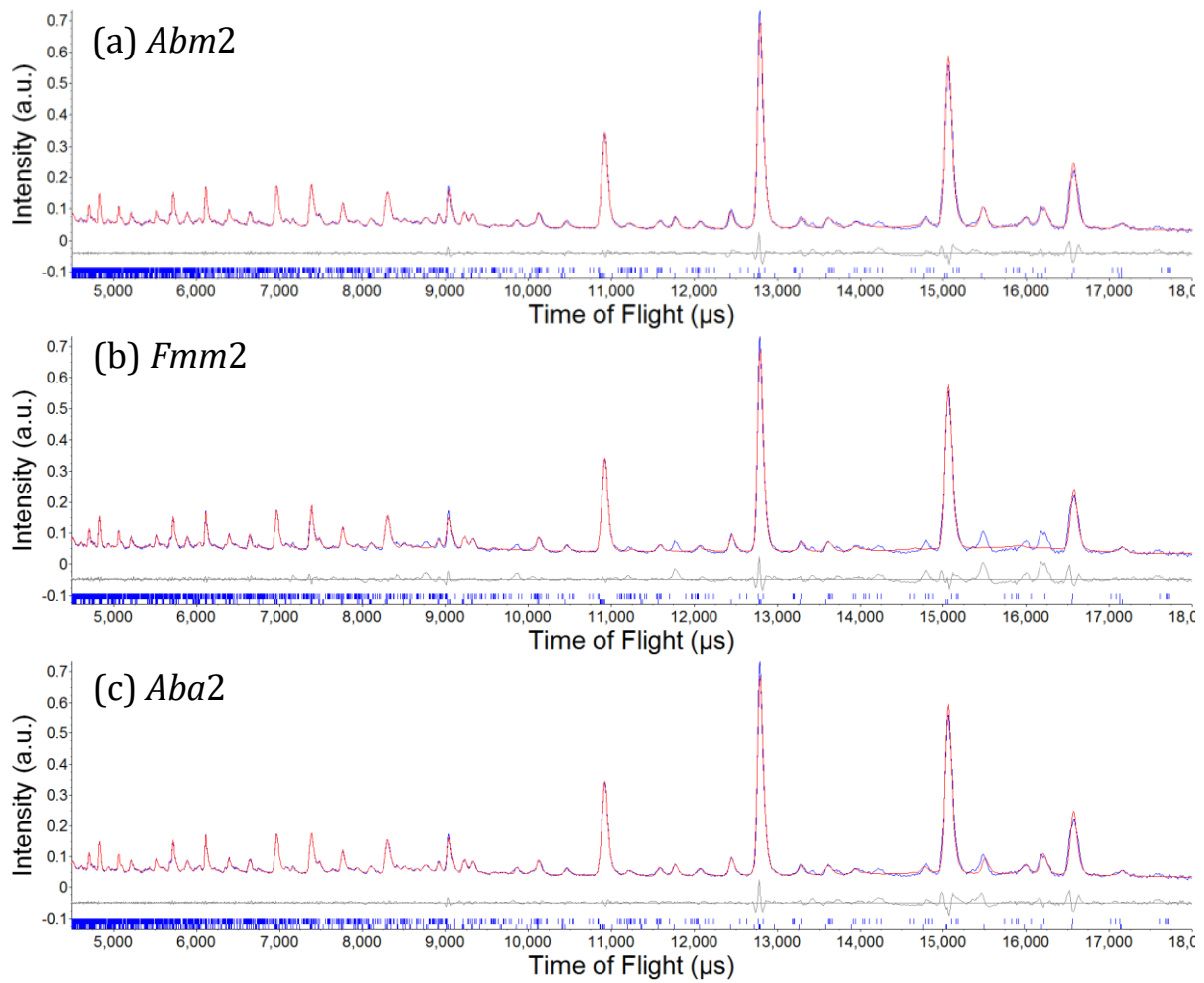


Figure 1.9.1 - Pawley refinements showing observed (-), calculated (-) and difference (-) profiles using NPD data of $\text{Bi}_2\text{CoO}_2\text{F}_4$ with respect to (a) Orthorhombic $Abm2$, $R_{wp} = 5.23\%$, $R_p = 4.07\%$, $\chi^2 = 3.35$; (b) Orthorhombic $Fmm2$, $R_{wp} = 8.79\%$, $R_p = 6.47\%$, $\chi^2 = 8.51$; and (c) Orthorhombic $Aba2$, $R_{wp} = 5.28\%$, $R_p = 4.20\%$, $\chi^2 = 3.63$. The impurity phase, $\text{Bi}_7\text{F}_{11}\text{O}_5$, and main Pawley phase are marked by upper blue ticks and lower blue ticks, respectively.

1.10 Rietveld Refinement of 50 K NPD Data using Various Models

2.1.1 *Fmm2* Model

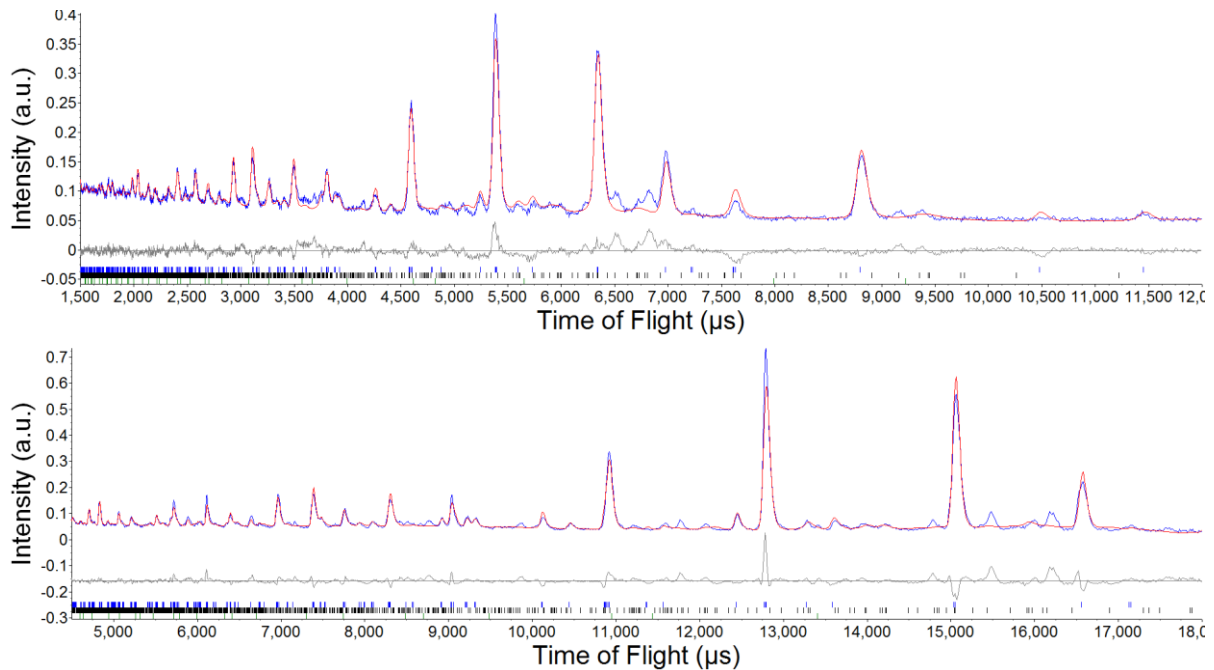


Figure 1.10.1 - Observed (-), calculated (-) and difference (-) profiles from Rietveld refinement using (top) bank 3 and (bottom) bank 5 of the 50 K NPD data of $\text{Bi}_2\text{CoO}_2\text{F}_4$. *Fmm2*, $a = 5.430(1) \text{ \AA}$, $b = 16.351(1) \text{ \AA}$, $c = 5.437(1) \text{ \AA}$, $R_{wp} = 9.63\%$, $R_p = 6.78\%$, $\chi^2 = 6.70$. Reflection positions of main phase and $\text{Bi}_7\text{F}_{11}\text{O}_5$ are marked by lower black ticks and upper blue ticks, respectively.

Table 1.10.1 - Details from refinement in space group *Fmm2* using 50 K NPD data.

Atom	X	y	z	Occupancy	Beq (\AA^2)	Site
Bi	0.00000	0.3274(2)	0.989(6)	1	0.35(5)	8c
Co	0.00000	0.00000	0.00000	1	0.3(2)	4a
O(eq.)	0.256(4)	0.00000	0.21(1)	1	19(2)	8d
O(ap.)	0.00000	0.1233(4)	0.925(7)	1	5.2(5)	8c
O(fl.)	0.25000	0.25000	0.229(6)	1	2.7(1)	8b

Table 1.10.2 - Selected bond lengths for $\text{Bi}_2\text{CoO}_2\text{F}_4$ from NPD refinements in space group *Cmca*.

Bond	Lengths in \AA at 50 K	Bond	Lengths in \AA at 50 K
Bi - O(fl.)	2 x 2.27(3)	Bi - O(ap.)	1 x 3.17(5)
Bi - O(fl.)	2 x 2.33(3)	Co - O(eq.)	2 x 1.83(7)
Bi - O(ap.)	1 x 2.50(5)	Co - O(eq.)	2 x 2.02(7)
Bi - O(ap.)	2 x 2.853(7)	Co - O(ap.)	2 x 2.059(1)

1.10.3 *Abm2* Model

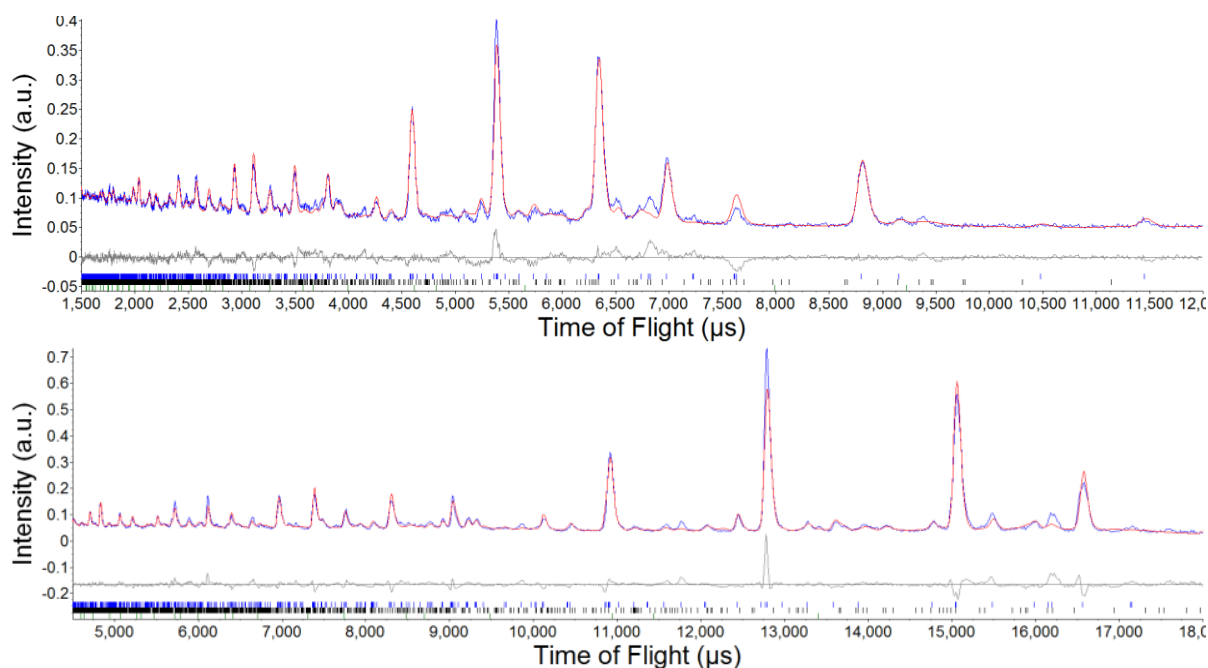


Figure 1.10.2 - Observed (-), calculated (-) and difference (-) profiles from Rietveld refinement using (top) bank 3 and (bottom) bank 5 of the 50 K NPD data of $\text{Bi}_2\text{CoO}_2\text{F}_4$. *Abm2*, $a = 5.436(1) \text{ \AA}$, $b = 16.351(1) \text{ \AA}$, $c = 5.431(1) \text{ \AA}$, $R_{\text{wp}} = 8.70\%$, $R_p = 6.17\%$, $\chi^2 = 5.48$. Reflection positions of main phase and $\text{Bi}_7\text{F}_{11}\text{O}_5$ are marked by lower black ticks and upper blue ticks, respectively.

Table 1.10.3 - Details from refinement in space group *Abm2* using 50 K NPD data.

Atom	X	y	z	Occupancy	Beq (\AA^2)	Site
Bi	0.7620(8)	0.5776(8)	0.253(6)	1	0.41(5)	8d
Co	0.75000	0.25000	0.25000	1	0.1(1)	4a
O(eq.)	0.47(1)	0.25000	0.06(1)	1	19(2)	4c
O(eq.)	0.015(6)	0.25000	0.45(1)	1	5.2(5)	4c
O(ap.)	0.694(2)	0.3719(3)	0.215(8)	1	2.7(1)	8d
O(fl.)	0.50000	0.00000	0.481(6)	1	0.21(8)	4a
O(fl.)	0.00000	0.00000	0.015(7)	1	1.2(2)	4a

Table 1.10.4 - Selected bond lengths for $\text{Bi}_2\text{CoO}_2\text{F}_4$ from NPD refinements in space group $\text{Abm}2$.

Bond	Lengths in Å at 50 K	Bond	Lengths in Å at 50 K
Bi - O(fl.)	1 x 2.22(3)	Bi - O(ap.)	1 x 3.07(1)
Bi - O(fl.)	1 x 2.28(3)	Co - O(eq.)	1 x 1.80(6)
Bi - O(fl.)	1 x 2.31(3)	Co - O(eq.)	1 x 1.82(5)
Bi - O(fl.)	1 x 2.41(3)	Co - O(ap.)	1 x 2.025(7)
Bi - O(ap.)	1 x 2.62(1)	Co - O(ap.)	1 x 2.025(7)
Bi - O(ap.)	1 x 2.67(6)	Co - O(eq.)	1 x 2.05(5)
Bi - O(ap.)	1 x 3.05(6)	Co - O(eq.)	1 x 2.10(7)

1.10.4 Cmca (X_2^+) Model

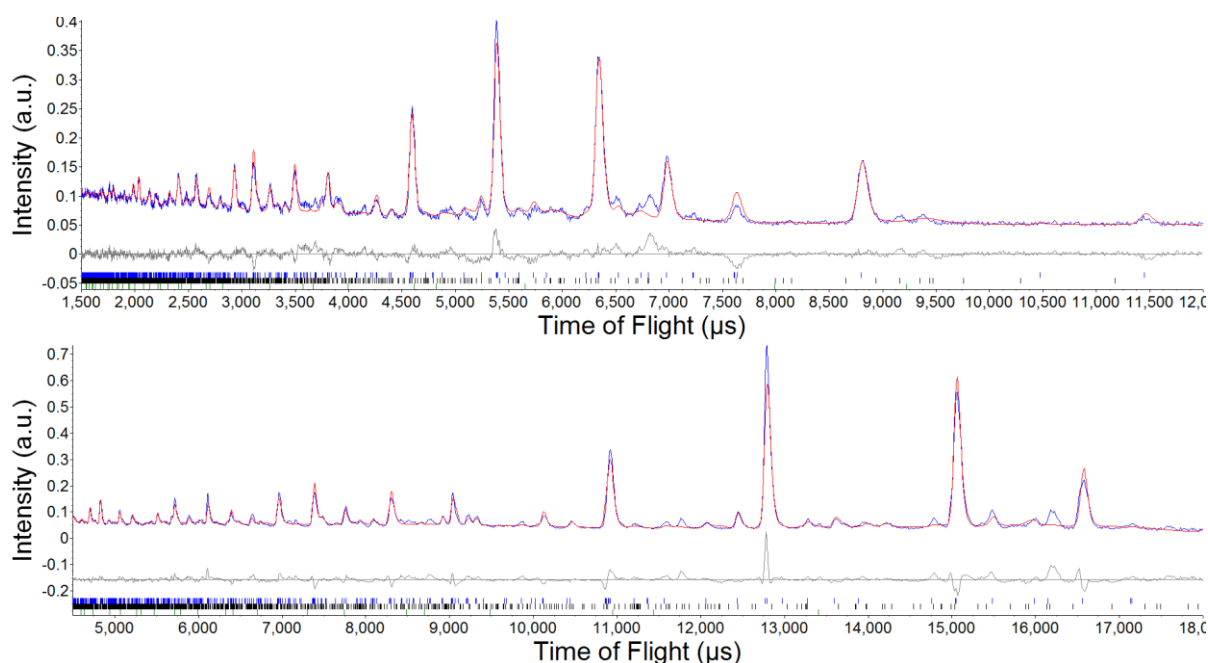


Figure 1.10.3 - Observed (-), calculated (-) and difference (-) profiles from Rietveld refinement using (top) bank 3 and (bottom) bank 5 of the 50 K NPD data of $\text{Bi}_2\text{CoO}_2\text{F}_4$. Cmca (X_2^+), $a = 16.353(1)$ Å, $b = 5.431(1)$ Å, $c = 5.435(1)$ Å, $R_{\text{wp}} = 9.46\%$, $R_p = 6.59\%$, $\chi^2 = 6.45$. Reflection positions of main phase and $\text{Bi}_7\text{F}_{11}\text{O}_5$ are marked by lower black ticks and upper blue ticks, respectively.

Table 1.10.5 - Details from refinement in space group *Cmca* (derived from X_{2^+} modes) using 50 K NPD data.

Atom	X	y	z	Occupancy	Beq (Å ²)	Site
Bi	0.3274(1)	0.00000	0.00000	1	0.48(5)	8d
Co	0.00000	0.00000	0.00000	1	0.1(1)	4a
O(eq.)	0.00000	0.207(3)	0.291(3)	1	9.9(4)	8f
O(ap.)	0.0.1215(4)	0.00000	0.00000	1	6.2(1)	8d
O(fl.)	0.25000	0.273(1)	0.25000	1	0.35(7)	8e

Table 1.10.6 - Selected bond lengths for $\text{Bi}_2\text{CoO}_2\text{F}_4$ from NPD refinements in space group *Cmca* (derived from X_{2^+} modes)

Bond	Lengths in Å at 50 K	Bond	Lengths in Å at 50 K
Bi - O(fl.)	2 x 2.229(4)	Co - O(eq.)	2 x 1.94(2)
Bi - O(fl.)	2 x 2.377(5)	Co - O(eq.)	2 x 1.95(2)
Bi - O(ap.)	2 x 2.841(2)	Co - O(ap.)	2 x 1.987(7)
Bi - O(ap.)	2 x 2.843(2)		

Appendix B - Anion Order to Break Inversion Symmetry

2.1 Space Groups Derived from Apical and Equatorial Ordering Modes

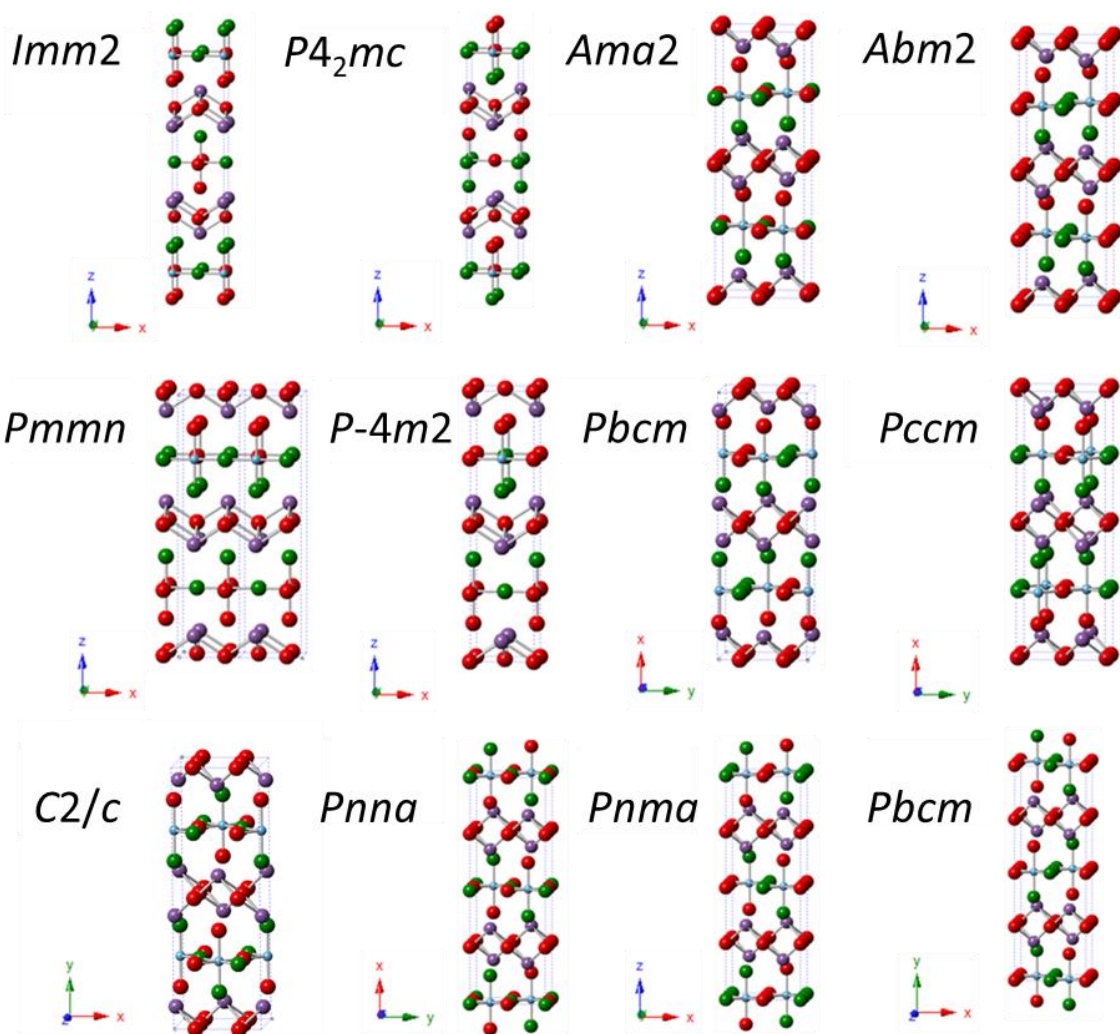


Figure 2.1.1 – Illustrations of the structures of each space group formed through combinations of apical and equatorial occupancy modes shown in Figure 4.2.3.

2.2 Space Groups Derived from Anion Ordering and Octahedral Rotational Modes

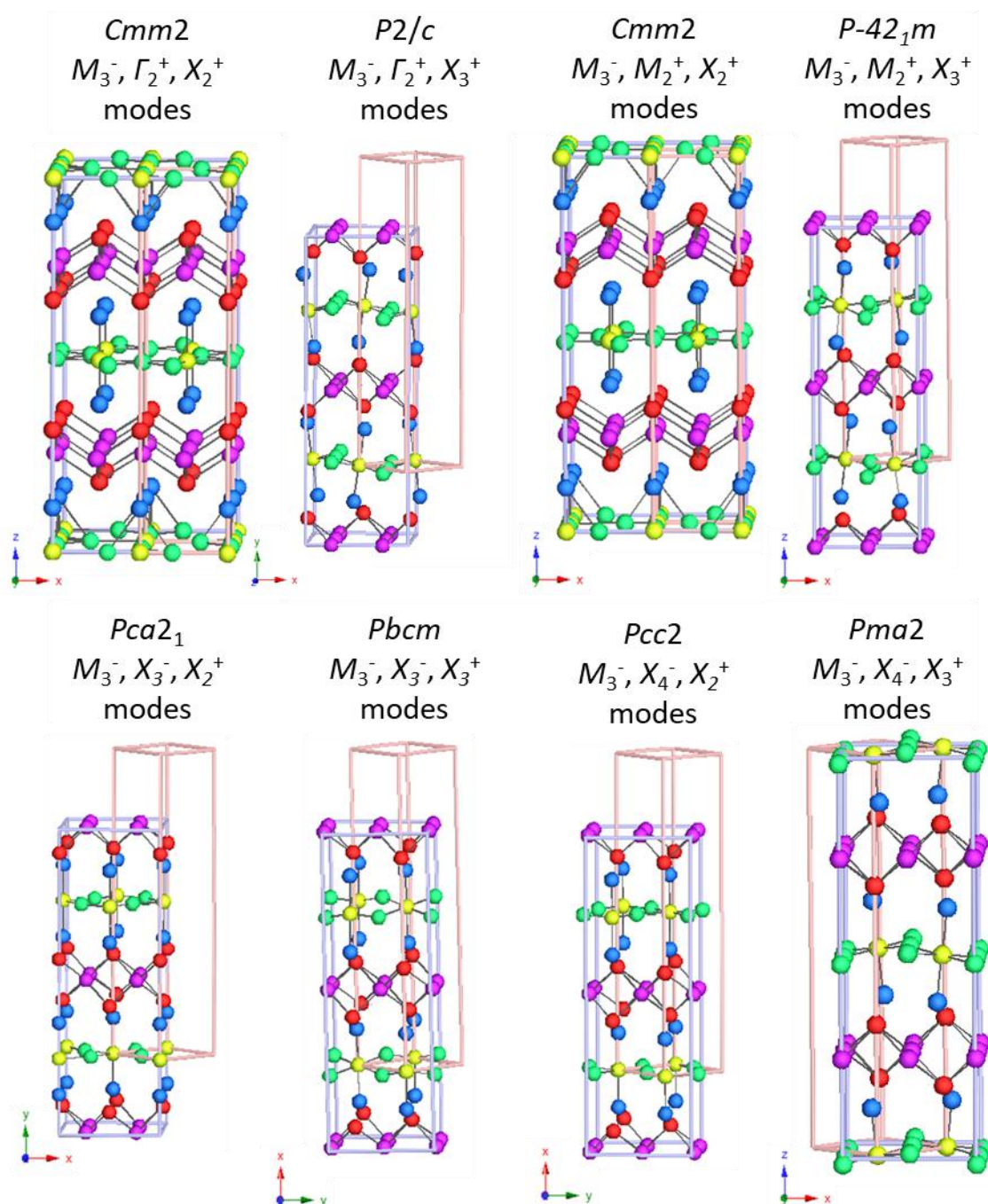


Figure 2.2.1 – Illustrations of structural symmetries derived through combinations of apical and equatorial occupancy modes with rotational modes, as seen in Figure 4.2.5. Each illustration is labelled with the space group and the occupancy/symmetry mode combinations above the picture.

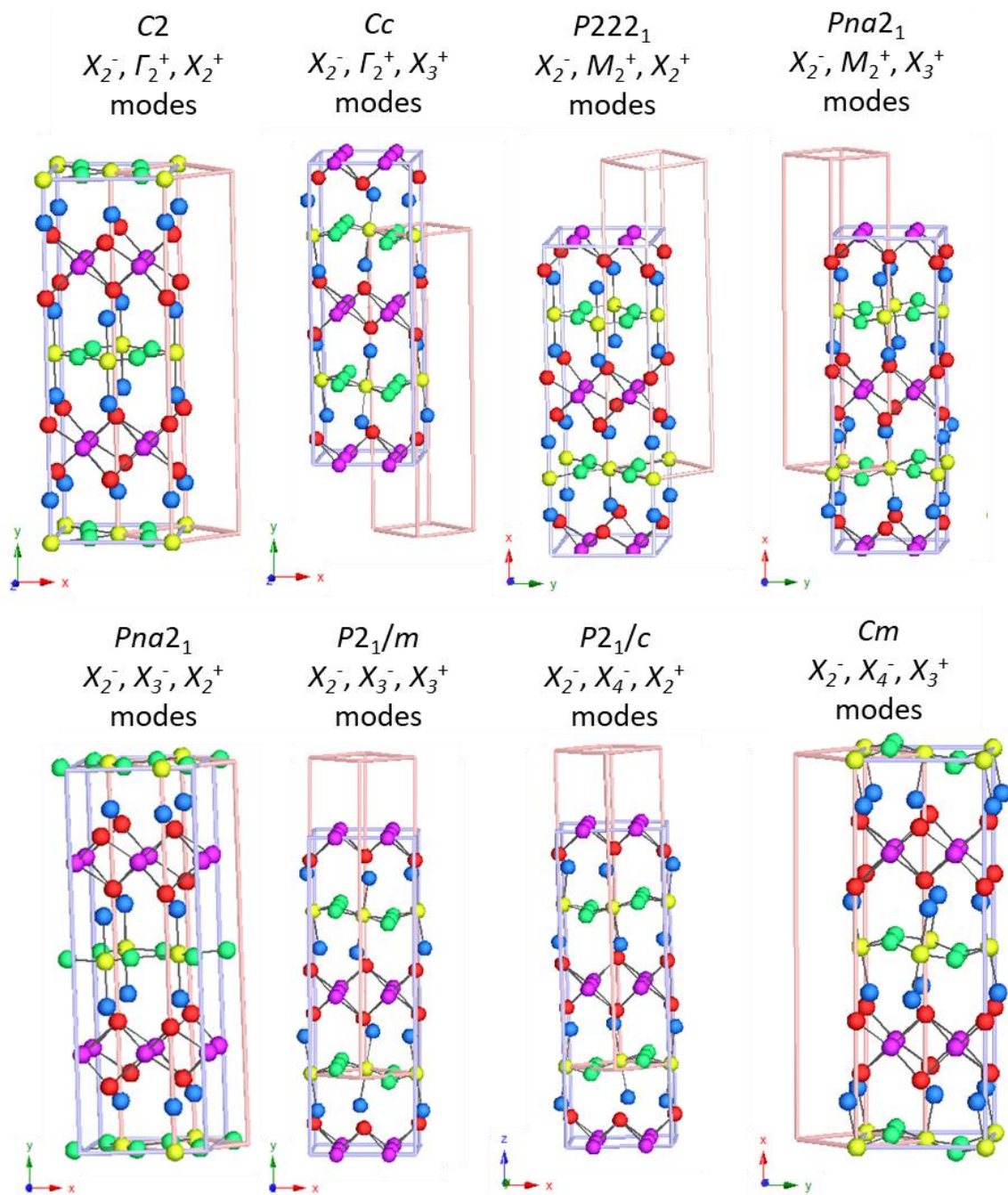


Figure 2.2.1 - Carried on from last page.